THE HONG KONG
POLYTECHNIC UNIVERSITY
香港理工大學
Pao Yue-kong Library
包玉剛圖書館

Copyright Undertaking

This thesis is protected by copyright, with all rights reserved.

By reading and using the thesis, the reader understands and agrees to the following terms:

1. The reader will abide by the rules and legal ordinances governing copyright regarding the use of the thesis.

2. The reader will use the thesis for the purpose of research or private study only and not for distribution or further reproduction or any other purpose.

3. The reader agrees to indemnify and hold the University harmless from and against any loss, damage, cost, liability or expenses arising from copyright infringement or unauthorized usage.

ULTRAFAST STRUCTURAL AND FUNCTIONAL PHOTOACOUSTIC MICROSCOPY TOWARDS CLINICAL APPLICATIONS

YINGYING ZHOU

PhD

The Hong Kong Polytechnic University

2021

The Hong Kong Polytechnic University

Department of Biomedical Engineering

Ultrafast structural and functional photoacoustic microscopy

towards clinical applications

ZHOU YINGYING

A thesis submitted in partial fulfillment of the requirements for the degree
of Doctor of Philosophy

April 2021

CERTIFICATE OF ORIGINALITY

I hereby declare that this thesis is my own work and that, to the best of my knowledge and belief, it reproduces no material previously published or written, nor material that has been accepted for the award of any other degree or diploma, except where due acknowledgement has been made in the text.

_____ (Signed)

ZHOU, YINGYING
_____   _____(Name of student)

ABSTRACT

Photoacoustic imaging (PAI), a hybrid imaging modality that integrates advantages of optical contrast and ultrasonic resolution, has been investigated in biomedical fields in recent years widely. Optical-resolution photoacoustic microscopy (OR-PAM) is an important branch of photoacoustic imaging and it can provide subcellular or cellular resolution of absorption targets, which is meaningful to interpret and grasp microscale mechanism for biology. To increase the detection accuracy and reduce the misalignments of physical activities, ultrafast OR-PAM is more suitable in capturing *in vivo* structural and functional information. In the past four years, my research mainly focuses on ultrafast structural and functional OR-PAM and its relevant biomedical applications via revision and improvement of current system or algorithm. Accordingly, the thesis is divided into three major aspects as follows.

In the first aspect, we present an ultrafast wavelength switching approach to achieve both high pulse energy and clear separation of multiple photoacoustic signals. A short fiber, e.g., 10-m long, allows the stimulated Raman scattering to generate high-energy pulses at demanded wavelengths. A frequency-domain method is developed to separate two photoacoustic signals that are partially overlapped in time. Numerical simulation and phantom experiments have validated the signal unmixing method. The results show that 50-ns delay between the two A-lines induces partial overlap, these two signals can be separated with 98% accuracy with 1.4% reduction in signal-to-noise ratio. This Fourier-domain separation method is further applied in *in vivo* functional OR-PAM. The oxygen saturation values can be reliable obtained based the two A-lines separated at each position. This ultrafast wavelength switching technique allows fiber-based stimulated Raman scattering method generates high pulse energy with negligible misalignment among different wavelengths for photoacoustic imaging. In addition, the short wavelength switching time increases the highest A-line rate of multi-wavelength photoacoustic imaging.

In the second aspect, three biomedical applications based on the ultrafast OR-PAM system developed in the first study or its modification are investigated.

The first application is tissue dichroism measurement. Dichroism is a kind of material property that leads to anisotropic optical absorption with different light polarizations.

It has a close relationship to types and alignments of excitation target and thus the dichroic tissues can be distinguished based the dichroism. In this study, we advance the dichroism photoacoustic imaging technique in terms of low noise and potentially high imaging speed. We develop a single-shot system that the three laser beams are splitted from one laser pulse and they are separated in time for dichroic optical-resolution photoacoustic microscopy. The three pulses have identical pulse energies, different polarizations, and a sub-microseconds time delay. In such a way, the dichroism photoacoustic imaging is insensitive to pulse energy fluctuation and can maintain a low detection noise in fast scanning. We not only measure the dichroism degree of target but also calculate the orientation angle of it. The new dichroism can be served as a contrast to image dichroic tumor or probe-conjugated tumor detection in the future.

The second application is to monitor the outcomes of cupping therapy from a quantitative imaging perspective. Cupping therapy, thousands of years widely used traditional Chinese medicine practice, uses cups to create suction onto the skin, aiming to stimulate blood circulation and ease the symptoms of some diseases, such as fatigue, tension, and muscle pain. However, due to lack of scientific evidence, the actual effect has always been controversial. In order to objectively and quantitatively evaluate the cupping therapy effect, here OR-PAM is introduced to observe microenvironment parameters changes including structural and functional parameters in animal models before and after cupping through facial cups. It is found that within a short time and tiny pressure after cupping (5 minutes and -20 kPa), more capillaries appear, with some associated with slight blooding. We also quantify all the results and find that the total haemoglobin concentration increases 64% and 40% in veins and arteries, respectively. The oxygen saturation declines about 17% and 3% in veins and arteries, respectively. The elevation in haemoglobin concentration and the decrease in oxygen saturation recover to their original levels two hours later, indicating that the cupping therapy only last a short period. This study is the first time to quantitatively investigate the microenvironment changes of cupping therapy through imaging prospective, which indicates the evaluating ability of OR-PAM. These capabilities, if further engineered, can be extended for wide applications of cupping treatment monitoring and guidance.

The third application is to measure medium viscosity via Grueneisen relaxation effect. Viscosity measurement is important in many areas of biomedicine and industry.

Traditional viscometers are usually time-consuming and require huge sample volumes. Microfluidics overcomes the challenge of large sample consumption but takes a long time to measure it. Moreover, the microfluidic device needs to design a special supporting microstructure to measure the viscosity, which may be complex and costly. Here, we propose photoacoustic viscometry to measure the liquid viscosity in generic microfluidic devices based on dual-pulse photoacoustic flowmetry. The new viscometer method embraces fast detection speed, low fluid consumption, and high detection sensitivity, offering a new tool for efficient viscosity measurement in a broad range of microfluidic devices.

In the last aspect, we propose to achieve ultrafast "OR-PAM" via deep learning. Here, the "OR-PAM" imaging performance is obtained by learning acoustic-resolution photoacoustic microscopy (AR-PAM)' scanning data but having OR-PAM's resolution. Conventional AR-PAM can image deeper than OR-PAM but with low image resolution. Besides, AR-PAM has a faster raster scanning speed as much fewer scanning steps are involved due to the limitation of resolution. How to achieve deep depth imaging while keeping high resolution and fast speed is essential in photoacoustic microscopic applications due to the trade-off between depth and resolution. Imaging quality such as contrast and signal-to-noise ratio has been improved through deep learning in recent years. Here, we propose to use that to realize ultrafast "OR-PAM" by learning the AR-PAM data so that we are able to obtain "OR-PAM" resolution and AR-PAM penetration depth simultaneously. Groups of mice ear images are collected to train the neural network. Feasibility and the efficiency of the network is validated with additional experimental mice brain AR-PAM data that are excluded in training.

In summary, this thesis aims on ultrafast structural and functional OR-PAM through system modification and algorithm development. Moreover, three different biomedical and clinical applications are investigated based on the ultrafast system or its derivation. All these provide new knowledge of the structural and functional OR-PAM and constitute critical steps to further the development of photoacoustic imaging towards in-depth biomedical research and applications.

PUBLICATIONS ARISING FROM THE THESIS

Peer-reviewed Journal Publications

(*equal contribution)

1. **Y. Zhou***, C. Liu*, X. Huang*, X. Qian, L. Wang[#], P. Lai[#], "Photoacoustic prediction of physiological conditions based on viscosity changes with microliter consumption". *Under review.*

2. S. Cheng*, **Y. Zhou***, H. Li, L. Wang[#], P. Lai[#], "Ultrafast deep penetration optical resolution photoacoustic microscopy through learning-based resolution transformation". *Under review.*

3. X. Huang*, **Y. Zhou***, CM. Woo, Y. Pan, L. Nie, P. Lai[#], "Multifunctional layered black phosphorene-based nanoplatform for disease diagnosis and treatment: a review". *Frontiers of Optoelectronics* 13(4), 327-351, 2020.

4. **Y. Zhou***, F. Cao*, H. Li, X. Huang, D. Wei, L. Wang[#], P. Lai[#], "Photoacoustic imaging of microenvironmental changes in facial cupping therapy". *Biomedical Optics Express* 11(5), 2394-2401, 2020

5. **Y. Zhou**, S. Liang, M. Li, C. Liu, P. Lai[#], L. Wang[#], "Optical-Resolution Photoacoustic Microscopy with Ultrafast Dual-Wavelength Excitation". *Journal of Biophotonics,* 2020

6. **Y. Zhou***, J. Chen*, C. Liu, C. Liu, P. Lai[#], L. Wang[#], "Single-shot linear dichroism optical-resolution photoacoustic microscopy". *Photoacoustics* 16, 100148, 2019

7. X. Huang, W. Shang, H. Deng, **Y. Zhou**, F. Cao, C. Fang, P. Lai, J. Tian[#], "Clothing spiny nanoprobes against the mononuclear phagocyte system clearance in vivo: Photoacoustic diagnosis and photothermal treatment of early stage liver cancer with erythrocyte membrane-camouflaged gold nanostars". *Applied Materials Today* 18, 100484, 2019

8. H. Li, F. Cao, **Y. Zhou**, Z. Yu, and P. Lai[#], "Interferometry-free noncontact photoacoustic detection method based on speckle correlation change". *Optics Letters* 44(22) 5481-4, 2019

Conference Presentations

1. **Y. Zhou,** F. Cao, P. Lai, "Photoacoustic assessment of microenvironment parameter changes during facial cupping therapy". SPIE Photonics Asia 2020, Beijing, China, 2020 (*Invited Oral*)

2. **Y. Zhou,** S. Liang, L. Wang, P. Lai, "Optical-Resolution Photoacoustic Microscopy with Ultrafast Dual-Wavelength Excitation". SPIE Photonics West 2020, San Francisco, USA, 2020 (*Oral*)

3. **Y. Zhou,** J. Chen, L. Wang, P. Lai, "Multi-pulse dichroism optical resolution photoacoustic microscopy". SPIE Photonics Asia 2019, Hangzhou, China, 2019 (*Oral*)

4. **Y. Zhou,** J. Chen, L. Wang, P. Lai, "Pulse-Delayed Dichroism Optical-Resolution Photoacoustic Microscopy". European Conferences on Biomedical Optics 2019, Munich, Germany, 2019 (*Oral*)

5. **Y. Zhou**, L. Wang, P. Lai, "Pulse-Delayed Dichroism Optical-Resolution Photoacoustic Microscopy". IEEE photonics society HK section postgraduate conference, Hong Kong, China, 2019 (*Oral*)

ACKNOWLEDGEMENTS

Time flies. Four years have passed so quickly. The journey of PhD study is not easy, and it can even be said to be very challenging, but it is still nearly the end now. Recalling the life and work in the past four years, many thanks are more than I can express.

Firstly, I am sincerely thankful to my Chief Supervisor, Prof. Puxiang Lai, who has given many encouragements and helps for my PhD study. When I entered his lab four years ago, it was my first time to learn how to do research. I almost lost myself, but he helped me to think logically and find the interest of research. He likes brainstorming and discussion, which always gave me inspirations and made me to look for new ideas. He is a so nice friend, giving enough freedom and time for me to do my interested research. When I encountered problems, he always encouraged me and efficiently discussed with me, which gave me many confidence and hope. Then, I also express my heartfelt thanks to Prof. Lidai Wang at City University of Hong Kong. I finished several projects in his lab with the helps from him. He is knowledgeable and he always can find the solutions to solve the problems encountered in research. His rigorous attitude towards scientific research is respectable and from that I also learned how to do research. This thesis cannot be finished without their help, I really want to express my most loyal thanks to them.

Apart from home, lab is where I stayed longest. My lab members are all my good friends, who have been giving countless warmness to me and sharing happiness with me. Ms. Xiazi Huang, one of my best friends, always shares interesting things in life with me. I also want to say thanks to Ms. Fei Cao, Mr. Huanhao Li, Mr. Zhipeng Yu, Mr. Tianting Zhong, Ms. Chiman Woo, Mr. Yuchen Song, Mr. Shengfu Chen, and Mr. Qi Zhao. Every time from talking with them I can receive positive replies, which helps me to live optimistically. In addition, Prof. Lidai Wang's lab members also give me many helps, especially Mr. Siyi Liang. Every time when I encounter project difficulties in his familiar fields, he always explains patiently and in detail to me. I also want to thanks for Mr. Guohua Wen, Mr. Chao Liu, Mr. Yachao Zhang, Mr. Jiangbo Chen, Mr. Mingsheng Li, Ms. Jingyi Zhu and Mr. Yue Wang in his lab for their helps.

Lastly, I want to say thanks and love to my family. My parents and grandparents always support me materially and spiritually, and they have been continuously showing their kindness to respect my decisions. Besides my parents, there is another person in this world who loves me so much, my husband, Dr. Jiyu Li. He always gives me love and tolerance. He accompanies with me finishing my PhD study, and I can say that I cannot hold on the hard journey without his love.

Thanks a lot!

TABLE OF CONTENTS

LIST OF TABLES

LIST OF FIGURES

1 INTRODUCTION

1.1 Background and Motivation

1.1.1 Photoacoustic imaging

In the broad electromagnetic spectrum, light, especially the near infrared light and visible light, is the only one in the frequency band that can directly interact with almost all kinds of molecules, such as RNA/DNA, fat, cytochrome, melanin, glucose, haemoglobin, and water. By using light, we can obtain structure, metabolism, and molecular information of cell and tissue, including haemoglobin concentration, blood oxygen saturation, blood flow, blood vessel density, etc. [1]. Meanwhile, compared with high-energy rays, light is a safe electromagnetic wave. Compared with MRI, the detection system is relatively simple and economic. Advantages of optical imaging include molecular contrast, safety, high sensitivity, high resolution and relatively low cost [2]. As a result, optical imaging has been increasingly used in today's biomedicine [3]. However, due to the highly uneven distribution of optical refractive index, light will be strongly scattered when propagating in complex media such as biological tissues. Even though light absorption could be weak, the effective penetration of visible and near infrared ballistic (*i.e.*, non-scattered) or quasi-ballistic (*i.e.,* only being scattered for one or a couple of times) photons into biological tissue is shallow [4], resulting in very limited penetration depth for high-resolution optical techniques within tissue. If a highly confined *in situ* optical imaging within or through biological tissue can be

obtained, it may pave a new way for the optical diagnosis and treatment of many human diseases that occurs at depths in tissue.

Through converting diffused light into non- or weak-scattered ultrasonic waves in deep tissue, photoacoustic imaging (PAI) integrates advantages of optical contrast and ultrasonic resolution, providing a promising strategy to overcome the aforementioned challenges [5, 6]. As shown by the name, photoacoustic imaging reconstructs the optical information based on the received ultrasound waves, achieving optical contrast and diffusive light penetration depth but with ultrasonic or sub-ultrasonic resolution. The principle of photoacoustic imaging is illustrated in Figure 1-1 [7, 8]. The region of interest is excited by a pulsed laser, which is absorbed and causes a rapid local temperature rise within a short time window. Followingly, the temperature rise leads to thermal expansion and hence vibrations, which propagate in form of ultrasonic waves and will be captured with one or an array of ultrasonic transducer positioned surrounding the medium. Lastly, spatial distribution of optical absorption of the region of interest is reconstructed through algorithms.
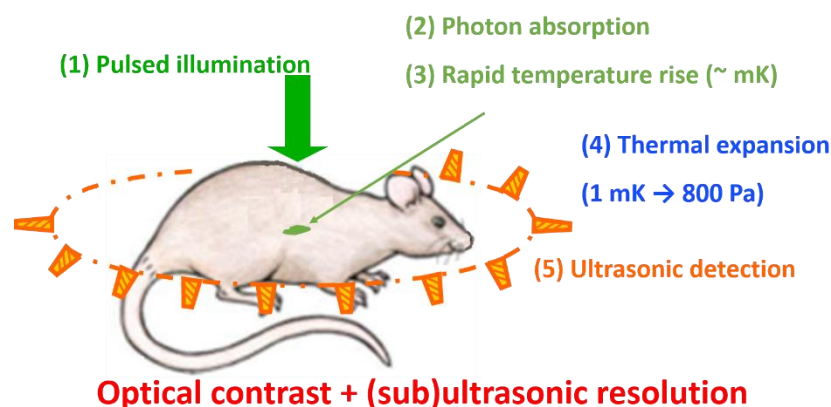
Figure 1-1 Principle of Photoacoustic Imaging

PAI, as a new hybrid imaging modality, has seen steady development in the past two decades and wide applications in the past few years. It has two major categories, photoacoustic microscopy (PAM) and photoacoustic computed tomography (PACT). In PACT, the reconstruction imaging formation is based on multi-element transducer array's mechanical/ electronic scanning [4]. Usually, PACT uses high energy laser to illuminate the target and the high energy pulse can penetrate deep tissue of up to several centimetres. Thus, PACT has brood imaging and diagnosis applications in whole small animal models, such as brain [9-11], eyes [12, 13], gastrointestinal tract [14], thyroid [15], breast [16-20], intraoperation [21], ovarian [22], prostate [23], bone and joint [24, 25], skin [26], and so on. In PAM, the other main branch of PA imaging, the imaging information is directly formed through the optical illumination zone's raster scanning and a single-element ultrasound transducer is usually used to receive PA signals. PAM can be further divided to acoustic-resolution PAM (AR-PAM) and optical-resolution PAM (OR-PAM) based on the dominant determination factor for lateral resolution [4]. In the latter, laser pulse is tightly focus on the target site, the diameter of the spot size is usually over 10 times minor than the acoustic focus, achieving a lateral resolution down to micron or submicron scales. The capability of OR-PAM for subcellular or cellular resolution allows it to be applied for micro-scale imaging and monitoring. At depths beyond diffusion limit, AR-PAM can reach tens of micrometres resolution by taking the advantage of ultrasonic focus while the laser beam is loosely focused or even diffusive under strong scattering. Compared with OR-PAM, AR-PAM can realize deeper tissue imaging with compromised lateral resolution and hence it is promising for applications at moderate tissue depths [27, 28].
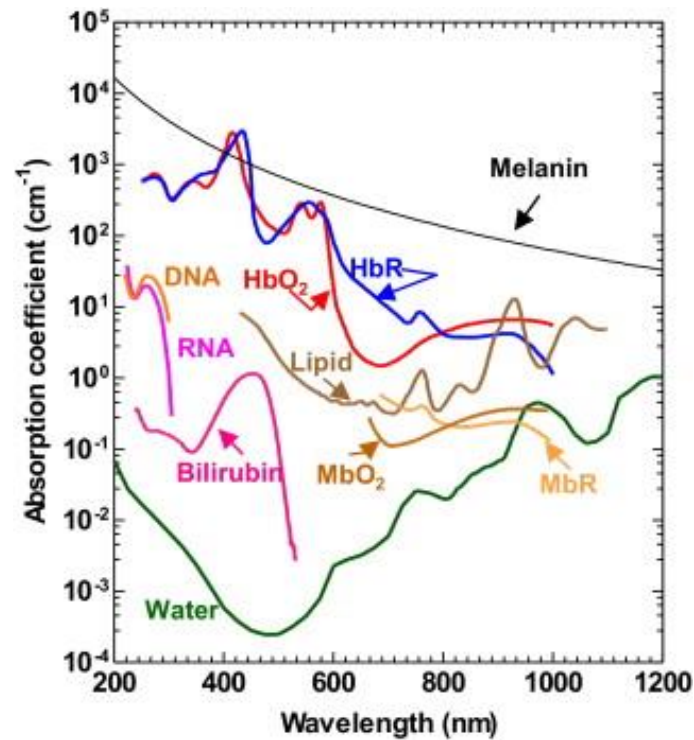
Figure 1-2 Absorption spectrum of major endogenous contrast agents in biological tissue at normal concentrations [29]

The contrast for PA imaging includes endogenous and exogenous contrast. The endogenous contrast contains many strong absorption materials in biological tissue, such as RNA/DNA, cytochrome, glucose, lipid, haemoglobin, melanin, and water. These contrasts are easy to capture and help to realize non-invasive label free photoacoustic imaging. Figure 1-2 shows the absorption spectrum of some major endogenous contrasts. As seen, different materials have their own absorption spectrum and absorption peak [29]. It indicates that PA imaging can be used to differentiate materials based on their featured absorption spectrum. In scenarios such as the target is surrounded by similar strong absorption background, it becomes challenging to extract useful target information and exogenous contrast agents can be considered. Various exogenous contrasts, mainly including organic dyes [30-32] and nanoparticles [33-35],

4

have been synthesised and used to increase the imaging contrast and specificity in PA imaging [36-40].

1.1.2 Functional optical-resolution photoacoustic microscopy

Taking advantages of wavelength-dependent optical absorption feature and the micron-scale imaging ability, OR-PAM is widely applied to map and compute various functional parameters of the target tissue region, such as total hemoglobin concentration (C_{Hb}), oxygen saturation values (sO_2), and blood flow speed [41-47]. Each parameter has its close tie to certain physiological indication. For example, the sO_2 is the percentage of oxy-haemoglobin in the blood, which is an important physiological parameter of healthy state. The level of blood sO_2 directly affects the normal metabolism of cells, which further reflects the metabolism of tissues to some extent. Abnormal sO_2 levels may indicate unhealthy conditions like cancer [48]. OR-PAM can calculate the sO_2 levels via two or more wavelengths due to the different absorption spectra (except for isosbestic points at 498 nm, 532 nm, 545 nm and 568 nm) between the oxy-hemoglobin and deoxy-hemoglobin [49, 50]. Since multiple measurements of the same tissue region corresponding to various wavelengths are required, functional OR-PAM for *in vivo* imaging usually requires fast scanning speed to obtain dynamic physiological information and mitigate the motion-induced artefacts.

Regarding the provision of optical pulses of different wavelengths, different approaches have been proposed. The simplest, or the most straightforward one, is to have a laser source possessing two or more wavelengths internally [51], or to combine more than one laser sources (of different wavelengths) to generate adjacent pulses of different wavelengths [47, 52-54]. A typical system setup is shown in Figure 1-3 [52], where

two laser sources generate 532 nm and 559 nm pulses in sequence to excite PA signals to compute the functional parameters, inclusive of cerebrovascular anatomy, hemoglobin concentration, hemoglobin oxygen saturation, and blood flow. The time delay between adjacent pulses of different wavelengths is controlled through an external triggering signal, with a wavelength switching time shorter one A-line duration.
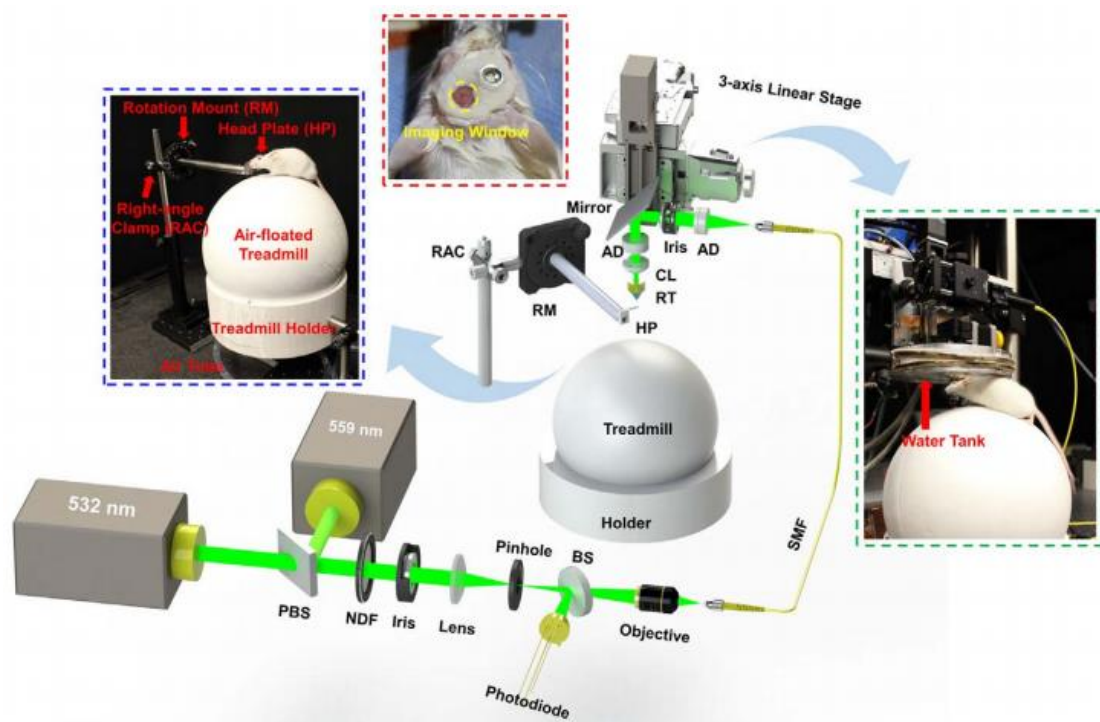
Figure 1-3 Head-restrained PAM from Hu's Group. PBS, polarizing beam splitter; NDF, neutral density filter; BS, beam sampler; SMF, single-mode fiber; AD, achromatic doublet; CL, correction lens; RT, ring-shaped ultrasonic transducer; RM, rotation mount; HP, head plate; RAC, right-angle clamp. Red-boxed inset: photograph of a mouse brain with a thinned-skull window and a nut attached using dental cement. Blue-boxed inset: photograph of the angle- and height-adjustable head-restraint apparatus. Green-boxed inset: the mouse placement during imaging [52].

Switching wavelength pulse by pulse by an electro-optical modulator (EOM) is another approach to yield optical pulses of multiple wavelengths [55, 56]. Figure 1-4 shows such an example [56]. Under the modulation of EOM, laser beams transport along two directions at the Polarization Beam Splitter (PBS). Half pulses transmit through the PBS, maintaining the wavelength of 532 nm; the other half pulses are reflected at the PBS due to their polarization shift by the EOM and travel through a single-mode polarization-maintaining fiber (PM-SMF), where stimulated Raman scattering effect alters the light wavelength to 558 nm. Pulses of two different wavelengths are recombined at the dichroic mirror (DM), then relayed by the single-mode fiber (SMF), eventually focused onto the target position in turns.
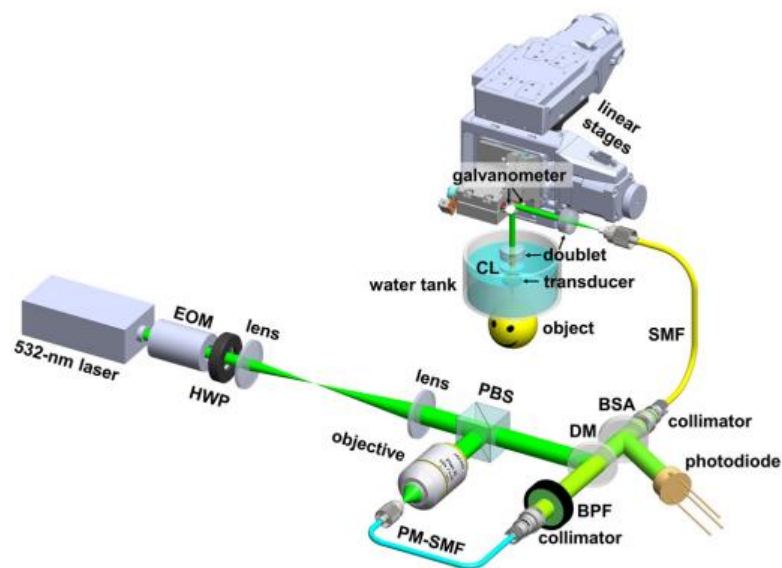
Figure 1-4 Schematic of a high-speed multi-parametric PAM system. EOM, electro-optical modulator; HWP, half-wave plate; PBS, polarizing beam splitter; PM-SMF, polarization-maintaining single-mode fiber; BPF, bandpass filter; DM, dichroic mirror; BSA, beam sampler; SMF, regular single-mode fiber; CL, correction lens [56].

These two methods require a short wavelength switching time shorter than one A-line duration, so that PA signals corresponding to different wavelengths can be separated. Apart from this, the multiple laser sources option is costly, and the emission fluctuations from two lasers cannot be avoided and may not be well synchronized. All these can lead to measurement errors. The EOM-based multiple wavelengths option is not stable in fast raster scanning (large step size) because laser pulses of different wavelengths actually excite different locations in the target region. The mismatch between sequential pulses equals the step size of raster scanning.

In order to reduce the fluctuations and misalignments in fast functional OR-PAM, we choose to generate pulses of multiple wavelengths through optical fibers based on the stimulated Raman scattering (SRS). In this, only one laser source is used and different wavelengths are generated simultaneously from one pulse excitation, so that the fluctuations of laser outputs can be counteracted with each other. In the meanwhile, unlike conventional pulse delaying method using a long optical fiber, we significantly shorten the fiber length and propose a new algorithm that can disentangle the partially overlapping adjacent PA signals corresponding to different wavelengths. These technical innovations assure the development of an ultrafast functional OR-PAM system, which serves as the experiment platform for a series of applications and explorations in this thesis.

1.2 Thesis Outline

Three major parts as follows is divided from this thesis.

In the first part (Chapter 2), an ultrafast OR-PAM system and a signal separation method for partially overlapping PA signals are proposed to realize higher energy

output and ultrafast dual-wavelength switching. Since the time delay between adjacent pulses of different wavelengths are very short (order of 10 ns), the corresponding PA signals are unavoidable to be partially overlapped. Thus, a Fourier-domain signal separation method is proposed to disentangle the overlapping signals, and the feasibility of this separation method is confirmed through simulation and animal experiments.

In the second part (Chapters 3-5), three different biological and clinical related applications are investigated based on the ultrafast OR-PAM system developed in Chapter 2 or its modifications. The first application is to measure tissue dichroism. Three-wavelength dichroism detection OR-PAM schematic which is extended from the ultrafast OR-PAM system in Chapter 2 is built, which can determine not only the dichroic degree but also the orientation angles, and overcome the unstable drawbacks of current EOM-based dichroism detection setup. To extend applications from *in vitro* targets to clinical goals. The second application is to monitor the microenvironment parameters changes including the total haemoglobin concentration, vascular density and oxygen saturation after cupping treatment with the dual-wavelength ultrafast OR-PAM system that is the same with our ultrafast OR-PAM with changed fiber length to be more suitable for this study. This is the first time to investigate the physiological changes of cupping therapy from an *in vivo* microscopic imaging aspect. The last application is to measure fluidic and blood viscosity based on the Grueneisen relaxation effect. A mathematical model between the liquid viscosity and Grueneisen relaxation effect is established, which is then verified with the dual-wavelength ultrafast OR-PAM system. Various blood samples corresponding to different disease models are tested and compared, which is meaning to disease state monitoring.

In the third part (Chapter 6), we apply deep learning trained network to improve AR-PAM imaging quality to the OR-PAM standard (resolution) to achieve ultrafast deep-penetrating "OR-PAM" that has similar optical resolution but faster imaging speed compared with normal OR-PAM. This method combines advantages of fast raster scanning and deep-penetration depth of AR-PAM and high lateral resolution of OR-PAM. OR-PAM and AR-PAM data from mice ears are collected to train the neural network and AR-PAM brain images are used to test the feasibility and efficiency of the method.

2 OPTICAL-RESOLUTION PHOTOACOUSTIC MICROSCOPY WITH ULTRAFAST DUAL-WAVELENGTH EXCITATION

This chapter is reproduced with some adaptations from the manuscript "Yingying Zhou, Siyi Liang, Mingsheng Li, Chao Liu, Puxiang Lai, and Lidai Wang, "Optical-Resolution Photoacoustic Microscopy with Ultrafast Dual-Wavelength Excitation". Journal of Biophotonics, 2020. The contributions of authors are as follows: L. Wang, P. Lai and Y. Zhou conceived the idea. Y. Zhou, M. Li, C. Liu, and P. Lai designed the system. Y. Zhou, S. Liang and L. Wang design the algorithm. Y. Zhou ran the experiment. Y. Zhou, S. Liang, P. Lai and L. Wang prepared the manuscript. All authors were involved in the analysis of the results and manuscript revision.

In this chapter, we present an optical-resolution photoacoustic microscopy with ultrafast dual-wavelength excitation and a signal separation method to achieve high pulse energy and ultrafast dual-wavelength excitation. The signal separation method is validated via numerical simulation and phantom experiment. We show that when two photoacoustic signals are partially overlapped with a 50-ns delay, they can be recovered with 98% accuracy. We apply this ultrafast dual-wavelength excitation technique to in vivo OR-PAM. Results demonstrate that two PA signals corresponding

to two wavelengths from one A-line can be successfully separated, and sO2 values can be reliably computed from the separated data. The ultrafast dual-wavelength excitation enables fast functional photoacoustic microscopy with negligible misalignment among different wavelengths and high pulse energy, which is important for in vivo imaging of microvascular dynamics.

2.1 Introduction

As mentioned earlier, OR-PAM is a non-invasive imaging technique that offers optical absorption contrast at subcellular resolution [4]. Using multiple excitation wavelengths, OR-PAM can quantify different types of molecules according to their unique absorption spectra [57, 58]. For example, with two or more wavelengths, OR-PAM can image hemoglobin concentration and blood oxygen saturation (sO2) [59, 60]. *In vivo* functional OR-PAM often needs high imaging speed to acquire dynamic physiological information and mitigate motion artifacts. Fast functional OR-PAM requires a laser source having two or more wavelengths, high pulse repetition rate, fast multi-wavelength excitation, and sufficient pulse energy for satisfactory signal-to-noise ratio (SNR) [61-63].

Several pulsed laser techniques have been developed for fast dual-wavelength excitation in OR-PAM. One method is to sequentially trigger two pulsed lasers [64, 65]. Another method is to use an electro-optical modulator (EOM) to switch among different wavelengths [56, 66]. The third method is to generate multiple wavelengths via stimulated Raman scattering (SRS) [67, 68] and delay them differently with long optical fibers [61]. These methods require delay time between different wavelengths not less than one A-line duration to separate the signals. However, in fast OR-PAM, if the delay

time between different wavelengths is comparable with the pulse repetition time of one wavelength, different wavelengths may excite spots significantly misaligned. To minimize this misalignment, the delay time between different wavelengths needs to be much shorter than the single-wavelength pulse repetition time. Furthermore, in the SRS approach, a long delay fiber, as required by the long delay time between different wavelengths, may limit the highest pulse energy it can deliver, leading to weak photoacoustic signals [69, 70]. Therefore, a short multi-wavelength excitation time is preferred for reducing misalignment and improving sensitivity.

In this chapter, we present a novel frequency-domain approach to separate partially overlapped PA signals reliably, reducing the multi-wavelength excitation time in functional OR-PAM to be shorter than an A-line duration. First, we simulate the separation algorithm. Then, we use the SRS and fiber delay to implement 50-ns dual-wavelength excitation. In phantom experiments, we can separate the partially overlapped PA signals with a good SNR (only reduces by 1.4%). *In vivo* sO_2 is imaged using ultrafast dual-wavelength excitation, whose results are as accurate as of the conventional OR-PAM method.

2.2 Method

2.2.1 Experimental Setup

A schematic of ultrafast dual-wavelength excitation OR-PAM is shown in Figure 2-1a. A pulsed laser (7-ns pulse width, VPFL-G-20, Spectra-Physics) emits 532-nm wavelength. The pulse repetition rate of the laser is 4 kHz in this study. The laser beam is split into two paths by a polarization beam splitter (PBS, PBS051, Thorlabs Inc). A half-wave plate (HWP1, GCL-060633, Daheng Optics) is placed before the PBS to

adjust the energy ratio of the two paths. One path transmits in free space. The other path is coupled into a 10-m polarization-maintaining single-mode optical fiber (PMF, HB450-SC, Fibercore) to delay the pulse by 50 ns. The 10-m fiber can be used as an optical delay line. With increased pulse energy, the 10-m PMF can also generate 558-nm wavelength via the SRS effect. Because the polarization state of the pump laser affects the SRS efficiency, a half-wave plate (HWP2) is placed before the 10-m PMF to adjust the polarization state. In sO_2 imaging, a bandpass filter (central wavelength: 558 nm, bandwidth: 10 nm, FB560-10, Thorlabs Inc) is placed after the 10-m fiber to pass the 558-nm wavelength and reject others. The two paths are combined with a 50/50 beam splitter (BS, BS010, Thorlabs Inc) and then delivered to an OR-PAM probe via a 2-m single-mode fiber (SM, P1-460B-FC-2, Thorlabs Inc). The fiber coupling efficiencies are above 50%.

In the OR-PAM probe, light from the 2-m fiber is focused by two achromatic doublets (AC064-013-A, Thorlabs Inc). An optical/acoustic beam combiner reflects the optical beam to the sample. Upon one trigger, the laser source excites two photoacoustic waves. Because of the 50-ns time delay, the two waves are partially overlapped. The photoacoustic waves are collimated by an acoustic lens (Stock #45-697, Edmund Optics), transmit through the optical/acoustic beam combiner, and are received by a piezoelectric transducer (V214-BC-RM, Olympus-NDT). The optical focus is coaxially and confocally aligned with the acoustic focus to optimize the detection sensitivity. The data acquisition card (ATS9360, Alazar Tech Inc) digitizes the signal with 12-bit resolution at 500 MHz (The minimum required sampling frequency is ~140 MHz). The scanning probe is mounted on a two-axis linear stage (L-509.10SD, Physik Instrumente), creating two-dimensional raster scanning to acquire a volumetric image.

14

The step size is 1.25 µm and one 2000^2 pixels figure takes about 16 minutes. The lateral resolution of this OR-PAM system is ~3.6 µm. The axial resolution, determined by the bandwidth profile of the ultrasonic transducer, is ~45 µm.

The dual-wavelength laser can operation at 1 MHz for each wavelength. Limited by the slow raster scanning module, the current OR-PAM system only achieves 4-kHz A-line rate. The short-delayed dual-wavelength laser and signal unmixing method is not limited to our current OR-PAM system. In the future, the method can be used in a fast-scanning system to demonstrate the imaging speed.
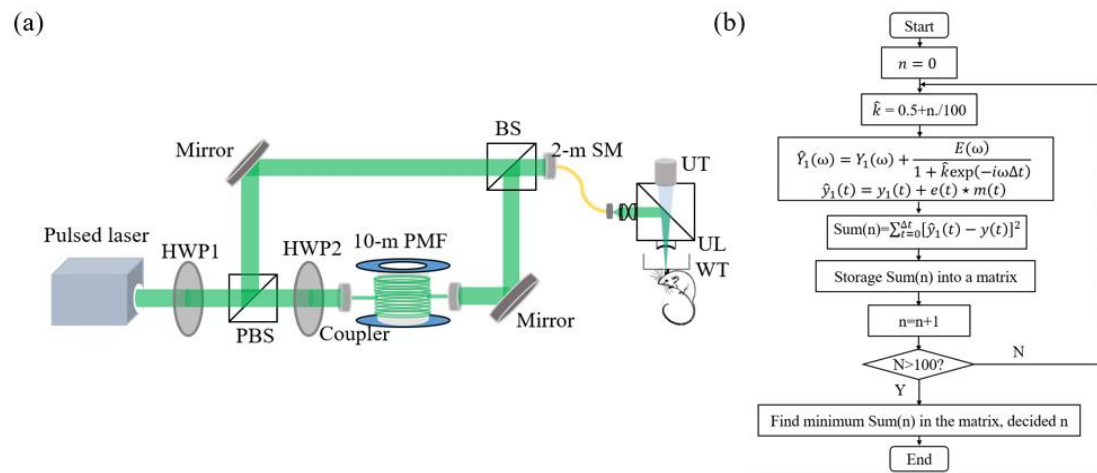
Figure 2-1 (a) Schematic of OR-PAM with ultrafast dual-wavelength excitation. BS, beamsplitter; HWP, halfwave plate; PBS, polarizing beamsplitter; PMF, polarization-maintaining fiber; SMF, single-mode fiber; UL, ultrasound lens; UT, ultrasound transducer; WT, water tank. (b) Flow chart of finding optimal k value.

2.2.2 Principle

The dual-wavelength excitation time interval corresponding to the 10-m PMF is 50 ns. If the imaging depth range is 300 µm, an A-line may last for about 200-ns. In this case, the two PA signals are partially overlapped. In sO_2 imaging, the blood at 532 nm and

558 nm usually has similar absorption coefficients. It is reasonable to assume that the two PA signals have the same waveforms. Their relationship can be expressed as

$$y_2(t) = ky_1(t - \Delta t) \tag{2-1}$$

where $y_1(t)$ and $y_2(t)$ are the first and second true PA signals, k is an unknown coefficient, and Δt is a known time delay between the two excitations. The detected PA signal $y(t)$ is an overlap of the two A-lines, which can be written as

$$y(t) = y_1(t) + ky_1(t - \Delta t) + e(t) \tag{2-2}$$

where $e(t)$ is a random measurement noise.

To separate the two partially overlapped signals, we apply Fourier transform to Eq. (2-2) and obtain

$$Y(\omega) = (1 + k\exp(-i\omega\Delta t))Y_1(\omega) + E(\omega) \tag{2-3}$$

We define $\hat{Y}_1(\omega) = \frac{Y(\omega)}{1+\hat{k}\exp(-i\omega\Delta t)}$, where $\hat{Y}_1(\omega)$ and $\hat{k}$ are estimated $Y_1(\omega)$ and k. If $\hat{k} = k$, $\hat{Y}_1$ becomes

$$\hat{Y}_1(\omega) = Y_1(\omega) + \frac{E(\omega)}{1+\hat{k}\exp(-i\omega\Delta t)} \tag{2-4}$$

Taking inverse Fourier transform of Eq. (2-4), we obtain

$$\hat{y}_1(t) = y_1(t) + e(t) \star m(t) \tag{2-5}$$

where the asterisk $\star$ denotes convolution operation, and $m(t)$ is the inverse Fourier transform of $[1 + \hat{k}\exp(-i\omega\Delta t)]^{-1}$.

16

Estimation of the A-line y_1 and k becomes an optimization problem

$$\min_{\hat{k}} \sum_{t=0}^{\infty} [\hat{y}_1(t) - y_1(t)]^2 \qquad (2\text{-}6)$$

Because y_1 is directly measured before the second laser pulse excitation, i.e., $y(t) = y_1(t) + e(t)$ for $t < \Delta t$, we change the optimization problem to

$$\min_{\hat{k}} \sum_{t=0}^{\Delta t} [\hat{y}_1(t) - y(t)]^2 \qquad (2\text{-}7)$$

Solving Eq. (2-7) allows us to separate the two signals and determine the amplitude ratio *k*. The calculating flow chart can be seen in Figure 2-1b.

2.3 Results and Discussion

2.3.1 Simulation

We simulate PA signal separation with different delay times. First, we acquire an A-line signal from a black tape sample with a single pulse excitation. To reduce noise, we average the signal by 1000 times. Then the A-line signal is multiplied by a constant coefficient k (varying from 0.74 to 1.32) and delayed by 10~60 ns. The delayed signal is added to the original A-line signal to simulate the overlapped dual-pulse PA signal. Figure 2-2 shows the signal separation results by simulation. An original short A-line signal (blue solid line) and a delayed copy (red dashed line) are shown in Figure 2-2a. Random Gaussian white noise (standard deviation is 0.014) is added to the overlapped signal, resulting in an SNR of 25 dB. Figure 2-2b shows the overlapped signal generated via adding up the original, delayed signals and same random Gaussian white noise. The Fourier-domain separation method is applied to the overlapped signal to recover the original and delayed signals, as shown in Figure 2-2c. We compute the correlation

coefficient between the separated results and the original ones to quantify their similarity. The correlation coefficients for the 1st and 2nd A-lines are 98.82% and 99.54%, respectively. The amplitude between the separated signals and original signals are also compared, as shown in Figure 2-2g. A paired t-test is employed between separated signals and true signals, the p-value is above 0.70. The peak-to-peak values of the separated signals are not significantly different from the true signals. Figure 2-2h compares the SNRs of the signals before and after separation, which shows that the averaged SNR is only reduced by ~1.2% after the separation. P-value between the two groups is above 0.5, indicating the reduction is insignificant. We then further test signal separation with different delay time from 10 to 60 ns based on short A-line signal. The SNR of the overlapped signal is 25dB. Figure 2-2i shows that we can correctly separate the signals with a delay as short as 18 ns (the overlap of two A-lines is about 90%). When the time delay between two signals is shorter than 18 ns (overlap over 90%), the separation efficacy starts to decline. Multi-layer absorption will generate long A-line PA signals, thus we also simulate separation for long A-line overlap PA signals. As shown in Figure 2d-f, similar results are acquired with short A-line signals; the amplitude exhibits 0.15% difference and the SNR decreases about ~1.4%.
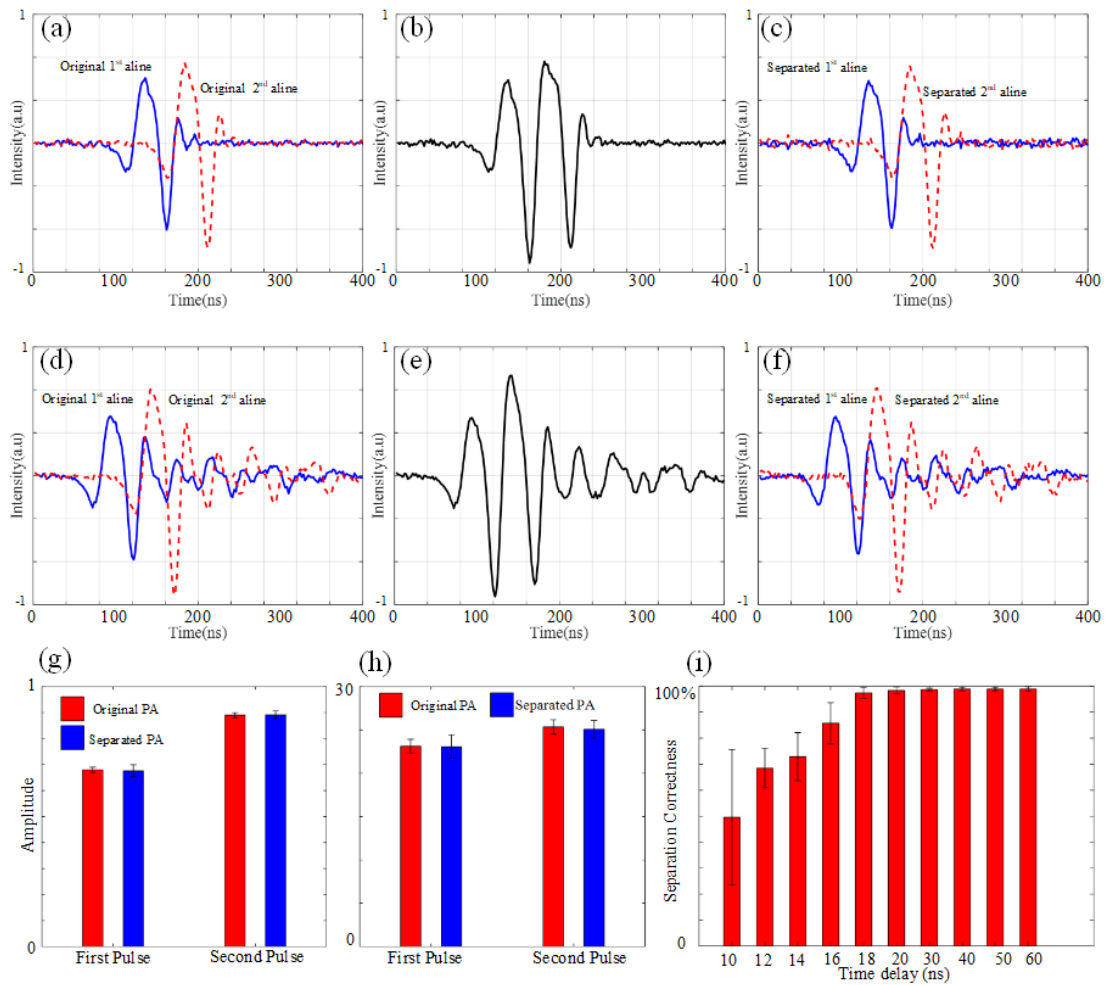
Figure 2-2 Simulation of signal separation. (a)-(c) Simulation results of broadband PA signals. (a) An acquired A-line excited with one pulse (blue solid line) and its delayed copy (red dashed line). The copy is delayed by 50 ns and multiplied by k. (b) Summation of the two signals to simulate dual-pulse PA excitation. (c) Separated first signal (blue solid line) and separated second signal (red dashed line). (d)- (f) Simulation results of narrowband PA signals. (d) An acquired A-line excited with one pulse (blue solid line) and its delayed copy (red dashed line). The copy is delayed by 50 ns and multiplied by k. (e) Summation of the two signals to simulate dual-pulse PA excitation. (f) Separated first signal (blue solid line) and separated second signal (red dashed line). (g)- (i) Comparison corresponding to

(a)-(c). (g) Comparison of amplitudes of separated signals with the original ones. (h) Comparison of SNRs between separated signals and original signals. (i) Separation correctness with different level overlap. Error bars are standard deviation, and the sample size is 20.

2.3.2 Phantom experiment

Phantom experiments are conducted to further validate the signal separation method. Figure 2-3a shows an experimental dual-pulse overlapped PA signal generated from a black tape sample. SNR of the overlapped signal is 31 dB. The time delay between the two excitations is 50 ns. Using the proposed separation method, the first (blue solid line) and the second (red dashed line) PA signals are recovered and shown in Figure 2-3b. The amplitude of the second PA signal is 1.14 times of the first one (k=1.14). To verify the separation results, the first and second PA signals are measured separately with traditional single-pulse excitations. The measured single-pulse PA signals are shown in Figure 2-3c. The correlation coefficients between the measured and separated PA signals are 0.979 for the first signal and 0.976 for the second signal. Figure 2-3d and 2-3e show the comparison of amplitudes and SNRs between the two sets of signals. The separated signals have the insignificant (0.17%) different peak-to-peak values and 1.4% lower SNR than the measured signals. We further investigate the separation method at different SNRs. As shown in Figure 2-3f, the separation accuracy increases with the improved SNR. The correlation coefficients between the separated and the directly measured signals are higher than 94% when the SNR is above 23 dB. When the overlapped signal's SNR is greater than 30dB, the correlation coefficient is close to 100%. When the SNR of the overlapped signal is below 18 dB, the separated signals have low similarity (< 58%) with the true signals.

Because the time delay between the two pulses is only sub-microseconds, the Grueneisen parameter may change due to instantaneous local heating [71]. We test the increase of the Grueneisen parameter in the dual-pulse excitation. The time delay between the two pulses is 50 ns. The pulse energies are both 50 nJ, which can excite PA signals with a high SNR (> 36dB). In the experiment, the second PA signal of a black tape sample is measured with and without the first pulse excitation. The second PA amplitude with the first pulse excitation is 0.8% higher than the one without the first pulse excitation. Therefore, we can conclude that, with a reasonably high SNR, the Grueneisen parameter is not changed significantly in the dual-pulse excitation.
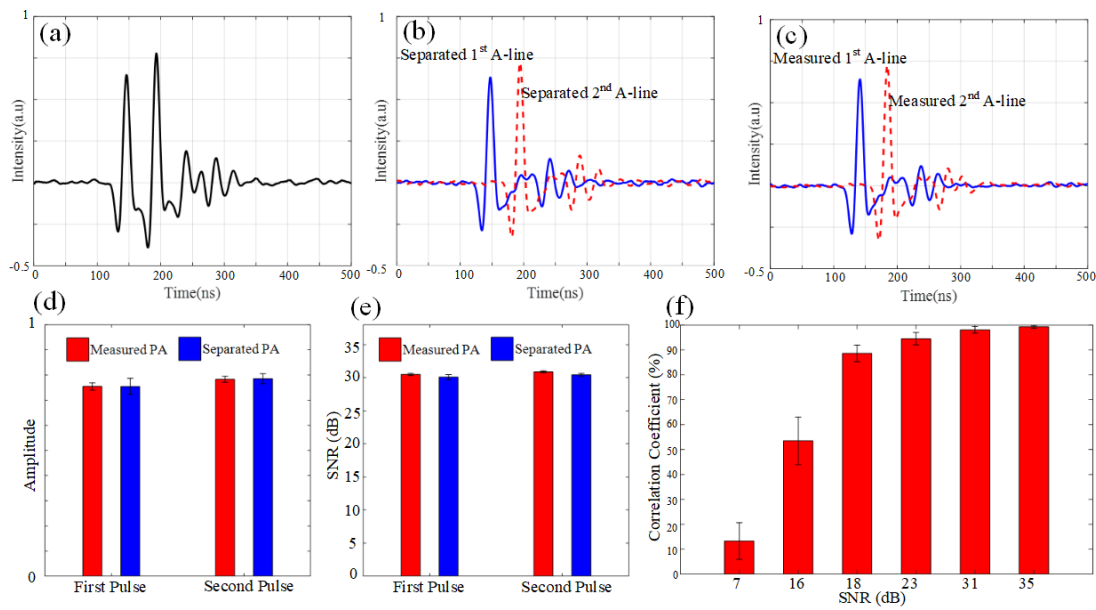
Figure 2-3 (a) Dual-pulse overlapped PA signal obtained in an experiment. (b) Separated first (blue solid line) and second (red dashed line) PA signals. (c) Directly measured first (blue solid line) and second (red dashed line) PA signals. The two signals are measured separately and thus have no overlapping. (d) Comparison of amplitudes between the separated signals in (c) and the measured signals in (d). The difference of peak-to-peak values is not significant (paired t-test

is employed between separated signals and measured signals, p-value all above 0.75). (e) Comparison of SNRs between the separated signals in (c) and the measured signals in (d). (f) The correlation coefficient between the separated and the measured signals at different SNRs of the overlapped signals. Error bars are standard deviation, and the sample size is 20.

2.3.3 *In vivo* experiment

We apply the Fourier-domain signal separation method to ultrafast dual-wavelength excitation in functional OR-PAM of mouse ears. All procedures in the animal experiments were approved by the animal ethical committee of the City University of Hong Kong. Two wavelengths, 532 nm and 558 nm, are switched in 50 ns. The pulse energy is 50 nJ for both wavelengths. The field of view is about 4.75×3.25 mm^2. The overlapped A-lines are acquired. We use the Fourier-domain method to separate an overlapped PA signal to two A-lines and determine an optimal amplitude ratio (the k value) between the two A-lines. Figures 2-4a and 2-4b show the separated images at 532 and 558 nm, respectively. Based on the separation results, we determine the oxygen saturation using [72]

$$sO_2 = \frac{\varepsilon_{de}(\lambda_{558})PA(\lambda_{532}) - \varepsilon_{de}(\lambda_{532})PA(\lambda_{558})}{[\varepsilon_{ox}(\lambda_{532}) - \varepsilon_{de}(\lambda_{532})]PA(\lambda_{558}) - [\varepsilon_{ox}(\lambda_{558}) - \varepsilon_{de}(\lambda_{558})]PA(\lambda_{532})} \qquad (2\text{-}8)$$

where ε_{ox} and ε_{de} are the molar extinction coefficients of oxy- and deoxyhaemoglobin, respectively, PA is the separated signal amplitude at different wavelengths. The sO_2 image is shown in Figure 2-4c. Figure 2-4d is another sO_2 image of the same region measured without using the signal separation, i.e., the 532-nm and 558-nm pulses are separated by 200 ns and thus do not cause overlapping in A-lines. From Figures 2-4c

and 2-4d, we can clearly distinguish the arteries and veins. Figure 2-4e shows the averaged sO_2 values in three artery-vein pairs as labelled in Figure 2-4c and 2-4d. The SNR is above 18 dB. The difference between the sO_2 values obtained with the two methods is not significant, validating that the signal separation method can be applied to *in vivo* sO_2 imaging. The ultrafast dual-wavelength excitation enables the use of a short optical delay fiber and thus allows generating high pulse energy in stimulated Raman scattering laser.
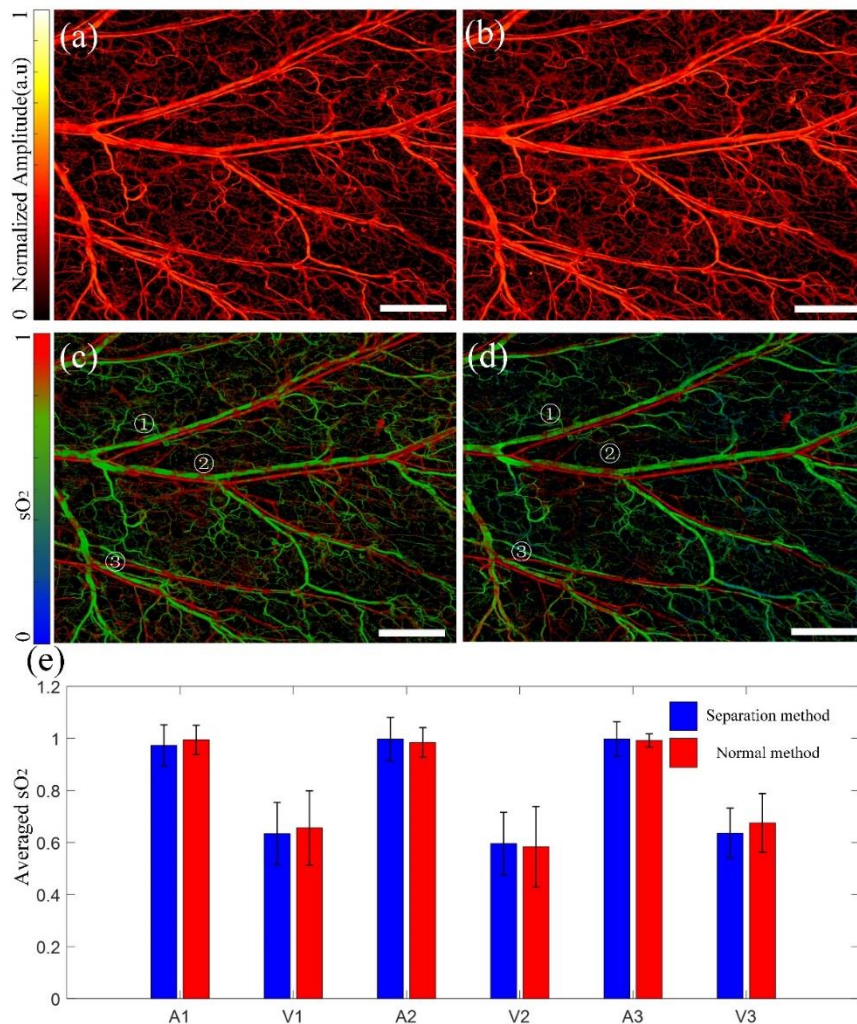
Figure 2-4 *In vivo* OR-PAM of oxygen saturation with ultrafast dual-wavelength excitation. The first and second pulses are 532 nm and 558 nm. The time delay

between them is 50 ns. (a) Separated first PA image (532-nm) of the mouse ear. (b) Separated second PA image (558-nm) of the mouse ear. (c) Oxygen saturation image of the mouse ear calculated from the separated data. (d) Oxygen saturation image of the same mouse ear calculated from two single-pulse excitation data at 532 and 558 nm, respectively. The two pulses are delayed by 200 ns and thus have no overlapping in A-lines. (e) Comparison of the sO_2 values in three artery-vein pairs measured with the two methods. The artery-vein pairs are labelled in (c) and (d). Scale bar: 800 μm.

2.4 Conclusion

In this chapter, we present a new OR-PAM technique that enables dual-wavelength excitation as fast as 50 ns. Via stimulated Raman scattering and an optical fiber delay line, we can excite two PA signals of different optical wavelengths in tens of nanoseconds. The two PA signals may have significant overlapping. To address this issue, we develop a Fourier-domain signal separation method to recover the two PA signals. We assume that the two PA signals have the same waveform, so that the amplitude ratio between the two signals can be determined via solving an optimization problem. We validate the method with numerical simulation and phantom experiments. The partially overlapped PA signals can be separated with good accuracy. With a reasonably good SNR, the separated two signals have the same peak-to-peak values with the true signals, and the SNR only reduces by ~1.4%. Applying this method to *in vivo* OR-PAM, we demonstrate functional OR-PAM of oxygen saturation in the mouse ear. The results are comparable with the ones from conventional OR-PAM with long dual-wavelength excitation time. The ultrafast dual-wavelength excitation enables functional OR-PAM with reduced misalignment among different wavelengths. This

technique can potentially increase the pulse energy in SRS laser due to the short fiber length, which is beneficial to functional OR-PAM, such as brain imaging and single-red-blood-cell imaging, which requires high sensitivity and precise alignment among different wavelengths.

3 ULTRAFAST OPTICAL-RESOLUTION PHOTOACOUSTIC MICROSCOPY FOR SINGLE-SHOT LINEAR DICHROISM DETECTION

This chapter is reproduced with some adaptations from the manuscript "Yingying Zhou, Jiangbo Chen, Chao Liu, Chengbo Liu, Puxiang Lai and Lidai Wang, "Single-shot linear dichroism optical-resolution photoacoustic microscopy". Photoacoustics 16, 100148, 2019. The contributions of authors are as follows: L. Wang, P. Lai conceived the idea. Y. Zhou, J Chen, C Liu and L. Wang designed the system. Y. Zhou ran the experiments. Y. Zhou, P. Lai and L. Wang prepared the manuscript. All authors were involved in the analysis of the results and manuscript revision.

In this Chapter, a new ultrafast three-wavelength OR-PAM technique modified from the system presented in Chapter 2 is introduced. Based on the short fiber delay mechanism, we establish a dichroism detection system. Dichroism is a material property that causes anisotropic light-matter interactions for different optical polarizations. Dichroism relates to molecular types and material morphology and thus can be used to distinguish different dichroic tissues. In this chapter, we present single-

shot dichroism photoacoustic microscopy that can image tissue structure, linear dichroism, and polarization angle with a single raster scanning. We modify the fiber-based laser system to split one laser pulse into three with different polarization angles, sub-microseconds time delay, and identical pulse energy. A dual-fiber OR-PAM system is developed to acquire three A-lines per scanning step. In such a way, dichroism imaging can achieve the same speed as single-wavelength photoacoustic microscopy. Moreover, the three polarized pulses originate from one laser pulse, which decreases pulse energy fluctuations and reduces dichroism measurement noise by ~35%. The new dichroism photoacoustic imaging technique can be used to image endogenous or exogenous polarization-dependent absorption contrasts, such as dichroic tumor or molecule-labelled tissue.

3.1 Introduction

Dichroism refers to anisotropic optical absorption property for different light polarizations. This property closely relates to molecular type and alignment. Dichroism can be determined via measuring absorption of different polarized irradiations with respect to the molecular or structural axis [73, 74]. Dichroism detection can probe molecular types and structures of some biopolymers (such as protein and DNA) and synthetic polymers [75-78].

As an emerging optical imaging technique, PA tomography has seen a wide range of applications, including imaging dichroism in biological tissue. PA imaging also shows great potentials to provide multiple optical properties by being integrated with other optical modalities [79-81]. PA signal is proportional to absorbed optical energy [4, 8, 60, 82-84] and, thus, provides a sensitive approach to measure dichroism. Dichroism-

sensitive OR-PAM was first reported by Hu *et al.* [66]. In Hu's work, the OR-PAM system detects linear dichroism of amyloid plaques. An electro-optical modulator (EOM) alternates two perpendicularly polarized excitation beams pulse by pulse. While promising, two polarized beams are not enough to fully quantify the linear dichroism. In addition, the delay time between the two perpendicularly polarized pulses is the laser pulse repetition period. The misalignment between the two polarizations is half step size, which may cause errors in dichroism imaging [56, 61]. Qu *et al.* realized dichroism imaging in PACT [85]. The polarization directions of dichroic materials, i.e., linear polarizers and bovine tendons, were successfully identified at depths of several transport mean free paths. Zhang *et al.* [86] developed a quantitative method to determine the dichroism from the anisotropy value. Both methods rotate a half-wave plate (HWP) to control the laser polarization and are time-consuming. This may be problematic in high-speed imaging.

In this chapter, we develop a new OR-PAM technique that can measure linear dichroism in a single shot. The fast polarization measurement reduces misalignment among different polarized excitations, especially in fast scanning OR-PAM. In addition, the three different polarized laser pulses are generated from a single laser pulse, significantly reducing the energy fluctuation between the three pulses.

3.2 Method

3.2.1 System Setup

A linear dichroism OR-PAM schematic is shown in Figure 3-1, which is modified based on the system developed in Chapter 2. A 532-nm pulsed laser (7 ns pulse width, linear polarization, VPFL-G-20, Spectra-Physics) is used as the photoacoustic excitation

source. The output laser beam is split into three paths using two sets of polarizing beam splitters (PBS1 and PBS2) and halfwave plates (HWP1 and HWP3). The halfwave plates adjust the energy ratio among the paths. One laser path is delivered to an OR-PAM probe via a 2-m polarization-maintaining fiber (PMF, single mode, P1-488PM-FC-2, Thorlabs). The other two paths go through two polarization maintaining fibers (PMF, 30-m and 60-m long, respectively, single mode, HB450-SC, Fibercore) to generate different time delays. Then the two delayed paths are combined at a polarizing beamsplitter (PBS3) and delivered to the OR-PAM probe via another 2-m PMF (single mode, P1-488PM-FC-2, Thorlabs). The polarization directions of the two paths are aligned with the fast and slow axes of the 2-m PMF, respectively. At the output end, the two 2-m PMFs are connected to the probe with two fiber adapters, and the angle between the fast axes of the two 2-m PMFs is 45°, so that we obtain three laser pulses with three different polarizations: 0°, 45°, and 90°. The three laser pulses have ~150-ns time interval and unchanged pulse energy ratio among them, the pulse energy for each pulse is around 30 nJ. In the imaging probe, the two laser beams from the fibers are collimated with an achromatic lens (AC064-013-A, Edmund) and then combined with a beamsplitter. Another achromatic lens (AC064-013-A, Edmund) focuses the combined beam. Then the focused beam is reflected in an optical/acoustic beam combiner (2 aluminium-coated prism) [87], transmits through an ultrasonic lens, and illuminates the sample. Optically induced ultrasonic waves are collected by the ultrasonic lens, transmit through the optical/acoustic beam combiner, and are received by a 50-MHz piezoelectric transducer (V214-BC-RM, Olympus-NDT). Optical excitations from the two fibers are both aligned with the acoustic detection coaxially and confocally to maximize the detection sensitivity. This OR-PAM system acquires

three A-lines with different polarized excitations at every scanning step. Raster scanning the PA probe allows for acquiring volumetric images. The step size is 1.25 µm and one 1000^2 pixels figure takes about 4 minutes.
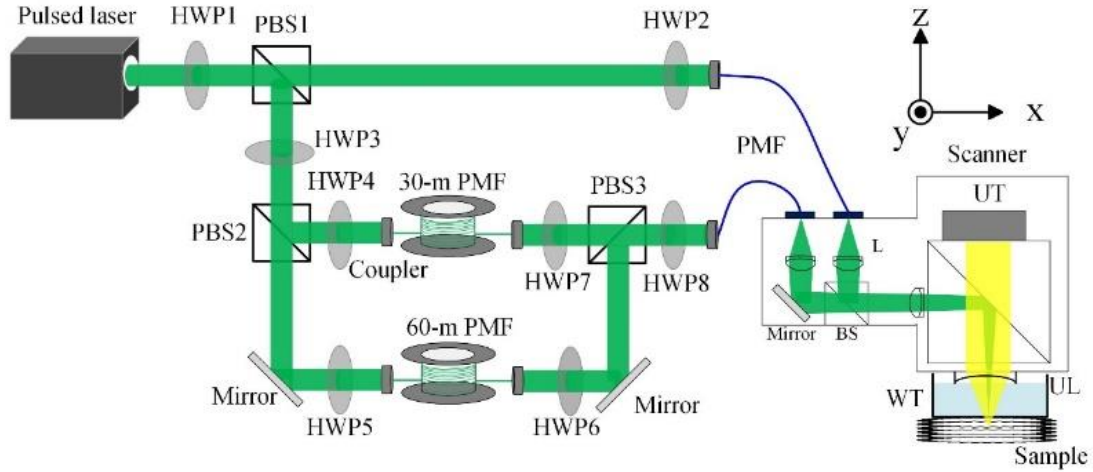
Figure 3-1 Schematic of the dual-fiber single-shot dichroism OR-PAM system. BS, beamsplitter; HWP, halfwave plate; L, lens; PBS, polarizing beamsplitter; PMF, polarization-maintaining fiber; UL, ultrasound lens; UT, ultrasound transducer; WT, water tank.

3.2.2 Principle

Principle of the linear dichroism measurement is presented as follows. In linear photoacoustic range, the initial pressure can be expressed as [71, 88, 89]

$$p = \Gamma \eta_{th} \, \mu_a F \tag{3-1}$$

where Γ is the Grueneisen parameter, η_{th} is the heat conversion efficiency, μ_a is the absorption coefficient, and F is the optical fluence. If the sample is dichroic, μ_a varies with the excitation polarization angle. For dichroic samples, assuming the optical axis

orientation is θ, the polarization angle of light is φ. The μ_a depends on θ and φ as [66]

$$\mu_a(\theta, \varphi) = \frac{\mu_p + \mu_v}{2} + \frac{\mu_p - \mu_v}{2}\cos(2\varphi - 2\theta) \tag{3-2}$$

where $\mu_a(\theta, \varphi)$ is the absorption coefficient when optical axis for target is θ and the polarized angle for light is φ. μ_p and μ_v are the optical absorption coefficient of the direction parallel with and perpendicular to the optical axis, respectively.

If we measure PA signals with three linear polarized pulses at 0°, 45° and 90°, we obtain

$$\begin{cases} p(\theta, 0^o) = \Gamma\eta_{th}F\left[\frac{\mu_p + \mu_v}{2} + \frac{\mu_p - \mu_v}{2}\cos(0^o - 2\theta)\right] \\ p(\theta, 45^o) = \Gamma\eta_{th}F\left[\frac{\mu_p + \mu_v}{2} + \frac{\mu_p - \mu_v}{2}\cos(90^o - 2\theta)\right] \\ p(\theta, 90^o) = \Gamma\eta_{th}F\left[\frac{\mu_p + \mu_v}{2} + \frac{\mu_p - \mu_v}{2}\cos(180^o - 2\theta)\right] \end{cases} \tag{3-3}$$

For simplicity, we let the three pulses have the same fluence. The dichroism is defined as $\left|(\mu_p - \mu_v)/(\mu_p + \mu_v)\right|$ [66]. Solving Eq. 3-3, we can determine the dichroism and polarization angle from the three PA measurements.

$$\theta = \frac{\arccos\left[\frac{p(\theta,0^o) - p(\theta,90^o)}{\left(2\times\left[(p(\theta,0^o) - p(\theta,45^o))^2 + (p(\theta,90^o) - p(\theta,45^o))^2\right]\right)^{\frac{1}{2}}}\right]}{2} \tag{3-4}$$

3.3 Results and Discussion

3.3.1 Comparison between a linear polarizer and a black ink sample

Figure 3-2 shows dichroism OR-PAM of a linear polarizer and a black ink sample (unpolarized). Figure 3-2a shows the PA images at three polarization angles. The upper row is the results from the linear polarizer sample, whose polarization angle is 135°.

The lower row is the black ink sample. The linear polarizer results show obvious different PA intensities at different polarized excitations. The PA intensity at 45° excitation is lower than the other two, and the PA images at 0° and 90° excitations are nearly the same. Because the black ink has no dichroism, the PA images shows no obvious differences at different polarized light excitations. Dichroisms are calculated and shown in Figure 3-2b. The averaged dichroism value for the linear polarizer is 0.96±0.003, and the value for the black ink sample is nearly 0. We validate the dichroism of the linear polarizer in transmission mode using a power meter. The extinction ratio of the polarizer equals to 0.99, which is close to the PA imaging result.
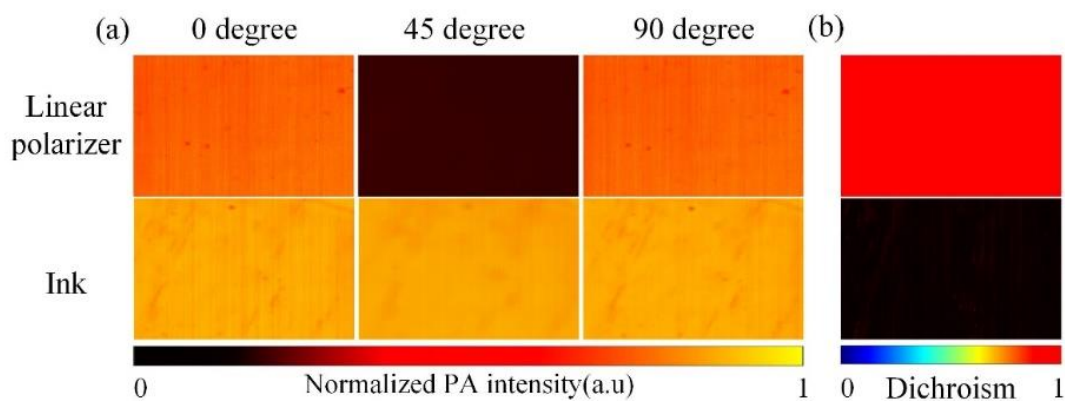
Figure 3-2 (a) Linear polarizer (upper) and black ink (lower) images at 0°, 45°, and 90°. (b) Calculated dichroism of the linear polarizer (upper) and the black ink (lower) samples.

3.3.2 Phantom experiment

To verify the dichroism imaging, three linear polarizers are positioned in different angles, as shown in Figure 3-3. Figure 3-3a shows three PA images acquired with three polarized light excitations. The polarizer gives strongest PA signals when its polarization angle aligns with the polarization angle of the excitation light. Figure 3-3b

shows the computed dichroism of the three linear polarizers. As expected, their dichroism is the same regardless their orientations. Figure 3-3c shows the computed polarization angles θ according to Eq. 3-4. These results demonstrate that our single-shot OR-PAM can image dichroism correctly.
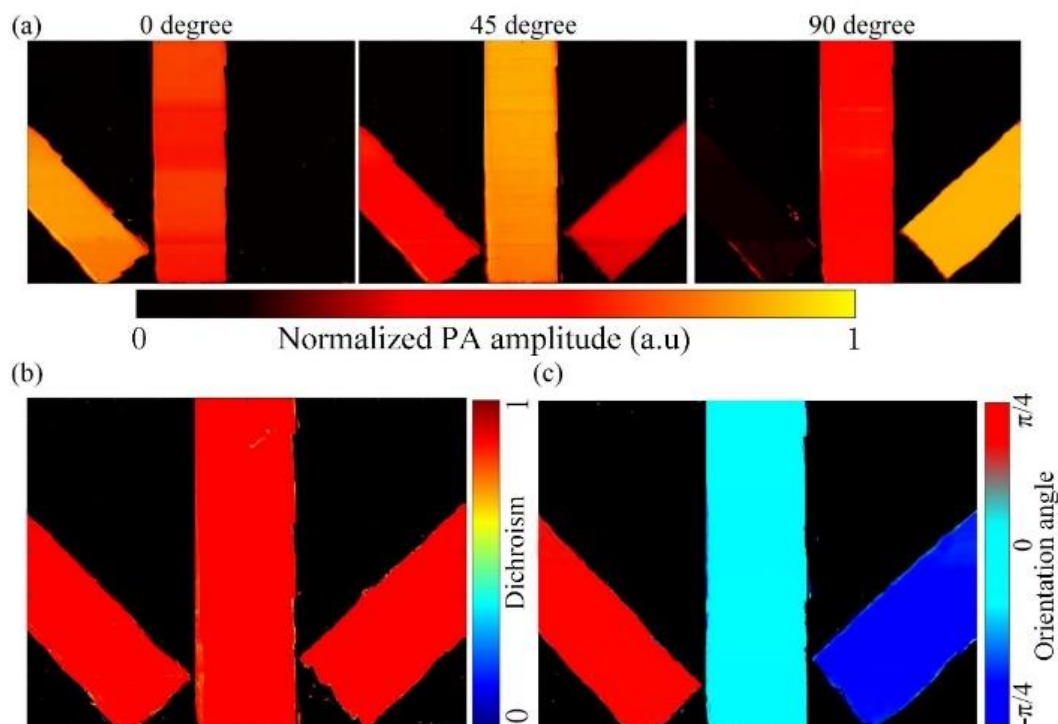
Figure 3-3 (a) PA images of three linear polarizers excited with polarized light at 0º, 45º, and 90º. (b) Calculated dichroism image of the three linear polarizers. (c) Calculated polarization angle of the three linear polarizers.

An alternative approach is to measure the dichroism from three independent pulses. Compared with the independent-pulse method, our single-shot approach measures three PA signals originating from one laser pulses and thus reduces pulse energy fluctuations. In Figure 3-4, we show the standard deviation of the detected dichroism as a function of scanning step size. As seen, with EOM-based method [66], the standard deviation

increases with the step size almost linearly, as the larger the step size, the larger is the discrepancy in the spatial position involved in the dichroism detection. Therefore, such a system is not suitable for large step size. Otherwise, the detection accuracy cannot be ensured. In comparison, in our dichroism system, the detection standard deviation remains nearly constant for different step sizes. The fiber delay setting can also get rid of the laser output fluctuation due to the subtraction of three daughter paths in the dichroism calculation. The standard deviations of the dichroism results from the single-shot approach is 0.0455, which is 35% less than the independent-pulse method.
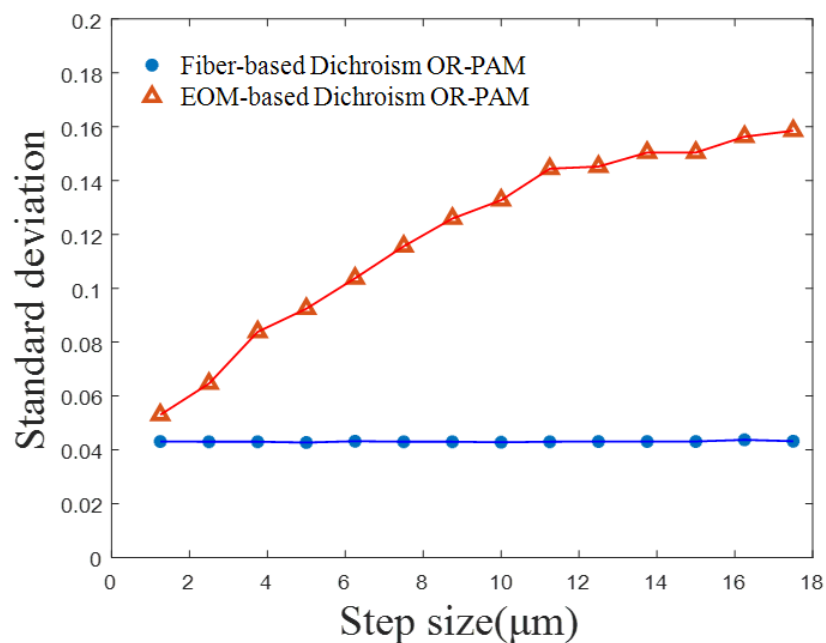
Figure 3-4 Standard deviation of detected dichroism as a function of raster scanning step size for one pulse per position (red triangle) and three pulses per position (blue circles) approaches.

3.3.3 Tissue experiment

We further demonstrate single-shot dichroism OR-PAM with biological tissue. Congo Red dye is a dichroic molecule. In experiment, 0.01g Congo Red (C8450, Solarbio) was dissolved in 0.2 ml deionized water, and was used to dye a ~200-µm-thick chicken breast tissue sample. First, we tested photo bleaching rate of the labelled sample in OR-PAM imaging. The laser pulse energy in experiment was 30 nJ. The averaged PA amplitude decreases ~58% per one million pulsed excitations. For raster scanning, the laser spot size is 5 µm and the step size is 1.25 µm. Thus, the sample bleaching at one spot is 0.002784% for three pulsed excitations. Thus, photo bleaching causes negligible influence to the single-shot dichroism imaging.

Figure 3-5a shows a maximum-amplitude-projected PA image of the chicken breast sample. The polarization angle of the excitation light for this image is 0°. The laser repetition rate is 8 kHz for each polarization angle. The scanning step size is 1.25 µm, and the field of view is 1.25×1.25 mm^2. Figure 3-5b shows the spatial profile of averaged PA amplitudes along the B-scan direction at three excitation polarization angles. Dichroism of the sample causes dramatic differences among the three images. Because the time delay among the three pulses is sub-microseconds, the Grueneisen parameter might be changed due to local heating [71, 88, 89]. To exclude this possibility, we use two non-polarized laser pulses to excite the sample. The two pulses have the same pulse energy of 30 nJ. The time delay between them is ~150 ns. As seen in Figure 3-5c, the PA amplitude variation associated with the Grueneisen effect does exist, as the second PA amplitude increases ~3% due to local heating. Nevertheless, compared with polarization difference-induced difference (~25% variation for each different polarization) shown in Figure 3-5b, the Grueneisen effect causes ~12% error in the

dichroism measurement. In the future, this error may be reduced via increasing the time delay among the three pulses or using less pulse energy. Figure 3-5d and 3-5e show the dichroism and polarization angle distributions of the Congo Red-dyed chicken breast tissue sample. The dichroism of the sample is relatively uniform due to the use of the same dye. The polarization angle distribution, however, shows more variations due to the inhomogeneities of muscle fiber directions.
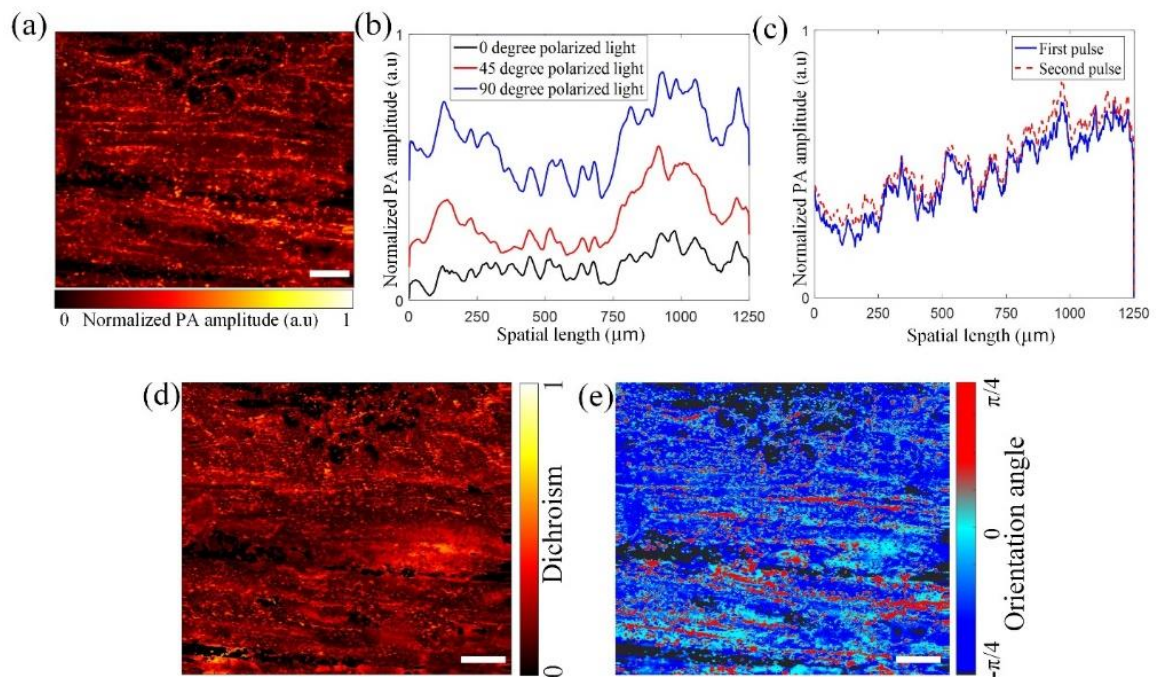
Figure 3-5 OR-PAM of a Congo-Red-dyed chicken breast tissue sample. (b) Averaged PA amplitudes excited with different linear polarization light at 0⁰, 45⁰, and 90⁰. (c) Test of Grueneisen relaxation effect. Averaged PA amplitudes excited with two non-polarized pulses. Time delay between the two pulses is 150 ns. (d) Calculated dichroism image. (e) Calculated polarization angle image. (Scale bar: 150 μm).

Therefore, with our proposed setup, one is able to achieve two-dimensional optical-resolution PA microscopic images of different polarizations with tunable step sizes. On top of that, dichroism PA microscopic images can be formed, from which one can tell if the material of the target is dichroic or not, or distinguish a dichroic object from a non-dichroic background. To demonstrate that, a hybrid sample was prepared, with the upper part made of black ink-dyed white paper and the lower part Congo Red-dyed chicken breast tissue. From the normal PAM (Figure 3-6a), the chicken and paper expressed similar PA features in terms of signal amplitude, and one cannot tell which part has the dichroic effect. From the dichroism PAM (Figure 3-6b), however, the two parts showed totally different features; the dichroic effect of the chicken was obvious, being around 15%, while the papers showed almost no dichroism. The quantified results of normal PAM and dichroism are shown in Figure 3-6c and d, respectively. The signals difference in normal PAM is tiny compared the obvious varieties in dichroism PAM. Moreover, structural fine features of the dichroic target (chicken tissue) shown in normal PAM still existed or even enhanced in the dichroism PA image due to a suppressed non-dichroic background (paper).
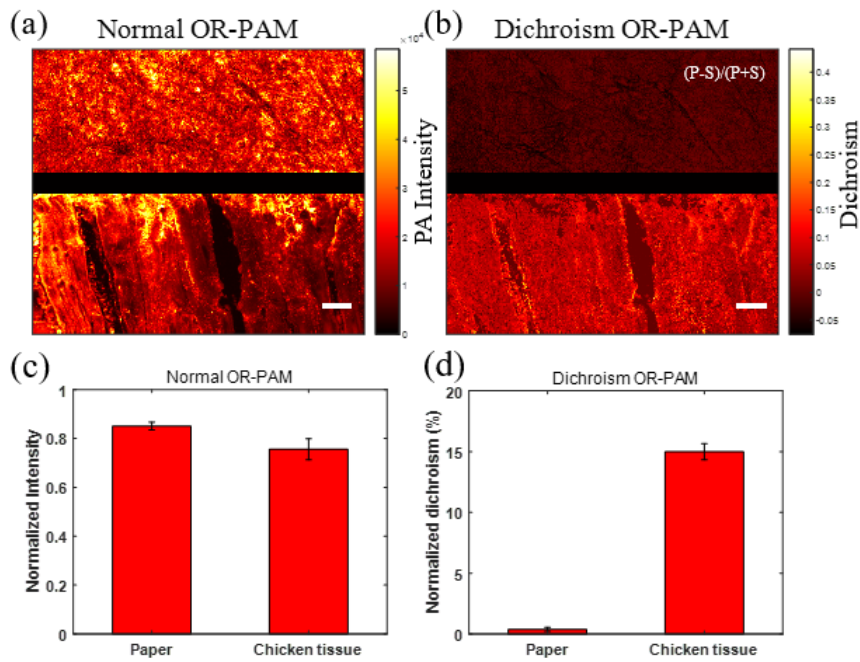
Figure 3-6 Normal (a) and dichroism (b) photoacoustic imaging of a hybrid sample composed of black ink-dyed white paper (upper part) and Congo Red-dyed chicken breast tissue (lower part). The scale bar represents 200 µm. (c) Quantified results in corresponding to (a). (d) Quantified results in corresponding to (b).

3.4 Conclusion

We present the development of a single-shot linear dichroism OR-PAM. To quantify the linear polarization, the OR-PAM system excites the sample with three laser pulses at different polarization angles. One laser pulse output of a fiber-based laser source is split into three with different polarization angles and different time delays. This approach provides stable energy ratio among the three pulses and thus can reduce the noise in dichroism imaging. Polarization switch is implemented via fiber delay. This offers sub-microseconds polarization switching and thus can reduce misalignment among different polarizations, even in fast scanning. The three laser pulses are delivered to a dual-fiber OR-PAM probe for PA imaging. Experimental results show

that dichroism OR-PAM can quantify dichroism and polarization angle in a single raster scanning. This technical advancement offers a new polarization contrast to optical-resolution photoacoustic microscopy and may extend it to broader preclinical and clinical applications.

4 Photoacoustic Imaging of Microenvironment Changes in Facial Cupping Therapy

This chapter is reproduced with some adaptations from the manuscript "Yingying Zhou, Fei Cao, Huanhao Li, Xiazi Huang, Dongshan Wei, Lidai Wang, and Puxiang Lai, "Photoacoustic imaging of microenvironmental changes in facial cupping therapy". Biomedical Optics Express 11 (5), 2394-2401, 2020. The contributions of authors are as follows: P. Lai and Y. Zhou conceived the idea. Y. Zhou, F. Cao, and X. Huang designed the system. Z. Yu, F. Cao ran the experiments. Z. Yu, F. Cao, H. Li, L. Wang and P. Lai prepared the manuscript. All authors were involved in the analysis of the results and manuscript revision.

This chapter describes the second application based on the fiber-based ultrafast OR-PAM system developed in Chapter 2. As a traditional medicine practice, cupping therapy has been widely used to relieve symptoms like fatigue, tension, and muscle pain. During the therapy, negative pressure is applied to the skin for certain duration with an intention to enhance blood circulation or induce micro-bleeding. The therapeutic effect, however, is not clear due to the lack of direct quantification. Aiming at quantitative assessment of the treatment effect, we apply OR-PAM in monitoring the structural and functional changes after cupping. We find that, after 5-minute of ~20 kPa

negative pressure cupping, more capillaries appear in the focus, and micro-blooding is observed from the capillaries. We quantify the images and find the blood vessel density is increased by 64%, and the total hemoglobin concentration in both the veins and the arteries exhibits 64% and 40% elevation, respectively. Oxygen saturation in the vein and artery decreases by 17% and 3% right after cupping, respectively. After two hours of recovery, the three blood-related parameters return to their original levels, indicating the effects in the tissue last only a short period after cupping at the given pressure and time duration. Note that no significant cupping marks are induced with the treatment parameters in this study. This work proposes OR-PAM to quantitatively monitor and evaluate the effect of cupping therapy from the perspective of imaging. The method is also useful for accurate control of the therapeutic outcome.

4.1 Introduction

Cupping therapy is a traditional medicine practice that applies negative pressure to the skin, leading to increased blood circulation or micro-bleeding in local tissue. It is claimed that cupping can increase capillary permeability, enhance tissue gas exchange, promote blood circulation, and relieve symptoms like fatigue, tension, and muscle pain [90, 91]. After cupping treatment, marks caused by capillary expansion or micro-bleeding may appear on the skin surface. They usually exhibit skin protrusions of different colours, yet sometimes bleeding points and blisters may show up due to excessive negative pressure and long treatment time [92].

Cupping therapy has been used for thousands of years to relieve soreness and pain [93]. Nowadays, the clinical practices of cupping have extended, such as to treat herpes zoster, acne vulgaris, cervical spondylosis, cough, scapula, periarthritis of the shoulder

and facial paralysis [94-104]. However, due to the lack of quantitative assessment tools, the effectiveness, the optimal negative pressure and time duration of cupping therapy have not been thoroughly studied. Recently, some researchers have interpreted cupping therapy from the perspective of microenvironment changes based on parameters obtained from optical sensing tools. For example, in 2017, Li *et al.* used near-infrared spectroscopy to investigate the hemodynamics in the tissue around the cupping site [105]. A significant drop in deoxyhemoglobin but an elevation in oxyhemoglobin was recorded, indicating an enhancement of oxygen uptake around the cupping site. Right at the cupping site, in 2019 the same team reported increased deoxyhemoglobin but declined oxyhemoglobin [106]. The results from these two studies are quite consistent, suggesting improved blood circulation due to the cupping treatment. Similar measurements were repeated by Jae Gwan *et al*., who embedded an optical sensor within the therapy cup to monitor the hemodynamic changes during cupping [107]. They observed elevation of both deoxyhemoglobin and oxyhemoglobin at the cupping site but drop of both parameters at the surrounding positions, confirming cupping can increase the oxygen and blood supplement to cupping site.

Although promising, the aforementioned studies are based on optical sensing, which results in spatially averaged measurements. It is preferred if the microenvironment parameter changes can be spatially resolved and mapped to the micro-circulation system. Therefore, high-resolution optical imaging is desired for cupping assessment. Taking advantage of optical absorption contrast and subcellular spatial resolution, OR-PAM is exploited in this study to image the microenvironmental changes [4, 83, 84, 108-111] in cupping. OR-PAM can provide label-free quantitative imaging of the micro-vessels and oxygen saturation *in vivo* [59, 60]. Cupping with low negative

pressure and photoacoustic (PA) imaging is performed on the mouse ear. The dynamic change in the treated tissue is recorded using OR-PAM. Structural and functional parameters, including the total hemoglobin concentration, vascular density, and oxygen saturation, are quantitatively monitored from the images in the whole process of cupping.

4.2 Method

A schematic of OR-PAM is shown in Figure 4-1a. A 532-nm pulsed laser (7 ns pulse width, VPFL-G-20, Spectra-Physics) provides the excitation laser source. The 532-nm laser beam is divided into two paths by a polarizing beamsplitter (PBS1, PBS051, Thorlabs Inc). A half-wave plate (HWP1, GCL-060633, Daheng Optics) is placed before the PBS to adjust the energy ratio between the two daughter paths. One path transmits in free space, with a half-wave plate (HWP3) and a polarization beamsplitter (PBS2) to produce a small portion of the light to be sampled by a photodiode to monitor and compensate for the laser fluctuations. The other path is coupled into a 100-m multimode fiber (MMF, GIMMSC(50/125)P, Fibercore) to generate a 558-nm wavelength via the Stimulated Raman Scattering (SRS) effect [70, 112]. To maximize the SRS efficiency, another half-wave plate (HWP2) is put before the 100-m fiber to tune the polarization state of the input beam. In addition, the 100-m MMF causes ~500-ns delay with respect to the other path. In order to pass the 558-nm wavelength and reject others, a band-pass filter (central wavelength 558 nm, bandwidth 10 nm, FB560-10, Thorlabs Inc) is placed after the MMF. The two laser beams are recombined by a dichroic mirror (T550lpxr-UF1, CHROMA). The combined beams are coupled into a 2-m single-mode fiber (SM, P1-460B-FC-2, Thorlabs Inc) and delivered to the OR-PAM probe. The two sequential laser pulses at 532 nm and 558 nm are focused on the

sample through the probe, generating two temporally separated PA signals. The energy applied to the mouse ear is about 50 nJ per pulse. An optical/acoustic beam combiner in the PA probe reflects the optical beam and transmits the ultrasonic beam. A 50-MHz piezoelectric transducer (V214-BC-RM, Olympus-NDT) detects the ultrasonic waves. We align the optical excitation beam with the acoustic detection beam coaxially and confocally to optimize the sensitivity. Raster scanning the PA probe allows for acquiring volumetric images. The step size is 2.5 µm, the pulse repetition rate is 4 kHz and it takes ~16 minutes to acquire a PA image of 2.5x2.5 mm^2 (2000 x2000 pixels). The imaging resolution is 5 µm in the transverse plane and 40 µm along the acoustic axial direction.

In experiment, 6-week ICR female mice were anesthetized with isoflurane, and the mouse ear was mounted on a glass platform with double-sided tape, as shown in Figure 4-1b. All procedures involving animal experiments were approved by the animal ethical committee of the City University of Hong Kong. Before cupping therapy, we first acquired a PA image as a baseline. Then, a facial cup was applied to the mouse ear for 5 minutes. The facial cup device is transparent cup made of silicon, as Figure 4-1c shown. It is easy to operate, the cup exhausts the air inside by squeezing. The outer and inner diameters of the facial cup opening are 1.5 cm and 0.7 cm, respectively, and the cup length is 5 cm. As a result, the region of the cupping are is around 1.54 cm^2 in the experiment. The pressure exerted on the mouse ear was about -20 kPa. After the cupping process, we acquired several PA images with a time interval of two hours (including the pre-processing time and the imaging time; the actual resting time for the mouse is about 1 hour, which is comparable with the operation time) to monitor the microenvironment changes at the region of interest. Based on these images, blood

vessel density, total hemoglobin concentration, and oxygen saturation are computed and analyzed.
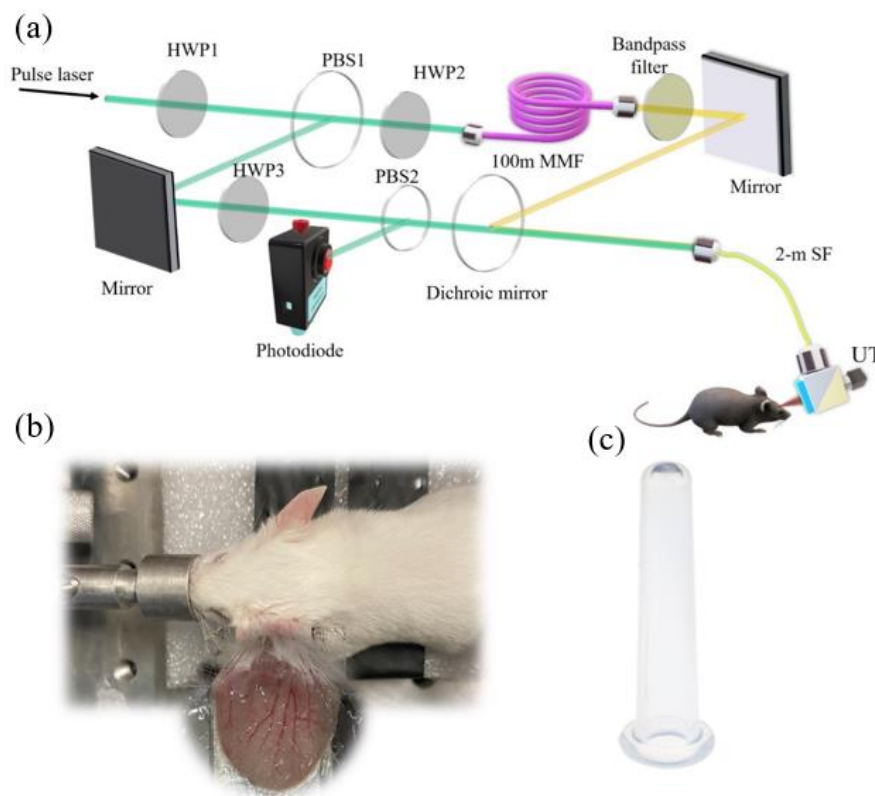
Figure 4-1 (a) Schematic of the photoacoustic-based microenvironment monitoring system. HWP1-3, half-wave plate; MMF, multimode fiber; PBS1-2, polarizing beamsplitter; SF, single-mode fiber; UL, ultrasound lens; UT, ultrasound transducer. (b) Mouse model fixed on the glass platform. (c) Facial cup.

4.3 Results and discussion

Structural images of the same region on the mouse ear pre- and post-cupping are shown in Figure 4-2a and b. Compared with the pre-cupping image, 64% more blood vessels (corresponding to vascular density, the calculation method mentioned in the following part) show up in the image right after the cupping. Moreover, the blood vessels' PA

signal (the averaged PA intensity of the whole figure) increases ~37% after cupping. Figure 4-2c and d are the close-up of white dashed boxes in a and b, respectively. Thus, blood in vessels contributes to the majority of the PA signals in this scenario, and more small blood vessels lead to stronger PA intensities after the cupping. Thus, due to the cupping, more capillaries are congested under the negative pressure and more blood flow into the optical focus, the field of view of the PA imaging system. PA intensities from other small and large blood vessels pre- and post-cupping have not expressed many differences, indicating that this phenomenon is caused by the cupping effect rather than the optical focus changes. Benefiting from the high resolution, we can even clearly see micro-bleeding in the tissue, as pointed by the arrows. It takes about 16 minutes to acquire an image. Although slow, such an imaging speed has not influenced the results due to the fast B-scan speed, and the obtained figures have a relatively constant background (large blood vessels in a and b show close PA intensities).
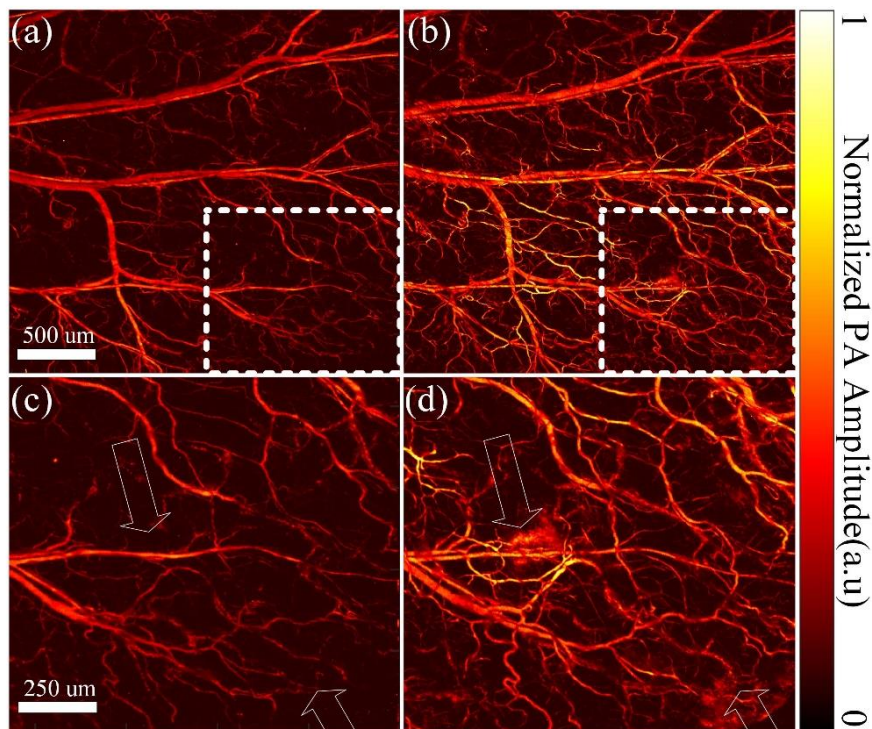
Figure 4-2 OR-PAM structural imaging of the same region of a mouse ear before (a) and right after (b) cupping. (c) Close-up of the dashed box in (a). (d) Close-up of the dashed box in (b).

As a qualitative verification, we acquired a series of photographs before and after cupping, as shown in Figure 4-3a. The camera settings remained unchanged during the whole process. In the photographs, the mouse ear surface as a whole turned red right after the cupping and then recovered to the original status two hours later. Due to the low contrast, photographs cannot provide more detailed information. In contrast, as shown in Figure 4-3b, OR-PAM images of the same mouse ear as circled in Figure 4-3a were acquired at 532 nm. PA signal strength (the averaged PA intensity of the whole figure) significantly increases $\sim 37\%$ right after the cupping but recovers to its original level in two hours. After two hours, there are no significant changes in the PA signal strength. No cupping marks were left after the treatment. Two pairs of blood vessels in Figure 4-3b are chosen to analyze the changes of normalized hemoglobin concentration in cupping through PA signal intensity at 532 nm. Because the absorption coefficients of deoxyhemoglobin and oxyhemoglobin are almost the same at 532 nm, the PA intensity is calibrated to measure the total hemoglobin concentration [113]. As shown in Figure 4-3c, both the veins and arteries exhibit increased hemoglobin concentration significantly right after the cupping. The hemoglobin concentration increased 62% in the veins and 40% in the arteries (forty 10x10-pixel areas in the blood vessel are calculated. $p < 0.05$ from One-way ANOVA, and the sample size is 40). The observed increase is highly consistent with the photographic and morphological PA imaging results in Figure 4-3a and b. After two hours, the hemoglobin concentration in the arteries and veins declines to their original levels. Based on the PA images in Figure 4-

3b, we quantify the blood vessel density. Four times of the standard deviation of the background is used as a threshold to extract the vascular signals. The number of pixels occupied by blood vessels is counted, from which the vascular density is estimated as the ratio between the vessel pixel number and the total pixel number. As shown in Figure 4-3d, the vascular density increases by 64% right after the cupping. After the negative pressure is removed, the vessels and capillaries recover back to their original states, and so does the vascular density. Collectively, the changes in the ear photographs and PAM images, and the calculated total hemoglobin concentration and vascular density consistently suggest that the facial cupping treatment does boost the local blood perfusion. With 5 minutes of $\sim$ 20 kPa pressure, the local microenvironment recovers within two hours.
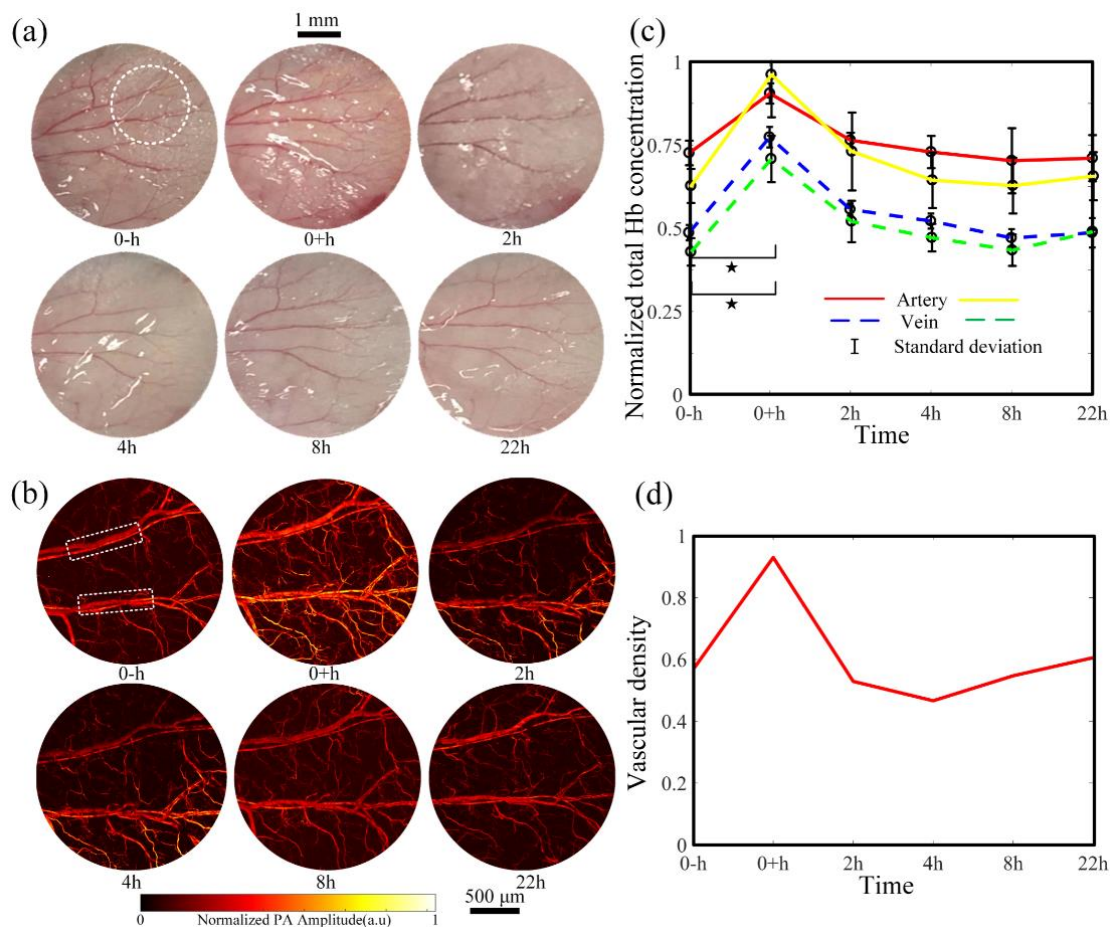
Figure 4-3 Ear vessel photographs (a), OR-PAM images (b), total hemoglobin concentration (c), and vascular density (d) changes before and after the cupping treatment. In (c), changes of artery and vein within the white box in (b) are presented with the red (yellow) line and blue (green) dashed line, respectively. ★, p < 0.05 (tested by one way ANOVA). The error bars in (c) are standard deviations.

We further quantify the oxygen saturation (sO$_2$) in the microenvironment through [61]

$$sO_2 = \frac{\varepsilon_{de}(\lambda_{558})PA(\lambda_{532}) - \varepsilon_{de}(\lambda_{532})PA(\lambda_{558})}{[\varepsilon_{ox}(\lambda_{532}) - \varepsilon_{de}(\lambda_{532})]PA(\lambda_{558}) - [\varepsilon_{ox}(\lambda_{558}) - \varepsilon_{de}(\lambda_{558})]PA(\lambda_{532})} \tag{4-1}$$

where ε_{ox} and ε_{de} are the molar extinction coefficients of oxy- and deoxyhemoglobin at 532 or 558 nm, PA is the photoacoustic signal amplitude at the two wavelengths. In Figure 4-4a, the sO$_2$ images at different time points are computed. The sO$_2$ value in the artery is higher than that in the vein. As shown in Figure 4-4b, the average sO$_2$ values change with time in the regions labelled with the white box. The sO$_2$ values in the veins are from 0.5 to 0.7, and above 0.95 in the arteries. Right after the cupping, the sO$_2$ values in veins and arteries reduced by 17% and 3% (forty 10x10-pixel areas in the blood vessel were chosen for calculation; $p < 0.05$ from One-way ANOVA, and the sample size is 40), respectively. The decrease of sO$_2$ values in blood vessels indicates that more oxygen is consumed in the cupping site or has been transported to the surrounding tissues, promoting the metabolism at the cupping site. During the recovering process, the sO$_2$ values in both veins and arteries return to their original levels. The results are consistent with Figure 4-3 and other reports [105-107].
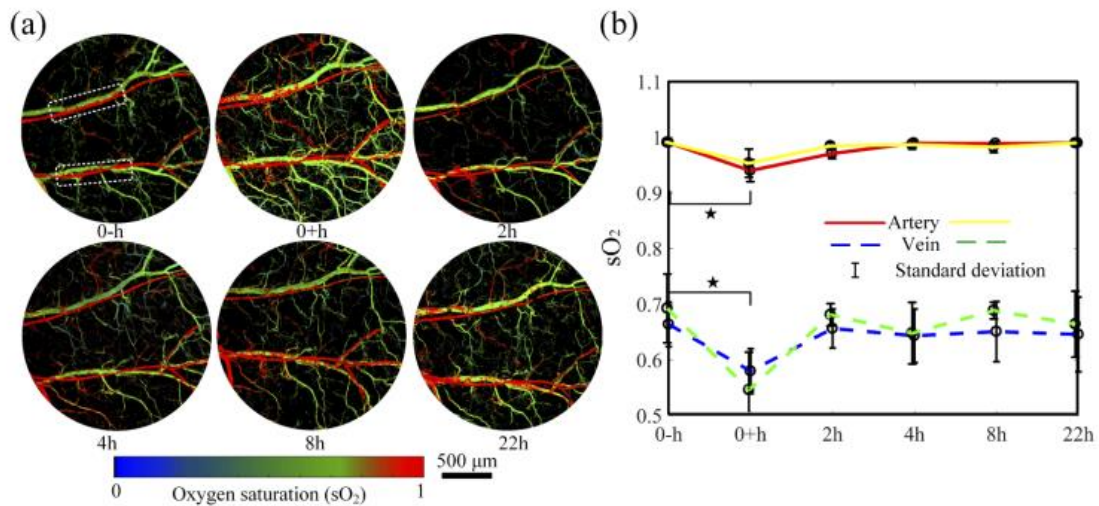
Figure 4-4 Dynamic changes in oxygen saturation before and after cupping. (a) sO₂ map of the mouse ear within the cupping process. (b) Averaged sO₂ changes of the artery (red/yellow line) and the vein (blue/green dashed line) for regions labelled with the rectangle in (a). ⋆, p < 0.05 (tested by One-way ANOVA). The error bars in (b) are standard deviations.

4.4 Conclusion

To better understand the mechanism and quantify the effectiveness of cupping therapy, we introduce OR-PAM to investigate microenvironment changes before and after cupping practice. Considering the imaging depth of OR-PAM is limited within 1 mm, living mouse ear is chosen as the cupping site in this study for its appropriate thickness of around several hundred micrometers. 100 μm). Although not perfect, such a model, as shown in this study, is sufficient to support OR-PAM to monitor and quantify the microenvironment changes associated with cupping therapy. As seen, right after the cupping, superficial capillaries have 37% stronger PA intensity compared with the pre-treatment ones. Some capillaries may bleed under the negative pressure. The total hemoglobin concentration in both veins and arteries is elevated significantly right after

50

the cupping treatment, suggesting that cupping enhances blood circulation. In addition, more oxygen is consumed at the cupping site or stimulated to be transported to capillaries and the adjacent tissues out of the field of view, promoting the metabolism at the cupping site. In two hours after the cupping, the parameters go back to their original level in pre-cupping. This result shows that facial cupping (~20 kPa in 5 minutes) produces a temporary effect and does not cause long-time marks in the skin. In cupping with higher pressure and longer time, marks may stay up to weeks, indicating a more sustainable treatment effect, which, however, waits for further confirmation. The results are well consistent with other reported findings [105-107]. This pilot study is the first step to interpret cupping from a microscopic imaging perspective. We show that the use of OR-PAM can monitor and quantify the cupping effect with high spatial resolution, which can be further used to optimize the pressure and time duration of the cupping treatment. Future explorations will move onto human patients, and acoustic resolution photoacoustic imaging will be used to visualize deeper (mm~cm) microenvironmental changes due to cupping.

5 MICROFLUIDIC PHOTOACOUSTIC VISCOMETRY BASED ON GRUENEISEN-RELAXATION EFFECT

This chapter is reproduced with some adaptations from the manuscript "Yingying Zhou, Chao Liu, Xiazi Huang, Xiang Qian, Lidai Wang, and Puxiang Lai, "Photoacoustic prediction of physiological conditions based on viscosity changes with microlittle consumption", To be submitted". The contributions of authors are as follows: P. Lai, L. Wang and Y. Zhou conceived the idea. Y. Zhou, C. Liu, and X. Huang designed the system. Y. Zhou ran the experiments. Y. Zhou, X. Huang, X. Qian, L. Wang and P. Lai prepared the manuscript. All authors were participated in manuscript preparation.

This chapter is the third application based on the revision of fiber-based ultrafast OR-PAM system developed in Chapter 2. Viscosity measurement is important in many areas of biomedicine and industry. Traditional viscometers are usually time-consuming and require huge sample volumes. Microfluidics overcomes the challenge of large sample consumption but takes a long time to measure it. Moreover, the microfluidic device needs to design a special supporting microstructure to measure the viscosity, which may be complex and costly. Here, we propose dual-pulse photoacoustic

viscometry to measure the liquid viscosity in generic microfluidic devices. The new viscometer method embraces fast detection speed, low fluid consumption, and high detection sensitivity, offering a new tool for efficient viscosity measurement in a broad range of microfluidic devices.

5.1 Introduction

Viscosity, an important thermophysical property, plays a key role in material distinction and liquid performance in medical and industrial fields [114, 115]. Viscosity measurement is crucial in a wide range of applications. For example, blood viscosity is an important clinical parameter due to its close tie with cardiovascular diseases [114, 116, 117]. To determine the viscosity, various methods have been developed. Conventional viscometer usually takes a long time and needs a large volume of fluid for accurate measurement. This method has not ideal when samples are precious or scarce [118-120]. To reduce the sample consumption and increase efficiency, microfluidic methods have been developed for viscosity measurement in recent years. For example, a co-axial microfluidic device is designed to measure the viscosity of Newtonian fluids by Lan *et al.* [121], which allows for a stable liquid/liquid annular co-laminar flow measurement based on Navier-Stokes equations. Kim *et al.* proposed to deliver the reference fluids and the target sample into two inlets of a Y-shaped microfluidic device separately, so that one can measure the sample viscosity by measuring the interfacial width, which is caused in the downstream of this Y-shaped device [122]. Kang *et al.* demonstrated a high-precision microfluidic viscometer on a microfluidic channel array which consists one hundred indicating channels [123]. These methods have significantly reduced the sample consumption, but need to design the measuring devices in advance, which is usually complex, costly, and time-

consuming. Moreover, the compatibility of viscosity measurement relies heavily on the interaction between the supporting microstructure of the device and the tested sample. That is, for different types of samples, one may need to design specific supporting microstructures, which further tightens the requirements and increases the design and operation complexity and cost [124]. Therefore, to broaden the application of microfluidic viscometer to more labs, there is an urgent need for a high-speed, low dose consuming, and precise viscosity measurement method that can be used in a broad range of generic microfluidic devices.

PA tomography is one kind of hybrid modality that uses light for signal excitation and ultrasound for signal detection. PA imaging has been developed for various applications [49, 71, 82, 125-130] including liquid viscosity measurement. For example, in 2010 Lou *et al.* utilized the frequency spectrum of measured photoacoustic signals to distinguish different liquids [131]. Built upon that mechanism, Zhao *et al.* realized the detection of blood viscosity *in vivo* by analyzing the frequency spectrum of blood photoacoustic signals [132]. However, the accuracy of viscosity measurement is limited by the ultrasonic bandwidth and noise. Moreover, photoacoustic detection of viscosity has not been developed for microfluidic devices.

Here, we propose to measure liquid viscosity in a standard microfluidic channel based on the Grueneisen relaxation effect [88]. In a microfluidic tube, flow speed of the liquid has an inversely proportional relation to the liquid viscosity. After calibration, we can determine the viscosity via measuring the flow speed. A single-shot photoacoustic flowmetric method that we previously developed is used here to measure the flow speed in microchannel [44]. The Grueneisen parameter is a temperature-dependent property.

In the dual-pulse excitation approach, because of the lingering temperature effect in first laser excitation, the local Grueneisen parameter changes during second laser pulse excitation. The flow speed can alter the local lingering temperature and the Grueneisen parameter. Consequently, the second PA magnitude is affected by the flow speed. We establish a model between the dual-pulse PA signals and the viscosity in the microfluidic channel. After calibration, different viscous liquids are successfully tested. The results are well consistent with the true values.

5.2 Method

5.2.1 System Setup

As shown in Figure 5-1a, the dual-pulse photoacoustic viscosity measurement platform is adapted from our previous dual-pulse photoacoustic flowmetry setup [44]. The same 532-nm laser as mentioned in Chapter 2 serves as excitation laser pulse, and a polarizing beam splitter (PBS1) divides the laser pulse into two paths. Before the PBS1, a half-wave plate is added to precisely adjust the two daughter laser beams' energy ratio. One of the laser beams is coupled into a 30-m SMF, which delays the laser pulse by ~146 ns from the other one, which is transmits in free space, as shown in Figure 5-1f. To increase the fiber coupling efficiency, another HWP2 is placed before the 30-m SMF to adjust the polarization state. This 30-m delay fiber only functions as a delay path; the spectrum of the two beams is shown in Figure 5-1e, confirming the sole wavelength of 532 nm of the two beams. The pulse energy of each laser beam is around 90 nanojoules. The two beams are recombined with another PBS2 and coupled into a 2-m SMF, which is connected to the scanning probe. The combined coupling efficiency of the two fibers is above 50%. Two achromatic doublets focus the light transmitted from the 2-m SMF

and the light then excites the region of interest in the target. The generated photoacoustic signal is received by the piezoelectric transducer. The excitation light and acoustic detection are confocally and coaxially aligned to optimize the sensitivity. More specific parameters of the probe can be found in our previous publications [132, 133].

Driven by the pressure (The pressure is constant and can be controlled by the air compressor) produced from an air compressor (JUBA, Yuteng Hardware and Electrical Tech, China), different viscous liquids flow in a transparent micro-tube (inner diameter is 0.25-mm, TYGON S-54-HL, Norton Performance Plastics, China). Different viscous liquids are obtained by mixing and stirring ink solution with different contents of surfactants solutions (20% Tween®20 aqueous solutions, Scientific Phygene, China). Tween®20 is a kind of polymer, which is widely used in the microfluidic field as an oil-in-water (O/W) emulsifier. The blood samples adopt adult bovine whole blood (Hongquan Biotechnology, Guangdong, China). Different viscous blood samples to emulate anemia and polycythemia conditions are obtained by mixing different concentration of plasma and hemocytes as mentioned in previous publication [11]. In brief, the plasma and hemocytes are separated by the centrifuge at 1400 rpm for 3 minutes from the normal whole blood (~40% haematocrit). The plasma is extracted from the upper half and the blood with ~80% haematocrit is obtained from the remaining half. Then, 75% plasma volume and 25% plasma volume are mixed and stirred with appropriate hemocytes (25% volume and 75% volume) to emulate anemia (~20% haematocrit) and polycythemia (~60% haematocrit) conditions, respectively. The whole bovine blood is used as normal group.
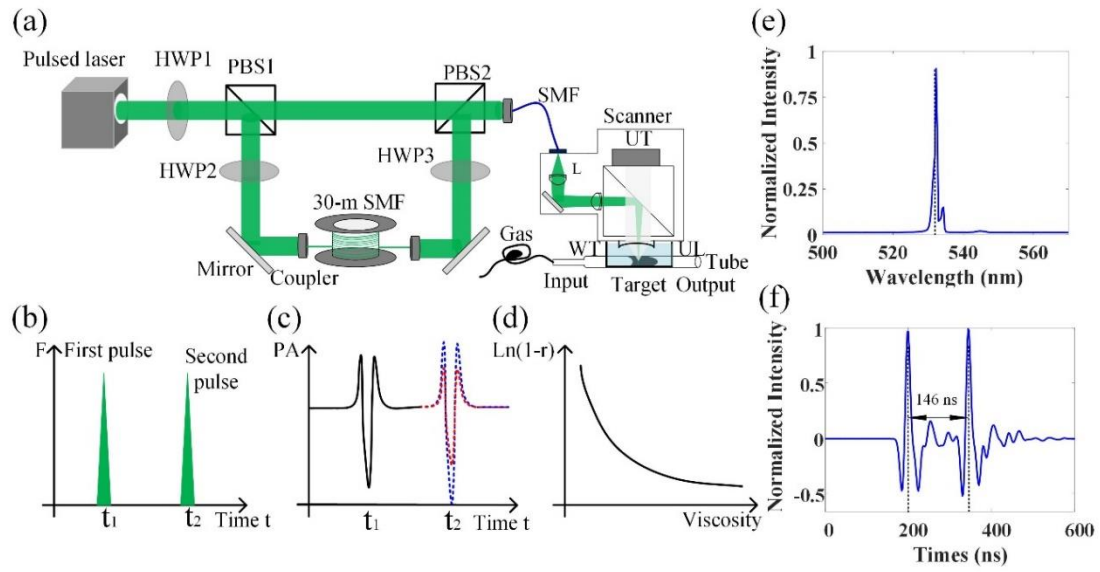
Figure 5-1 (a) Schematic of the dual-wavelength photoacoustic viscosity measurement platform[44]. HWP, half-wave plate; L, lens; PBS, polarizing beam splitter; SMF, single-mode fiber; UL, ultrasound lens; UT, ultrasound transducer; WT, water tank. (b) Two laser pulse with same energy excitations. (c) Generated two photoacoustic signals, the second signal can be larger or smaller than first one, which is decided by the material. (d) The estimated value of $\ln(1 - Ratio)$ versus the viscosity. (e) The spectrum of the excitation beams, showing a sole wavelength of 532 nm. (f) Time delay of 146 ns between the two optical pulses.

5.2.2 Principle

The principle of the dual-pulse photoacoustic viscosity measurement is presented as follows. Based on the Poiseuille's Law equation [134], the flow rate of liquid, Q, in a round tube is equal to

$$Q = \frac{(P_2 - P_1)\pi r^4}{8\xi l} \tag{5-1}$$

The flow rate Q is directly related to flow speed (v), $Q = \pi r^2 v$, where r is the inner diameter of the tube. Transforming Eq. (5-1) and combining the relationship between flow rate and speed, the liquid viscosity ξ can be expressed as

$$\xi = \frac{(P_2 - P_1)\pi r^4}{8lQ} = \frac{\Delta p r^2}{8lv} \tag{5-2}$$

where P_2 and P_1 are the pressures at the input and output points of the tube, respectively, and l is the length of the tube. The pressure difference (Δp) can be controlled by the air compressor and the parameters (r and l) of the tube are known. Thus, the liquid viscosity can be calculated when the flow speed of the liquid (v) is obtained.

Dual-pulse photoacoustic microscopy has been used to calculate the flow speed [44]. In a linear range, the sequentially induced two photoacoustic signals (PA_2 and PA_1) can be approximated as [8, 135]

$$PA_1 = k\Gamma_0 \eta F_1 \mu_{a1} \tag{5-3}$$

$$PA_2 = k(\Gamma_0 + \Delta\Gamma)\eta F_2 \mu_{a2} \tag{5-4}$$

where k is system detection parameter, Γ_0 is the Grueneisen parameter of the baseline temperature, $\Delta\Gamma$ is the changed Grueneisen parameter due to first pulse heating effect, η is the coefficient for light-to-heat conversion, F_1 and F_2 are the *in situ* optical fluences, and μ_{a1} and μ_{a2} are optical absorption coefficients for the two excitation laser pulses (μ_{a1} and μ_{a2} are the same as the same wavelength was used in our experiment). The changed Grueneisen parameter $\Delta\Gamma$ is affected by the local temperature changing, which can be modelled as [71, 88, 136-138],

$$\Delta\Gamma = aF_1\mu_{a1}e^{-(\tau_a + bv)\delta t} \tag{5-5}$$

where a, b and τ_a (related to the thermal conduction) are constant coefficients, v is flow speed, and δt is the known time delay between the two pulse excitations. As shown in Figure 5-1b, the optical fluence, F_1, is the same as F_2 in our experiment. Thus, the ratio between the second and the first photoacoustic signals can be written and simplified as

$$\frac{PA_2}{PA_1} = \frac{k(\Gamma_0 + \Delta\Gamma)\eta F_2 \mu_{a2}}{k\Gamma_0 \eta F_1 \mu_{a1}} = 1 + \frac{\Delta\Gamma}{\Gamma_0} = 1 + \frac{aF_1\mu_{a1}e^{-(\tau_a + bv)\delta t}}{\Gamma_0} \tag{5-6}$$

Within the same pulse energy excitation, the generated PA_2 can be larger or smaller than PA_1, which is determined by the absorption material itself, as shown in Figure 5-1c. Taking log_e operation on both sides of the Eq. (5-6), we can get

$$\ln\left(\left|\frac{PA_2}{PA_1} - 1\right|\right) = -ln\frac{|a|F_1\mu_{a1}}{\Gamma_0}(\tau_a + bv)\delta t = mv + n \tag{5-7}$$

where $m = -b\delta t$, and $n = -ln\frac{|a|F_1\mu_{a1}}{\Gamma_0}\delta t\tau_a$, both of which could be obtained through system calibration. Therefore, the flow speed v can be determined through the ratio of dual-pulse PA signals. Then, the liquid viscosity can be calculated according to Eq. (5-2). Combining Eq. (5-7) and Eq. (5-2), the estimated relation between the values of $\ln(1 - Ratio)$ versus the viscosity is shown in Figure 5-1d.

5.3 Results and discussion

A batch of well mixed solutions of different viscosities is shown in Figure 5-2a. To investigate if the regular (single-beam) photoacoustic signal significantly depends on the concentration of surfactant, different solutions were measured and compared under the same conditions. All solutions were injected into the microfluidic tube without flowing and excited by one laser pulse. The pulse energy was ~90 nanojoules, and the pulse repetition rate was 8 kHz. As shown in Figure 5-2b, the single-beam

photoacoustic signal amplitude changes very slightly with the contents of surfactants. The peak-to-peak amplitudes are extracted and shown in Figure 5-2c. As seen, compared with the solution containing 10% surfactants, the single-beam photoacoustic signal amplitude of the 70% solution only reduces by ~2.78%, and the signal amplitudes of the 50%, 30%, and 20% solutions drop by merely about 2.59%, 1.89%, and 0.90%, respectively. The result suggests that the difference of the surfactant concentration induces very limited variation to the optical absorption coefficient changes and hence the single-beam photoacoustic signal strength of different solutions. Moreover, the small divergences, if exist, can be easily compensated based on the measured results.
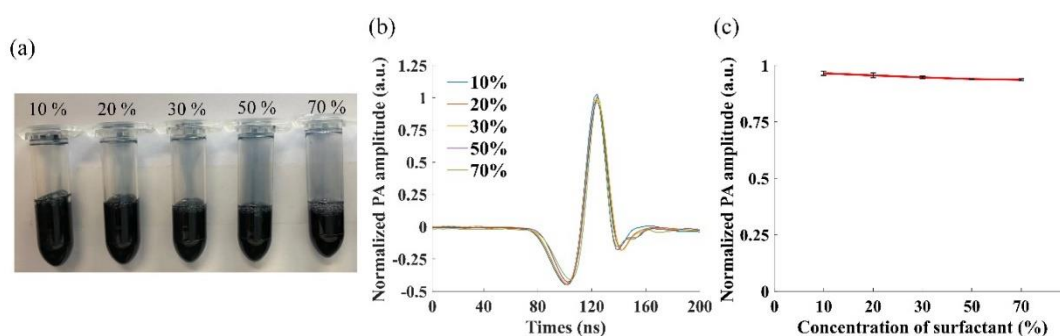
Figure 5-2 (a) Photograph of surfactant-ink solutions of different viscosities (containing 10%, 20%, 30%, 50% and 70% of surfactant, respectively). (b) Normalized photoacoustic signals of different surfactant-ink solutions. (c). Photoacoustic signal (peak to peak) amplitude as a function of surfactant concentration.

After confirming the small absorption fluctuations caused by different concentrations of surfactants, solutions were injected by turn and flow in the microfluidic tube under a constant pressure driven by an air compressor. Measurements were performed with the dual-pulse photoacoustic setting as described above. For each group of solutions,

dual-pulse photoacoustic signals, as illustrated in Figure 5-3a, were obtained. As seen, the two PA signals corresponding to the two pulses can be easily distinguished and separated. The peak-to-peak values of these two photoacoustic signals are extracted, and the ratio between them is defined as 'ratio'. The values of $\ln(1 - Ratio)$ at different surfactant concentrations are plotted, as shown in Figure 5-3b. As seen, the measured logarithm value shows an inverse proportional trend with the solution concentration. This is consistent with the fitted curve derived based on Eqs. (5-7) and (5-2), which follows a relation $\ln(1 - Ratio) = \frac{24.256}{con} - 3.5123$ with a determination coefficient (R^2) of 0.9728, where con is the surfactant concentration. This result, again, confirms the feasibility of the proposed dual-pulse photoacoustic method for viscosity measurement.
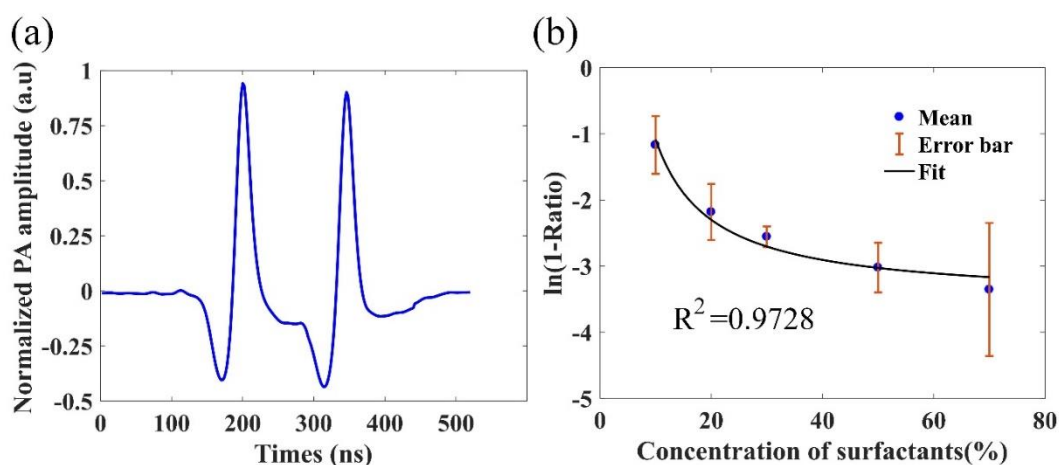
Figure 5-3 (a) A representative dual-pulse photoacoustic signal. (b) The value of $\ln(1 - Ratio)$ versus the surfactant concentration. Error bars are standard deviation and the sample size is 80.

To obtain the system parameters, m and n, in Eq. (5-7), a pure ink solution (no surfactant) was used to calibrate the relationship between the 'Ratio' and the preset

flow speed. The air compressor in this calibration was removed temporally, and a syringe pump is used to set the liquid flow speed within a range from 1 to 25 mm/s. The relationship between values of $\ln(1-Ratio)$ and flow speeds is shown in Figure 5-4a. The $\ln(1-Ratio)$ and the flow speed are approximately linearly correlated with each other. The determination coefficient (R^2) is 0.9662, which indicates a strong dependence of the dual-pulse signal ratio on the flow speed. The fitted curve between these two parameters can be expressed by $\ln(1-Ratio)=0.0505v-3.6795$, where 0.0505 and -3.6795 correspond to m and n in Eq. (5-7), respectively. From this equation, the flow speed can be firstly computed through $v=\frac{\ln(1-ratio)+3.6795}{0.0505}$ as the two signals' ratio can be determined directly from the experiment. Then back to the Poiseuille's Law equation, the viscosity information can be computed from Eq. (5-2), that is $\xi=\frac{0.0505\Delta pr^2}{8l[\ln(1-Ratio)+3.6795]}$.
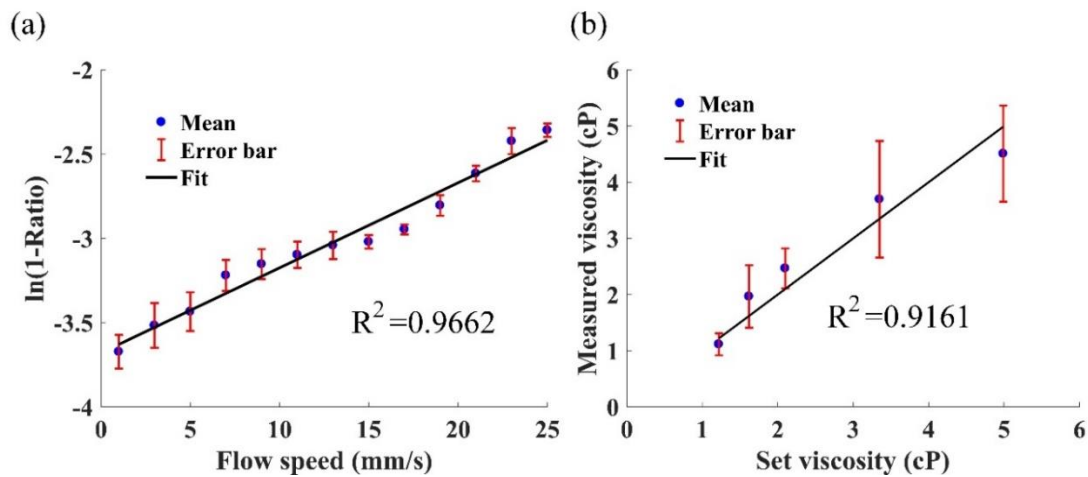
Figure 5-4 (a) Ratio between the two PA amplitudes versus the preset flow speed. (b) Measured viscosity versus true solution viscosity. Error bars are standard deviation.

Because the pressure difference (Δp) and tube parameters (r and l) are constant, we can simplify the relationship between the liquid viscosity and the signal amplitude ratio to $\xi = \frac{c}{\ln(1-Ratio)+3.6795}$, where the $c = \frac{0.0505\Delta p r^2}{8l}$ is a constant if one type of viscous solution is applied to calibrate the system.

In the experiment, 90% surfactant-containing solution (with a viscosity coefficient of 7.10 cP) was first used as the calibration sample. The solution flowed in the microfluidic tube under the pressure produced from the air compressor. The sample was excited by two sequential beams, and the ratio of the two photoacoustic signals was computed. Then the value of c was calculated, which was 2.7169 for the used setup. Then, samples of various viscosities (10%, 20%, 30%, 50%, and 70% of surfactant-containing solutions; <50 µL usage) were tested under the same pressure. Meanwhile, the viscosities of different solutions were computed to be 1.22, 1.62, 2.10, 3.35, and 4.99 cP, respectively. The measurement process can be completed in one dual-pulse excitation (0.000125 seconds) with 8 kHz pulse repetition rate. To increase the accuracy, one sample was excited by 10,000 times, and thus the testing process takes about 1.25 seconds. The measured viscosities are compared with the actual solution viscosities, as shown in Figure 5-4b. As seen, two sets of data are linearly correlated with each other, with a determination coefficient (R^2) of 0.9161. This demonstrates well that the proposed Grueneisen-based dual-pulse PA method can precisely measure the liquid viscosity.
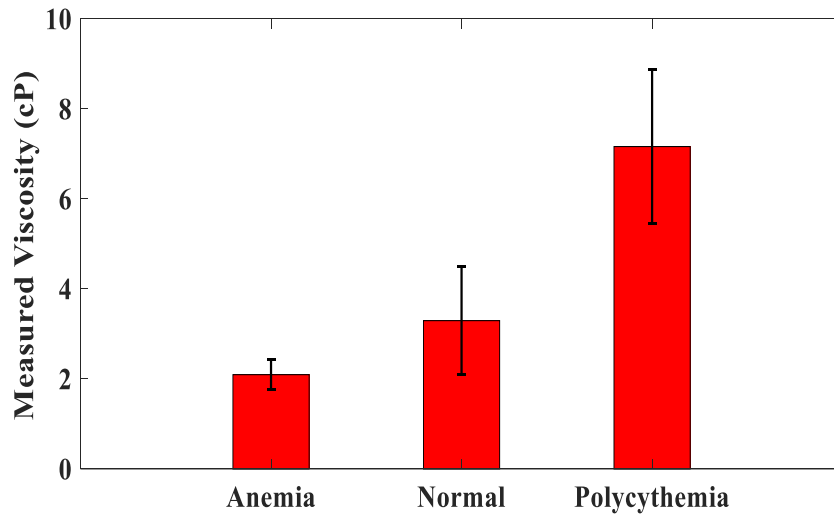
Figure 5-5 Measured blood viscosities for different groups.

Since the blood viscosity has a close tie to many diseases and the haematocrit is closely related to blood viscosity, different viscous bovine blood samples (one drop, around 50 µL) were tested, as shown in Figure 5-5. The measured blood viscosity results show a good linear relationship with the hematocrit values and agree well with the literatures in which blood viscosity for 20% hematocrit (anemia) is of $\sim 2 \times 10^{-3} Pa \cdot s$, for normal human or bovine blood is of $3 - 4 \times 10^{-3} Pa \cdot s$, and for the 60% hematocrit (polycythemia) is of $6 - 8 \times 10^{-3} Pa \cdot s$, respectively. This result reconfirms the precision of the proposed Grueneisen-based dual-pulse PA method. It should be worth mentioning that the blood samples tested here can be reused again as no labels or biochemical processing are involved. The blood in the tube can be collected for retest or other uses, which is meaningful in real applications with precious or scarce samples.

5.4 Conclusion

In this study, a new strategy is proposed to measure the viscosity of liquids in a microfluidic tube via featuring the Grueneisen relaxation effect in a dual-pulse

photoacoustic flowmetric system. An inverse model has been developed to quantify the liquid viscosity from the flow speed. It has been experimentally demonstrated that after system calibration, the measured liquid viscosities agree quite well with the actual values. Note that this dual-pulse photoacoustic viscosity measurement method uses only regular microfluidic tubes but no specifically designed supporting structures, greatly reducing the complexity of system design and operation for liquid viscosity measurement. Moreover, the measurement process in our method is up to 1.25 seconds, which can be considerably shortened if necessary. The platform only requires a tiny dosage of the sample (one drop, < 50 µL), which is essential for precious and scarce samples. To the farther future, this may can be integrated in a small handheld pocket system to test the blood viscosity like portable blood glucose meter, which may help to achieve daily viscosity monitoring for specific patients. Lastly but not least, this Grueneisen-based dual-pulse photoacoustic viscosity measurement method yields increased detection sensitivity compared with the spectrum-based photoacoustic measurement method [131]. In conclusion, the proposed dual-pulse photoacoustic method considerably increases the detection efficiency as well as accuracy, and it may enable microfluidic viscosity detection free from supporting microstructures.

6 ULTRAFAST DEEP PENETRATING OPTICAL RESOLUTION PHOTOACOUSTIC MICROSCOPY THROUGH LEARNING-BASED TRANSFORMATION

This chapter is reproduced with some adaptations from the manuscript "Shengfu Cheng, Yingying Zhou, Huanhao Li, Lidai Wang, and Puxiang Lai, Ultrafast deep penetration optical resolution photoacoustic microscopy through learning-based transformation" (to be submitted). The contributions of authors are as follows: P. Lai, Y. Zhou, and H. Li conceived the idea. Y. Zhou and L. Wang designed the system. Y. Zhou ran the experiments. S. Cheng processed the data. All authors were participated in the results' analysis and manuscript revision.

In the previous chapters, ultrafast OR-PAM is achieved via the short-delay fiber system, and some biomedical applications are investigated based on this system or its modifications. The light highly scattering in tissue limits the imaging depths in couple hundred micrometers. Such a depth can provide scant information of biological tissues

in application. Thus, there is need to advance the penetration depth of the ultrafast OR-PAM. Currently, there are already some reported methods to enhance PA imaging deeper into tissue, such as with wavefront shaping guidance [139] or tissue clearing agents [140]. Wavefront shaping can manipulate multiple scattered light to refocus inside a complex medium, which yet is limited by the focusing speed to determine the optimum phase compensation. Smearing tissue clearing agents on the target surface can reduce the refractive index mismatch and hence the scattering of tissue surface, allowing for deeper propagation of focused light. But this method cannot increase the imaging speed and the chemical agents always have a limited action time.

In this chapter, a new deep learning enhanced deeper penetrating ultrafast OR-PAM is proposed. Note that the optical-resolution performance is achieved based on not conventional OR- but AR-PAM, which is realized through improving AR images' resolution to optical resolution standard based on a generative adversarial network (GAN) while keeping the fast scanning speed as regular AR-PAM. Conventional AR-PAM can image deeper than OR-PAM but with lower image resolution due to the difference of optical excitation beam spot size. Furthermore, AR-PAM leads to a faster raster scanning speed which matches with scanning step size. How to achieve deep imaging depth while maintaining high resolution and fast speed is an essential problem in photoacoustic imaging. In the past few years, deep learning has been widely used in improving the image quality in optical imaging field and photoacoustic imaging as well. In this chapter, we propose to realize ultrafast deep tissue imaging with imaging resolution transform from AR-PAM to OR-PAM via deep learning method. Based on AR-PAM and OR-PAM data on *live* mice ear, a GAN is trained (AR data as the input and OR data as the output). The feasibility and efficiency of the network are validated

with the experimental data set that are not used in network training by comparing the correlation and similarity of the network output with the OR images. The generalization capability of the network is also studied by extending to mouse brain images, although the network is trained based on mouse ear data sets. Therefore, with the proposed deep learning method, we are able to realize deep-penetrating ultrafast OR-PAM that has been desired for long.

6.1 Introduction

Photoacoustic imaging has been widely studied in recent years as a hybrid imaging technique [40, 141-144]. PAM is an important division of photoacoustic imaging that can achieve higher resolution than PACT, and it is usually applied for micro-scale imaging [145-147]. PAM can further be categorized into AR-PAM and OR-PAM depends on mode of excitation optical illumination [4]. Comparisons between them are listed in Table 6-1 below. For example, the imaging resolution in AR-PAM is decided by the acoustic transducer as the excitation beam loosely illuminating the sample; the illumination in OR-PAM is tightly focused to a diffraction-limited spot , which is 10 times or more smaller in diameter than the acoustic focus [4]. Thus, one of the major differences between OR-PAM and AR-PAM is lateral resolution. Typically, OR-PAM could realize a lateral resolution down to 0.2~10 µm, while for AR-PAM it is around 15~50 µm. As for the axial resolution, both of them are decided by the axial profile of the acoustic focus, being about 30 µm [4]. Note that, however, there is a trade-off between penetration depth and lateral resolution, and usually higher resolution means shallower imaging depth. Specifically, OR-PAM is typically limited in the optical diffusion limit (<1 mm), while AR-PAM can go beyond the optical diffusion limit (1~10 mm) [29, 148-150].

Table 6-1 Comparisons between OR-PAM and AR-PAM

	OR-PAM	AR-PAM
Lateral resolution	Optical (0.2~10 µm)	Acoustic (15~50 µm)
Axial resolution	Acoustic (15~30 µm)	Acoustic (15~30 µm)
Imaging depth in biological tissue	Ballistic and quasi-ballistic regimes (<1 mm)	Diffusive regime (1-10mm)
Image formation mode	Raster scanning	Raster scanning

Both OR-PAM and AR-PAM are based on raster scanning to form images. The step size of the raster scanning should match the imaging resolution to avoid over or down sampling. Thus, OR-PAM and AR-PAM typically have different raster scanning step sizes, and it takes different time to obtain a figure of same field of view. For example, if the OR-PAM and AR-PAM have a lateral resolution with 5 µm and 50 µm, respectively, the imaging speed of AR-PAM can be 100 times faster than that of OR-PAM for two-dimensional raster scanning of a same field of view. Imagine that if advantages of AR- and OR-PAM can be combined, it can significantly extend applications of PAM in many scenarios that require high resolution, deep penetration depth, and fast scanning speed to reduce the physiological artefacts.

Deep learning has been paid special attention to realize super resolution in optical imaging in recent years. For example, in 2015, Dong *et al.* [151] proposed to upscale an input image by bicubic interpolation and trained a mean squared error (MSE)-based three-layer end-to-end super-resolution convolutional neural network (SRCNN) to achieve super-resolution. In 2017, Christian *et al.* [152] proposed a super-resolution generative adversarial network (SRGAN) driven by perceptual loss to achieve photo-realistic super-resolution in single image. Then an enhanced version of that, enhanced super-resolution generative adversarial network (ESRGAN), was proposed in 2018 to improve the Generator architecture and adopted relativistic discriminator and network interpolation [153]. In 2017, Ozcan *et al.* [154] demonstrated a microscopy based on deep learning which can transform a sample image acquired with a low-resolution wide-field microscopy into a high-resolution image. In 2019, the same group presented GAN-enabled fluorescence microscopy' cross-modality super-resolution [155].

From these examples, it is hypothesized that deep learning can also be used as a considerable tool to improve the resolution in PAI. In this chapter, we propose to achieve ultrafast deep "OR-PAM" by using deep learning as a tool for resolution transformation from AR-PAM to OR-PAM while keeping AR-PAM's penetration depth and scanning speed. Ten groups of AR-PAM and OR-PAM images (from living mice ears) with the same field of view are collected, which went through data expansion and then were used to train the neural network. After network training, AR-PAM data unused in network training were as input. The output of the network was compared with the ground truth (collected OR-PAM data) to test the feasibility and efficiency of the network. Furtherly, mice brain AR-PAM images were examined. Although the network was trained with mice ear data set, the output from the network achieved significantly

improved resolution close to that of OR-PAM. The result shows the generalization capability of the network, and more importantly the network allows for deep-penetrating OR-PAM imaging of intact mouse brain, which used to be physically impossible. Lastly but not the least, the spirit of the neural network can be extended for other aspects of photoacoustic imaging, such as increasing the contrast, revealing the microenvironment, and identifying the regions of interests in deep biological tissue with OR-PAM.

6.2 Methods

6.2.1 System characterization and data collection

A 532 nm laser source provides the PA excitation beam, which is delivered into the PAM probe as shown in Figure 2-1 through a 2-m SMF to pump OR-PAM, or through a 1-m multi-mode fiber (M105L01-50-1, Thorlabs Inc) to pump AR-PAM. These two imaging modalities can be swapped by shifting the two fibers: when the probe is connected to the single-mode fiber, light is tightly focused and the detection sensitivity is optimized through coaxial and confocal alignment between the optical and acoustic focuses, resulting in OR-PAM performance; when the probe is connected to the multi-mode fiber, light output from the fiber is diffusive and the signal resolution is decided by the piezoelectric transducer (V214-BC-RM, Olympus-NDT), resulting in AR-PAM performance. The step size is 1.25 µm for both AR and OR-PAM in collecting training data and the step size for AR-PAM is changed to 5 µm for collecting the figures for validating the trained network performance. The imaging resolution is calibrated as shown in Figure 6-1, where blue hollow circles are the photoacoustic signals obtained from a sharp edge of blade. The red and blue lines are the derived line spread function

(LSF) and edge spread function (ESF) of the measured data, respectively, using the method introduced in Ref. [156]. As seen, the lateral resolution of the OR- and AR-PAM modules are 3.5 and 48.1 μm, respectively in our system.
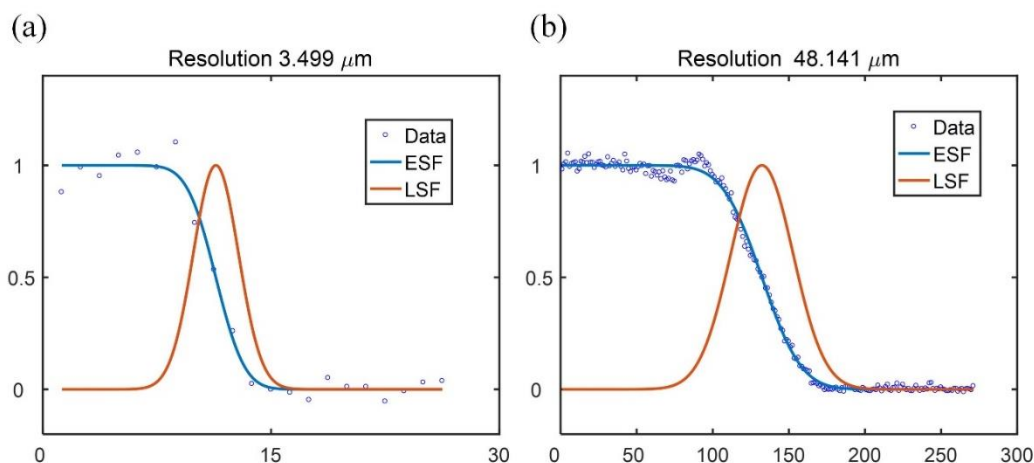
Figure 6-1 Calibration of the lateral resolutions of the OR-PAM system (a) and the AR-PAM system (b), respectively, by scanning across the sharp edge.

Isoflurane was used to anesthetize several 6-week-old mice (ICR model), and a glass platform was applied to mount the mouse ears. All procedures involving animal experiments have been approved by the Animal Ethics Committee of City University of Hong Kong. A series of 5×5 mm^2 regions of mice ears were collected by the OR-PAM to as the ground truth, which was closely followed by AR-PAM. Images from the same region was grouped as one data set for neural network training.

For mice brains, the skin hairs were removed firstly with hair removal cream. Then the skin was disinfected and cut with surgical scissors; the skull was intact. The exposed brains were scanned with AR-PAM in focus with a FOV of 5×5 mm^2.

6.2.2 Pre-processing of image pairs

To ensure the AR and OR images scanned separately were spatially well matched, pre-processing of image pairs is necessary. For example, in experiment not only blood vessel signals but also some random noise points were obtained as isolated bright spots (due to over exposure) or stained noises as circled in Figure 6-2. These cause mismatch between AR and OR images. Thus, the first step of pre-processing was to denoise the collected data, for which two conditions were applied. One assumes that an isolated bright pixel is usually surrounded with pixels of inferior value, hence the isolated pixel can be removed by smoothing or low pass filtering. The other is for background noises, when not all neighbouring pixel values of bright stain noises are similar to vascular values, it should be set as 0. Through these two methods, the noise pixels could be reasonably suppressed.
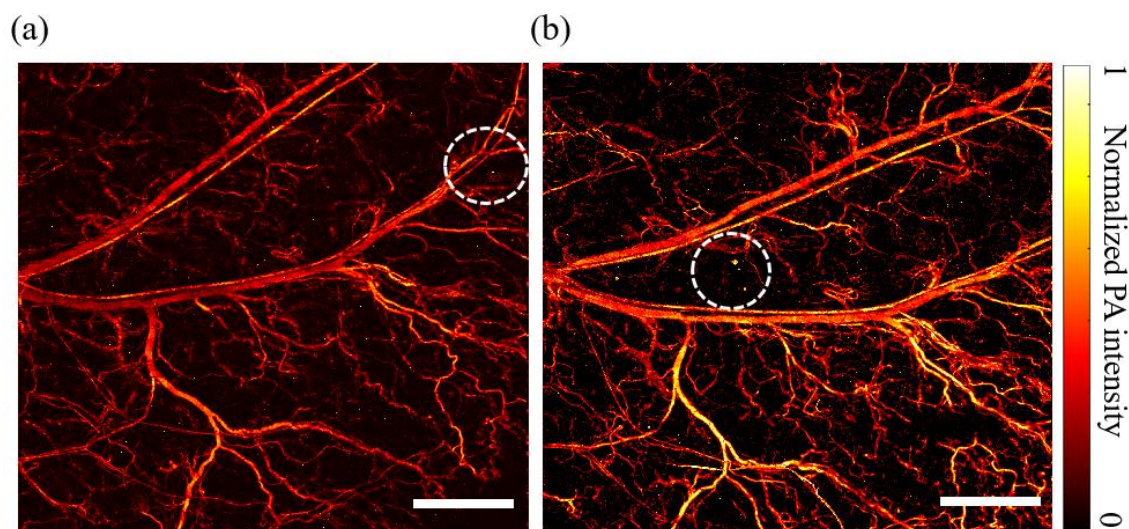
Figure 6-2 OR-PAM images with isolated bright spots (a) and stain noises (b).

(Scale bar: 1 mm).

Apart from the abovementioned issues, there is another mismatch between the AR-OR pairs, the spatial misalignments caused by separate motor scanning. To solve this problem, registration should be applied. The obtained OR and AR images were divided into 36 small patches. Each patch in OR images worked as a template to find the patch with highest correlation in AR images, based on which an image pair was extracted, forming a group for network training.

In addition, data augmentation was applied to enlarge the dataset for the AR-OR patch pairs. The data augmentation included geometry transformation and grayscale transformation. Furthermore, the geometry transformation contained flipping (null, vertical, horizontal, and diagonal), rotation (rotation angle of 0°, 90°, and 270°), and elastic deformation. Finally, 34,270 pairs of AR-OR patches of mice ear images based on 14 mice were obtained, in which 10 groups were used for training and 4 groups for testing. Notably, the training set and testing set share no overlap.

6.2.3 Neural network training

Generative adversarial network (GAN) has shown its potentials for image super-resolution [157, 158], and we choose it as the network for image transformation from AR to OR performances. The adopted network uses adversarial training in the min-max game as briefly shown in Figure 6-3. The generator (G) produces super-resolution (SR) images from the AR data and tries to fool the discriminator (D). And then, both SR and OR data are fed into the D, which is to distinguish which one is the OR image. During the training process, the abilities of D and G are significantly enhanced by learning from the dataset. Finally, the competition between G and D suggests that the quality of SR images from G approach to that of the ground truth OR. Data pre-processing and

network training was completed by my teammate, Mr. Shengfu CHENG. As these two parts are not the focus of this thesis, they are not described in detail herein.
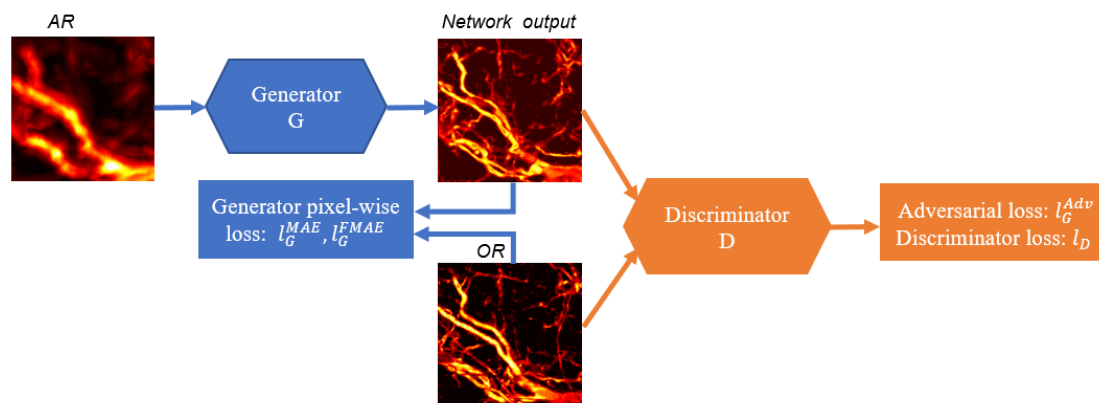
Figure 6-3 Illustration of the adversarial training in this study

6.3 Results and discussion

6.3.1 AR-PAM and OR-PAM mouse ear figure pairs

One typical pair of collected AR-PAM and OR-PAM images of mouse ear are shown in Figure 6-4. The overall quality of the AR image is apparently incomparable with that of the OR image. Small features are hard to be resolved clearly and it is not easy to distinguish arteries and veins in the AR image via the blood vessel widths. For example, as circled by the white dotted line in Figure 6-4a, two blood vessels merge to one, which probably induces inaccurate information. Moreover, it is difficult to differentiate the depth information between the two blood vessels when they intersect with each other, as circled by the blue dots in Figure 6-4a. The small blood vessels look even fuzzy due to low image resolution. The representations behave quite differently in the OR-PAM image (Figure 6-4b). We can easily distinguish the types of blood vessels; the arteries are thinner than the veins and accompany with the veins. The depth information of

intersecting blood vessels can be differentiated and small blood vessels like capillaries have been seen clearly.
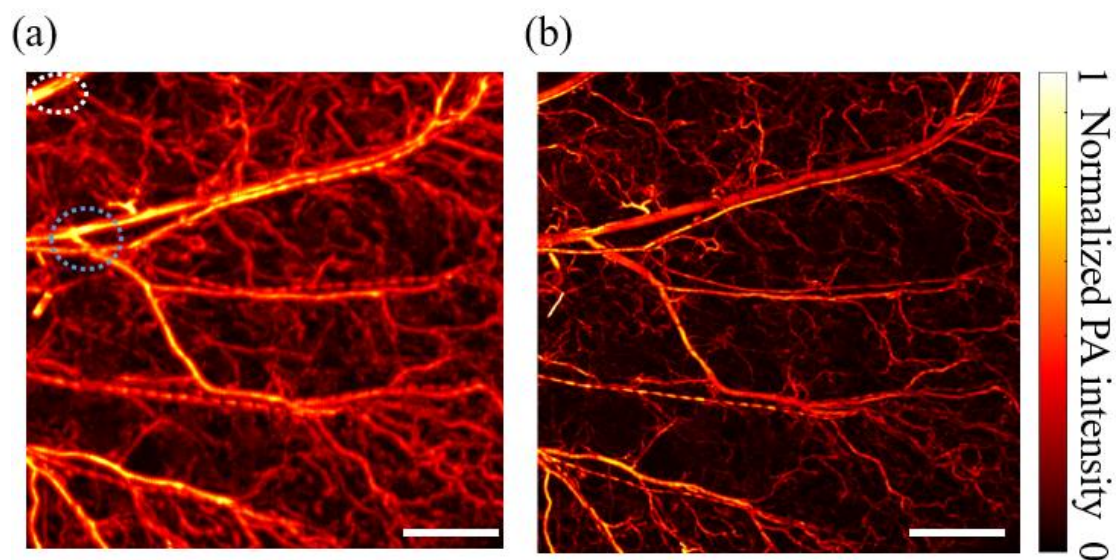
Figure 6-4 (a) A typical AR-PAM image of a mouse ear; (b) The corresponding OR-PAM image of the same mouse ear region. (Scale bar: 1 mm).

6.3.2 Training results of mouse ear

The training data are from mice ears. After the completion of the training process, new collected AR-PAM mice ear images (not included in the training set) were fed into the network, and the outputs were compared with the corresponding OR-PAM images as the ground truth. As shown in Figure 6-5, three columns from left to right are AR-PAM images (Figure 6-5a and d), network outputs (Figure 6-5b and e), and the corresponding OR-PAM images as the ground truth (Figure 6-5c and f), respectively. As expected, the image quality of AR images are not as good as that of OR peers. The boundaries of blood vessels are not clear and the two major blood vessels merge to one at some locations. Moreover, many tiny blood vessels such as capillaries are not resolved clearly in the AR images. After network processing, the blood vessels' boundaries become

76

much sharper and many small blood vessels that are fuzzy in the original AR image are enhanced with higher signal intensities. Visually, the network outputs are very similar to the OR images in terms of contrast and resolution.

To confirm the similarity, in the insets of Figures 6-5(a-c), the three dotted regions in Figures 6-5(a-c) are zoomed in. The signal amplitude profiles along the white line in the boxes are extracted and compared, exhibiting very similar features between the network outputs with the ground truths. It is worth mentioning that the network can differentiate adjacent blood vessels well due to increased resolution. For example, the two major blood vessels shown in (a) are not clearly resolved. It seems that these two vessels have identical thickness. However, according to the network output, these two blood vessels are very different, and they do not belong to one category, which is consistent with the information provided by the OR-PAM image. The white boxes in the bottom right corner of Figure 6-5(d-f) are the zoom-ins of the central boxes of Figure 6-5(d-f). As seen, the signal intensity profile in the AR image shows random peaks. After network processing, two signal peaks are expressed, indicating the existence of two small vessels. This is consistent to the features in the corresponding OR-PAM image, confirming the ability of the network in resolution improvement.

It should be noted that some small vessel features, as circled by the blue and green dotted lines in Figures 6-5(d-f), exist in the OR-PAM image but are not shown in the network output and the AR-PAM image. This is not caused by the processing error of the network; in experiment, these small vessel features were not collected by AR-PAM but only by OR-PAM. It also should be noted that during data collection, some scanning errors are inevitable associated with the two separated raster scanning for OR-PAM and

AR-PAM, respectively. The captioned phenomenon indicates the capability of the network to achieve the image quality improvement of AR figures while maintain fidelity of information without generating fake features.
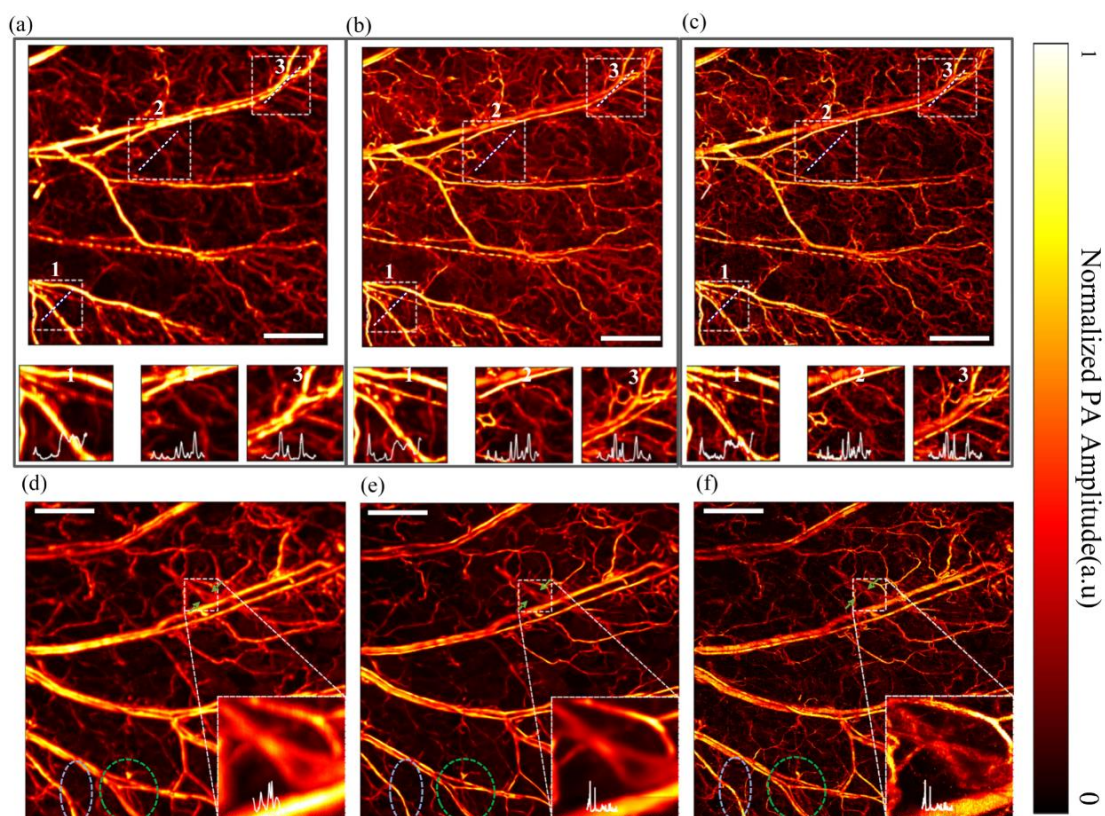
Figure 6-5 (a) AR-PAM image of a mouse ear; (b) Network output based on (a); (c) The corresponding OR-PAM image as the ground truth; (d) Another AR-PAM image of mouse ear; (e) Network output based on (d); (f) The corresponding OR-PAM image as the ground truth. The insets are the zoom-in of the circled regions. (Scale bar: 1 mm).

6.3.3 Comparison between deep learning and deconvolution

Deconvolution is a common imaging processing method to improve spatial resolution and contrast, which has been widely used for optical imaging technologies, including

optical coherence tomography (OCT) [159, 160], two-photon microscopy [161, 162], and confocal microscopy [163]. Recently, deconvolution also has been applied in PACT and AR-PAM to enhance image performance [164-167]. Thus, the performances of the deconvolution and the proposed deep learning schemes are compared. Figures 6-6(a-d) show a series of mouse ear images of the same field of view with AR-PAM, deep learning, deconvolution, and OR-PAM (as the ground truth), respectively. As seen, both deep learning method and deconvolution can increase the image quality of AR-PAM, but more small blood vessels, especially the capillaries, generate higher PA signals through deep learning. To visualize the differences more clearly, signal intensities along the white dotted lines are extracted. It can be seen that signal fluctuations with deep learning are almost the same as those of the ground truth, while the deconvolution method changes the contrasts of the intensity peaks, especially for the middle one. Furthermore, quantitative comparisons, including peak signal-to-noise ratio (PSNR), structural similarity (SSIM), and Pearson's correlation coefficient (PCC), are also summarized, as shown in Figure 6-6(e-g). For PSNR, the deep learning method can increase the value from 17 to 20, while the deconvolution method can only increase up to 19. The SSIM was raised from 0.34 to 0.46 and 0.39 with deep learning and deconvolution, respectively. The PCC parameter elevates with deep learning but decreases via deconvolution. Combining all these parameters, the deep learning method works considerably better than the blind deconvolution method, with all metrics improved reasonably.
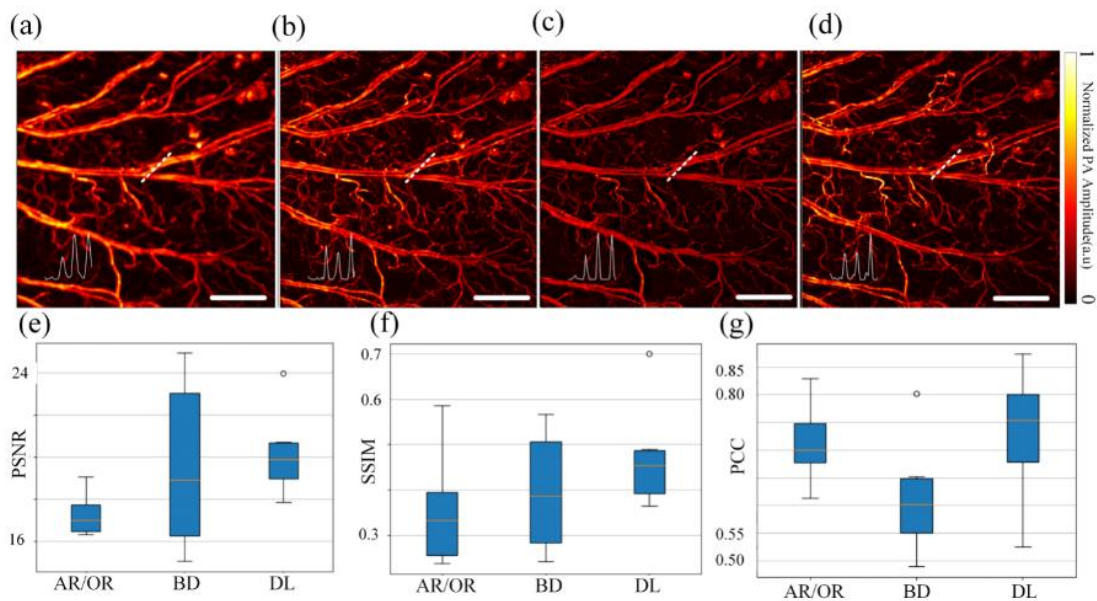
Figure 6-6 Comparison of imaging enhancement between deconvolution and deep learning. BD, blind deconvolution; DL, deep learning. (a) AR-PAM image of a mouse ear; (b) Deep learning network output image based on (a); (c) Deconvolution image based on (a); (d) The corresponding OR-PAM image as the ground truth; (e-f) Comparisons of PSNR, SSIM, and PCC for AR-PAM, deconvolution, and deep learning output with respect to OR-PAM, respectively. (Scale bar: 1 mm).

6.3.4 Maximum image recovery depth of the network

To quantify the capability of this network "recovering ability", the chicken breast tissue was sliced into different thicknesses to cover on human hairs to mimic tissue layers of different depths. Four human hairs were crossed with each other. An OR-PAM image of pure human hairs was collected first, which is set as the ground truth as shown in Figure 6-7a. From the OR-PAM image, the boundaries of hairs are clearly resolved. Due to the high resolution, these four hairs' depth information can be easily obtained from the crossing points, and the orders of these four hairs from top to bottom are 1, 2,

80

3 and 4, respectively, as labelled in the figure. Then a few AR-PAM images at different depths (0 μm, 1000 μm and 1700 μm) were collected (Figures 6-7b-d) and sent to the network to investigate the maximum recovery depth that the network can achieve. As seen, all the boundaries of human hairs are not clear in the AR images. The hairs seem to be wider compared with how they are resolved by OR-PAM, and some artefacts appear around the hair boundaries. Moreover, it becomes difficult to tell the relative depth information via the crossing points of four human hairs. With deep learning, as shown in Figures 6-7(e-g), the widths of human hairs can be recovered to their true levels and the boundaries become clear. The overall image quality for all these three groups have been improved significantly from their AR-PAM bases. However, not all network outputs can distinguish the depth information, and the recovery effects highly depends on the features of the original AR image. For example, the recovery quality of network output at depth 0 μm is best, and the depth information of human hairs can be differentiated from the crossing points clearly, which is very close to that in OR-PAM. With increased tissue depths to 1000 μm and 1700 μm, the hairs in the network output are not continuously, which is consistent with the input AR images shown in Figures 6-7(c-d). This is reasonable as the deep learning network improves the resolution based on the input data and it cannot elevate information that is not represented in the input data. If the input data (AR-PAM image) is obtained from deeper tissue region, the network can help improve the image quality. In this study, as shown in Figure 6-7f, the maximum recovery depth of the network to OR-PAM resolution is around 1000 μm, which has approached or even surpassed the optical diffusion limit in biological tissues at 532 nm wavelength used in this study. As a matter of fact, the penetration depth of

OR-PAM at the captioned wavelength has been typically limited within 900 μm beneath tissue surface [168-170].
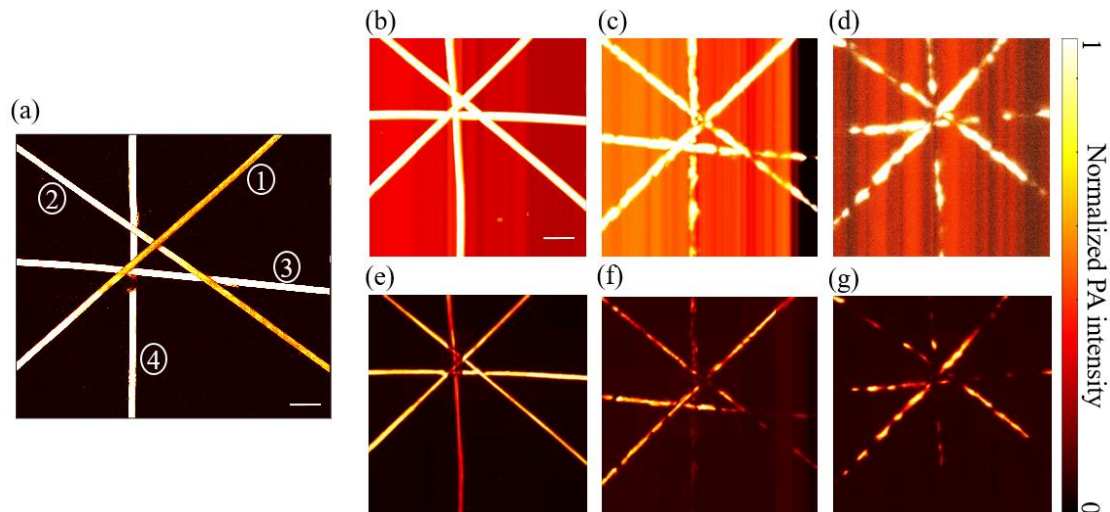
Figure 6-7 (a) OR-PAM image of four human hairs (at depth of 0 μm); (b-d) Experimental AR-PAM images of human hairs under chicken breast tissue sample of depth of 0, 1000, and 1700 μm, respectively (from left to right); (e) Network output images of human hairs under chicken breast tissue sample of depth of 0, 1000, and 1700 μm, respectively (from left to right). (Scale bar: 0.5 mm).

6.3.5 Application for deep mouse brain imaging

Brain imaging is an important topic in biomedicine due to its close tie to many brain studies and diseases, such as stroke and Alzheimer. Research with small animal brain model is a viable bridge to investigate human brain, which has also gained intensive attentions in OR-PAM. As OR-PAM relies on focused light delivery to the region of interest while mouse skull is highly scattering, it is challenging for OR-PAM to image deeply into the brain while retaining a high resolution. Based on what have been demonstrated earlier, it is natural to try the proposed network to see if OR-PAM-like

82

performance can be achieved based on deep-penetrating AR-PAM imaging of mouse brain.

The result is shown in Figure 6-8a. As seen, with the removal of skin, AR-PAM image of the mouse brain has a mediocre resolution and only big blood vessels express strong PA signals. Only a few small blood vessels can be seen due to the insufficiency of SNR and resolution. After deep learning processing, as shown in Figure 6-8b, the overall image quality is improved significantly. The outlines of all blood vessels become clearer and many more small blood vessels are shown up in field of view. Especially, around the central region of the mouse brain, rich capillaries that are invisible with AR-PAM possess strong signals. This result shows clearly that the proposed deep learning scheme can improve the image quality with enhanced SNR and resolution, enabling a performance of OR-PAM with a penetration depth of AR-PAM, as long as the basal AR-PAM possess sufficient SNR as demonstrated earlier. Moreover, AR-PAM has larger step size, resulting in faster raster scanning speed. For the same field of view, imaging speed can increase around 100 times compared with regular OR-PAM. Overall, this deep learning scheme allows for ultrafast "OR-PAM" while maintains AR-PAM penetration depths.
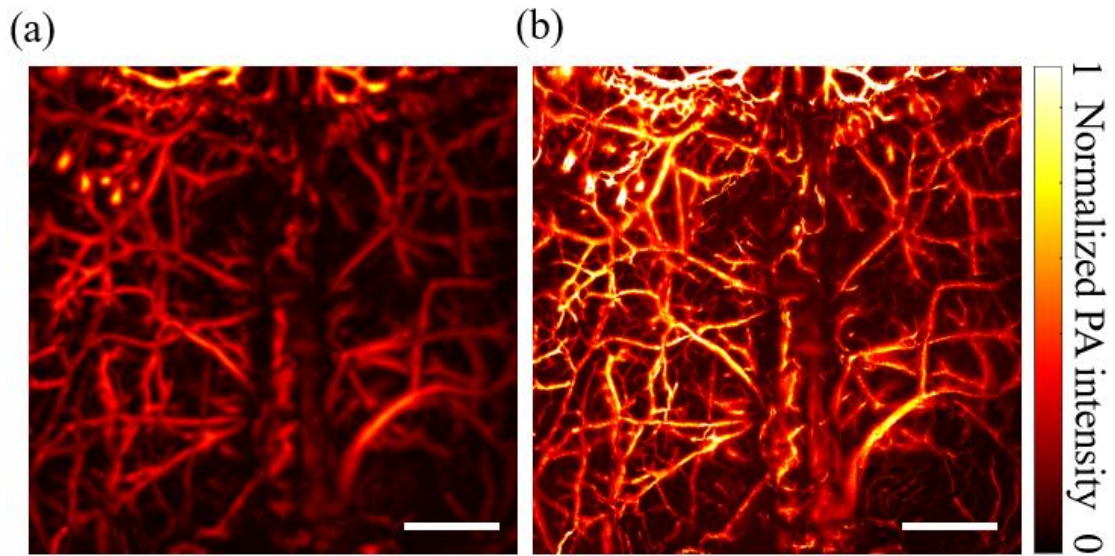
Figure 6-8 (a) AR-PAM image of a mouse brain with skin removed; (b) The corresponding network output image of the mouse brain. (Scale bar: 1 mm).

6.4 Conclusion

In this chapter, deep learning is proposed to combine the advantages of AR-PAM (high SNR and penetration depth) and OR-PAM (resolution), and the feasibility has been tested with mouse ear and brain experiments. A GAN model has been implemented to construct the training network. Limited mice ear data have been collected and data augmented to be used for network training after pre-processing. It is demonstrated that the network can effectively improve the image quality of basal AR-PAM images; the resolution and contrast of the network output has approached that of the ground truth without generating pseudo information such as small blood vessels that are not represented in AR-PAM at all. Compared with the conventional deconvolution method that can also improve imaging resolution, the proposed deep learning scheme outperforms on various levels, including PSNR, SSIM, and PCC. It is also shown the maximum working depth for the proposed network to recover OR-PAM level

resolution is more than 1 mm in chicken breast tissue, which has approached or even surpassed the optical diffusion limit in biological tissues at 532 nm wavelength used in this study. Apart from resolution improvement, using the deep learning scheme equivalently increases the raster scanning speed as the basal AR-PAM adopts much larger step size. Collectively, the proposed deep learning method allows for ultrafast "OR-PAM" imaging with AR-PAM depth, which is beneficial and meaningful for wide biological applications, such as small animal tumour and brain disease diagnosis at depths.

7 CONCLUSION AND FUTURE WORK

7.1 Conclusion

Photoacoustic imaging combines merits of optical contrast and ultrasonic depth and it has drawn intensive attention in recent years. As OR-PAM can obtain structural and functional information on microscale aspect, it has significance for medical diagnosis and treatment. Ultrafast OR-PAM is even more attractive as it has advantages like faster speed, more accurate results, and fewer artefacts. In this thesis, ultrafast OR-PAM is achieved from different aspects of system and algorithm. Furthermore, the ultrafast OR-PAM or its modifications is applied for several representative biomedical applications.

In Chapter 1, an overall introduction of background, the study motivation, and the outlines of the thesis are given. In Chapter 2, a new OR-PAM technique that enables dual-wavelength excitation as fast as 50 ns is presented. Two sequential PA signals are excited with tens of nanoseconds delay through a short optical fiber, while bring significant overlap problem between the two PA signals. To cope with this issue, a Fourier-domain signal separation method is developed to obtain the true signals. It is assumed that the identical waveforms between the two PA signals and thus the amplitude ratio between them can be determined through an optimization problem. In numerical simulation and black tape phantom experiment, this method is validated. The partially overlapped PA signals can be recovered to their original values with high accuracy. Under the circumstance that the PA signals have a reasonably good SNR, the

86

separated PA signals have identical intensities as original ones and the SNR only decreases about ~1.4%. We further demonstrate this separation method on *in vivo* functional OR-PAM. The oxygen saturation of mouse ears is computed on the basis separation results, which is comparable with the ones from conventional method (long optical fiber to generate time delay, without ultrafast wavelength switching). The ultrafast wavelength switching system and the Fourier-domain separation method facilitates OR-PAM with less misalignments caused by different wavelength excitations. It can also potentially increase the pulse energy output in the short fiber due to higher SRS threshold, which benefits to functional OR-PAM that requires high sensitivity, such as the brain imaging, or single-cell imaging.

Chapters 3, 4, and 5 demonstrate three different biomedical applications based on the ultrafast system developed in Chapter 2 or its modifications.

In Chapter 3, a single-shot linear dichroism OR-PAM is developed. Three different polarized laser beams with identical energy from one laser pulse excite on the sample to quantify the linear polarization and orientation angle of it. Similar with the system in Chapter 2, three laser beams with different polarization angles and different time delays are generated via fibers of various lengths from one laser output pulse, and thus the energy fluctuations can be avoided, reducing the misalignments in dichroism detection. This provides sub-microseconds polarization switching, so even in fast scanning, misalignment among different polarizations can be reduced, which is much stable compared with EOM-based system. In one single raster scanning, both the dichroism degree and the orientation angle of the dichroic material can be correctly quantified at the same time. The single-shot dichroism system offers a new strategy to capture the

polarization contrasts of biological tissues, which may be extended to a wide preclinical and clinical applications.

In Chapter 4, we applied OR-PAM to monitor the *in situ* microenvironment parameters changes pre- and post-treatment of a facial cupping therapy on a mouse ear to investigate the mechanism and effectiveness of cupping therapy in the language of modern physiology and medicine. It is found that superficial small blood vessels are congested, showing 37% stronger PA amplitudes just after the cupping compared with pre-treatment. Some capillaries even bleed at the vessel end under the negative pressure. Just after a facial cupping practice (-20 kPa in 5 minutes), an obvious elevation of total haemoglobin concentration in both arteries and veins and around 40% increasement of whole vascular density can be observed, indicating the enhancement of blood circulation with the cupping treatment. Meanwhile, the oxygen saturation values in blood vessels express a markedly decrease, demonstrating that tissue inside the cupping positions consumed more oxygen, promoting the metabolism at the cupping site. All these confirm the effectiveness of cupping. However, such effectiveness seems to last for only a couple of hours. After that, the elevated parameters go back to a level similar to the pre-cupping, suggesting the effect is not sustainable over a longer period of time. The results are very consistent with the finding of other reports [105, 106]. In our tiny pressure and short time treatment, no cupping marks were left. Cupping marks may stay much longer if using higher pressure and longer time. This study is the first time to apply imaging technique to investigate and interpret the cupping therapy. The capability of OR-PAM to quantitatively measure the cupping therapy practice is verified and it may be used to control the pressure and time duration and evaluate the effectiveness of cupping therapy.

In Chapter 5, a new strategy for measuring the liquid viscosity in the microfluidic tube by using the dual-pulse photoacoustic flowmeter method is proposed. The mathematical model is experimentally confirmed and the measured liquid viscosity is well consistent with the actual values after system calibration. The dual-pulse photoacoustic viscosity measurement method only uses conventional microfluidic tubes without a specially designed supporting structure, which greatly reduces the complexity of system design and liquid viscosity measurement operations. In addition, we only uses 1.25 seconds to complete the test, which can still be considerably shortened if necessary. The platform requires only a very small amount of sample (one drop, < 50 µL), which is essential for precious and scarce samples. Last but not least, this Grueneisen-based dual-pulse photoacoustic viscosity measurement method can improve detection sensitivity compared with spectroscopic photoacoustic measurement method [131].

In Chapter 6, the combination of photoacoutic imaging and deep learning is proposed to achieve "OR-PAM" imaging performance through learning the AR-PAM images that scan faster and penetrate deeper. The integration merges the benefits of OR-PAM's high resolution and AR-PAM's deeper penetration depth with fast imaging speed. A GAN deep learning model has been adopted to meet the requirements. Experiments show that the trained network can improve the image quality of mouse ear/brain PA images without producing pseudo blood vessels. The quality is comparable with the OR-PAM images. The network is confirmed to possess better ability, as represented by key quantitative parameters, than conventional deconvolution method does. Moreover, the OR-PAM-like resolution performance generated by the network can find a maximum depth of up to 1.7 mm in chicken breast tissue at 532 nm wavelength. It

breaks the ~1 mm diffusion limit of physical OR-PAM and is limited solely by the SNR of AR-PAM, which, in theory, can goes as deep as multiple millimetres. On the other hand, deep learning with basal AR-PAM images also increases the raster scanning speed due to much larger step size in AR-PAM. Collectively, this deep learning method helps to achieve ultrafast PAM imaging with resolution transformation from AR-PAM to OR-PAM, and it combines the advantages of AR-PAM (deep penetration and fast scanning) and OR-PAM (high resolution), which is beneficial and meaningful for wide biological applications, such as deep-tissue tumor detection and brain disease diagnosis.

7.2 Future work

This thesis mainly focuses on ultrafast OR-PAM system and its biomedical applications. These applications are, however, still limited to some *in vitro* targets or in a very shallow depth, which may not be enough to interpret more advanced mechanisms or phenomena happened in deep tissue. In addition, although the ultrafast dual-wavelength switching and signal separation method is not confined to the current OR-PAM system, faster scanning probe is desired to investigate dynamic physiological activities. The system mainly uses two wavelengths and only obtain few functional parameters, but comprehensive assessments of biology state prefer more parameters for accurate analysis. Thus, combining three main aspects (depth, speed, and multifunction) into one system should be investigated in the future based on the current OR-PAM system.

To improve the imaging speed, some adjustments can be applied in the stepper motor scanning probe. The speed of the current stepper motor scanning probe is limited by the mechanical module, which is quite time-consuming. With an unchanged laser, changing the scanning mode of the probe to a faster one is a feasible pathway. Popular

versions of fast scanning probe include galvanometer mirror [171], water-immersed MEMS scanning mirror [172], water-immersed polygon scanner [173], and voice-coil scanner [87]. All these scanning probes can increase the scanning speed by hundreds to thousands of times compared with the stepper motor. We can choose one of them to be combined to our short-delayed dual-wavelength system. Moreover, we can apply the proposed deep learning framework to further improve the scanning speed via larger step size scanning and hence fewer scanning positions.

To obtain more functional parameters, two wavelengths are not enough. To assess physiological state of living creatures, total hemoglobin concentration and oxygen saturation may not be enough. Multiple wavelengths for more functional parameters are more favourable to comprehensively assess the physiological states. Using multiple wavelengths such as 532 nm, 545 nm, 558 nm, and 1064 nm can not only obtain the conventional parameters, as depth (532 nm), total hemoglobin concentration (532 nm), oxygen saturation (532 and 558 nm), and blood flow speed (532 and 545 nm), but also can monitor blood viscosity (two 532 nm), tumor-vascular interaction (532, 545, and 1064 nm), etc. In order to maintain the high energy output for multiple wavelengths originated from one laser pulse, signal separation method similar to the one developed in Chapter 2 should be applied. In Chapter 2, we only separate two overlapped PA signals to achieve ultrafast dual-wavelength excitations. In the situation multiple wavelengths output, it means lower energy for each wavelength, which may be not enough in experiment. To overcome that, shorter fibers should be used. In this situation, overlapping of PA signals will occur. Thus, separating three or more overlapped PA signals is significantly meaningful. The principle is similar to the dual-signal separation and the optimization problems expands to 2 parameters for three wavelengths or n

parameters for (n+1) wavelengths. Separating more wavelengths can help to realize ultrafast multi-parameter high energy OR-PAM, which is essential for functional OR-PAM in where requiring high sensitivity, such as deep brain imaging and single-red-blood-cell imaging.

Last but not the least, imaging deeper while maintaining high resolution is essential in investigating biological activities, which, however, is highly challenging as the signal of OR-PAM relies on focused light delivery at the region of interest yet light is strongly scattered at depth in tissue. The deep learning framework, as proposed in Chapter 6, is one effective method to reach the goal of OR-PAM while retaining the depth and speed of AR-PAM. That said, the imaging depth afforded by AR-PAM is still limited. Thus, another branch of photoacoutic imaging, PACT, may also need to be included to the deep learning framework. It may be possible to realize image transformation from deep-penetrating low-resolution of PACT to high-resolution OR-PAM or AR-PAM. On the other hand, it has been demonstrated that with photoacoustically guided wavefront shaping [71], it is possible to achieve focused light at depths in biological tissue, which opens a new landscape for OR-PAM in deep biological tissue. Although this technique is currently limited by the time of focusing and refocusing [139, 174], it may see breakthroughs in the near future. Both two methods have great significance for deeper imaging and diagnosis, which is meaningful beyond OR-PAM for various biomedical applications.

After achieving ultrafast multi-parameters deep-penetrating OR-PAM, many biomedical applications can be extended or inspired. For example, the concept proposed in Chapter 4, OR-PAM for monitoring of cupping therapy, can be extended for

preclinical and clinical studies. In this thesis, the investigation is limited to one group of cupping treatment condition (-20 kPa, 5 minutes) with small animal model that has a shallow depth (less than 1 mm). In order to accurately quantify the cupping treatment effects and look for optimal treatment conditions, more pressure and treatment duration groups should be studied and compared. Moreover, more parameters, including but are not limited to flow speed changes, blood viscosity, and pressure around the cupping sites, should be calculated and compared in different situations. In addition, future explorations should move onto human patients, and AR-PAM or PACT may be applied to visualize deeper (mm~cm) microenvironmental changes associated with cupping and/or other treatments.

As mentioned earlier, demonstrated applications in this thesis mainly contain *in vitro* targets and a few *in vivo* targets. In the future, more diseased-related problems will be explored. Nowadays, many clinical problems lack effective imaging proofs or evidence. For example, cardiovascular disease is a major clinical challenge that threatens human health, and its morbidity ranks first worldwide. There some existing laboratory imaging technologies for small animal myocardial microcirculation evaluation, including high-frequency ultrasound, micro-CT, micro MRI, etc. These imaging modalities, however, cannot provide dynamic and direct evaluation of the microscale structural and functional parameters, such as hemodynamic of microcirculation. PA imaging has brought new opportunities for the diagnosis of myocardial microcirculation disorders from imaging aspects. Thus, this type of clinically-central topics will be investigated with PA of my next phase of research.

REFERENCES

[1]   L. V. W. H. W, *Biomedical Optics, Principles and Imaging* New Jersey: John Wiley and Sons, 2007.

[2]   A. P. Gibson, J. C. Hebden, and S. R. Arridge, "Recent advances in diffuse optical imaging," *Physics in Medicine and Biology,* vol. 50, no. 4, pp. R1-R43, Feb 21, 2005.

[3]   T. V, *Tissue Optics: Light Scattering Methods ann Instruments for Medical Diagnosis*: Bellingham, Washington USA: The Society of Photo-Optical Instrumentation Engineers, 2007.

[4]   L. H. V. Wang, and S. Hu, "Photoacoustic Tomography: In Vivo Imaging from Organelles to Organs," *Science,* vol. 335, no. 6075, pp. 1458-1462, Mar 23, 2012.

[5]   P. Beard, "Biomedical photoacoustic imaging," *Interface Focus,* vol. 1, no. 4, pp. 602-31, Aug 6, 2011.

[6]   L. H. V. Wang, and J. J. Yao, "A practical guide to photoacoustic tomography in the life sciences," *Nature Methods,* vol. 13, no. 8, pp. 627-638, Aug, 2016.

[7]   L. V. Wang, "Ultrasound-mediated biophotonic imaging: a review of acousto-optical tomography and photo-acoustic tomography," *Dis Markers,* vol. 19, no. 2-3, pp. 123-38, 2003.

[8]   M. H. Xu, and L. H. V. Wang, "Photoacoustic imaging in biomedicine," *Review of Scientific Instruments,* vol. 77, no. 4, Apr, 2006.

[9]   C. B. Sussman, C. Rossignol, Q. Z. Zhang, H. B. Jiang, T. Zheng, D. Steindler, L. D. Young, and M. D. Weiss, "Photoacoustic tomography can detect cerebral hemodynamic alterations in a neonatal rodent model of hypoxia-ischemia," *Acta Neurobiologiae Experimentalis,* vol. 72, no. 3, pp. 253-263, 2012.

[10]   R. Kiesslich, M. Goetz, A. Hoffman, and P. R. Galle, "New imaging techniques and opportunities in endoscopy," *Nature Reviews Gastroenterology & Hepatology,* vol. 8, no. 10, pp. 547-553, Oct, 2011.

[11]   L. M. Nie, X. Cai, K. Maslov, A. Garcia-Uribe, M. A. Anastasio, and L. H. V. Wang, "Photoacoustic tomography through a whole adult human skull with a photon recycler," *Journal of Biomedical Optics,* vol. 17, no. 11, Nov, 2012.

[12]   A. de la Zerda, Y. M. Paulus, R. Teed, S. Bodapati, Y. Dollberg, B. T. Khuri-Yakub, M. S. Blumenkranz, D. M. Moshfeghi, and S. S. Gambhir,

"Photoacoustic ocular imaging," *Optics Letters,* vol. 35, no. 3, pp. 270-272, Feb 1, 2010.

[13] S. Hu, B. Rao, K. Maslov, and L. V. Wang, "Label-free photoacoustic ophthalmic angiography," *Optics Letters,* vol. 35, no. 1, pp. 1-3, Jan 1, 2010.

[14] J. G. Zhang, and H. F. Liu, "Functional imaging and endoscopy," *World Journal of Gastroenterology,* vol. 17, no. 38, pp. 4277-4282, Oct 14, 2011.

[15] J. Levi, S. R. Kothapalli, T. J. Ma, K. Hartman, B. T. Khuri-Yakub, and S. S. Gambhir, "Design, Synthesis, and Imaging of an Activatable Photoacoustic Probe," *Journal of the American Chemical Society,* vol. 132, no. 32, pp. 11264-11269, Aug 18, 2010.

[16] S. Manohar, S. E. Vaartjes, J. C. G. van Hespen, J. M. Klaase, F. M. van den Engh, W. Steenbergen, and T. G. van Leeuwen, "Initial results of in vivo non-invasive cancer imaging in the human breast using near-infrared photoacoustics," *Optics Express,* vol. 15, no. 19, pp. 12277-12285, Sep 17, 2007.

[17] R. A. Kruger, R. B. Lam, D. R. Reinecke, S. P. Del Rio, and R. P. Doyle, "Photoacoustic angiography of the breast," *Medical Physics,* vol. 37, no. 11, pp. 6096-6100, Nov, 2010.

[18] S. A. Ermilov, T. Khamapirad, A. Conjusteau, M. H. Leonard, R. Lacewell, K. Mehta, T. Miller, and A. A. Oraevsky, "Laser optoacoustic imaging system for detection of breast cancer," *Journal of Biomedical Optics,* vol. 14, no. 2, Mar-Apr, 2009.

[19] T. Kitai, M. Torii, T. Sugie, S. Kanao, Y. Mikami, T. Shiina, and M. Toi, "Photoacoustic mammography: initial clinical results," *Breast Cancer,* vol. 21, no. 2, pp. 146-153, Mar, 2014.

[20] M. Heijblom, D. Piras, W. Xia, J. C. G. van Hespen, J. M. Klaase, F. M. van den Engh, T. G. van Leeuwen, W. Steenbergen, and S. Manohar, "Visualizing breast cancer using the Twente photoacoustic mammoscope: What do we learn from twelve new patient measurements?," *Optics Express,* vol. 20, no. 11, pp. 11582-11597, May 21, 2012.

[21] L. Xi, S. R. Grobmyer, L. Wu, R. M. Chen, G. Y. Zhou, L. G. Gutwein, J. J. Sun, W. J. Liao, Q. F. Zhou, H. K. Xie, and H. B. Jiang, "Evaluation of breast tumor margins in vivo with intraoperative photoacoustic imaging," *Optics Express,* vol. 20, no. 8, pp. 8726-8731, Apr 9, 2012.

[22] C. Kim, H. M. Song, X. Cai, J. J. Yao, A. Wei, and L. H. V. Wang, "In vivo photoacoustic mapping of lymphatic systems with plasmon-resonant nanostars," *Journal of Materials Chemistry,* vol. 21, no. 9, pp. 2841-2844, 2011.

[23] S. W. T. P. J. Heijmink, J. J. Futterer, S. S. Strum, W. J. G. Oyen, F. Frauscher, J. A. Witjes, and J. O. Barentsz, "State-of-the-art

uroradiologic imaging in the diagnosis of prostate cancer," *Acta Oncologica,* vol. 50, pp. 25-38, Jun, 2011.

[24]   Y. Sun, E. S. Sobel, and H. B. Jiang, "First assessment of three-dimensional quantitative photoacoustic tomography for in vivo detection of osteoarthritis in the finger joints," *Medical Physics,* vol. 38, no. 7, pp. 4009-4017, Jul, 2011.

[25]   X. D. Wang, D. L. Chamberland, and D. A. Jamadar, "Noninvasive photoacoustic tomography of human peripheral joints toward diagnosis of inflammatory arthritis," *Optics Letters,* vol. 32, no. 20, pp. 3002-3004, Oct 15, 2007.

[26]   L. Smith, and S. MacNeil, "State of the art in non-invasive imaging of cutaneous melanoma," *Skin Research and Technology,* vol. 17, no. 3, pp. 257-269, Aug, 2011.

[27]   S. Park, C. Lee, J. Kim, and C. Kim, "Acoustic resolution photoacoustic microscopy," *Biomedical Engineering Letters,* vol. 4, no. 3, pp. 213-222, 2014.

[28]   S. Jeon, J. Park, R. Managuli, and C. Kim, "A Novel 2-D Synthetic Aperture Focusing Technique for Acoustic-Resolution Photoacoustic Microscopy," *IEEE Trans Med Imaging,* vol. 38, no. 1, pp. 250-260, Jan, 2019.

[29]   J. Yao, and L. V. Wang, "Sensitivity of photoacoustic microscopy," *Photoacoustics,* vol. 2, no. 2, pp. 87-101, Jun, 2014.

[30]   J. V. Frangioni, "New technologies for human cancer imaging," *Journal of Clinical Oncology,* vol. 26, no. 24, pp. 4012-4021, Aug 20, 2008.

[31]   M. L. Li, J. T. Oh, X. Y. Xie, G. Ku, W. Wang, C. Li, G. Lungu, G. Stoica, and L. V. Wang, "Simultaneous molecular and hypoxia imaging of brain tumors in vivo using spectroscopic photoacoustic tomography," *Proceedings of the Ieee,* vol. 96, no. 3, pp. 481-489, Mar, 2008.

[32]   X. Wang, G. Ku, M. A. Wegiel, D. J. Bornhop, G. Stoica, and L. V. Wang, "Noninvasive photoacoustic angiography of animal brains in vivo with near-infrared light and an optical contrast agent," *Optics Letters,* vol. 29, no. 7, pp. 730-732, 2004/04/01, 2004.

[33]   W. Bost, Y. Kohl, F. Stracke, M. Fournelle, and R. Lemor, "High resolution optoacoustic detection of nanoparticles on living cells." pp. 120-123.

[34]   L. Brannon-Peppas, and J. O. Blanchette, "Nanoparticle and targeted systems for cancer therapy," *Adv Drug Deliv Rev,* vol. 56, no. 11, pp. 1649-59, Sep 22, 2004.

[35]   X. Yang, E. W. Stein, S. Ashkenazi, and L. V. Wang, "Nanoparticles for photoacoustic imaging," *Wiley interdisciplinary reviews: nanomedicine and nanobiotechnology,* vol. 1, no. 4, pp. 360-368, 2009.

[36]   C. Kim, C. Favazza, and L. H. V. Wang, "In Vivo Photoacoustic Tomography of Chemicals: High-Resolution Functional and Molecular

Optical Imaging at New Depths," *Chemical Reviews,* vol. 110, no. 5, pp. 2756-2782, May, 2010.

[37]   D. Yeager, A. Karpiouk, B. Wang, J. Amirian, K. Sokolov, R. Smalling, and S. Emelianov, "Intravascular photoacoustic imaging of exogenously labeled atherosclerotic plaque through luminal blood," *Journal of Biomedical Optics,* vol. 17, no. 10, Oct, 2012.

[38]   J. Weber, P. C. Beard, and S. E. Bohndiek, "Contrast agents for molecular photoacoustic imaging," *Nature Methods,* vol. 13, no. 8, pp. 639-650, Aug, 2016.

[39]   D. Pan, B. Kim, L. H. V. Wang, and G. M. Lanza, "A brief account of nanoparticle contrast agents for photoacoustic imaging," *Wiley Interdisciplinary Reviews-Nanomedicine and Nanobiotechnology,* vol. 5, no. 6, pp. 517-543, Nov, 2013.

[40]   G. P. Luke, D. Yeager, and S. Y. Emelianov, "Biomedical applications of photoacoustic imaging with exogenous contrast agents," *Annals of biomedical engineering,* vol. 40, no. 2, pp. 422-437, 2012.

[41]   J. Chen, Y. Zhang, L. He, Y. Liang, and L. Wang, "Wide-field polygon-scanning photoacoustic microscopy of oxygen saturation at 1-MHz A-line rate," *Photoacoustics,* vol. 20, pp. 100195, 2020.

[42]   Z. Chen, S. Yang, and D. Xing, "In vivo detection of hemoglobin oxygen saturation and carboxyhemoglobin saturation with multiwavelength photoacoustic microscopy," *Optics letters,* vol. 37, no. 16, pp. 3414-3416, 2012.

[43]   C. Liu, Y. Liang, and L. Wang, "Optical-resolution photoacoustic microscopy of oxygen saturation with nonlinear compensation," *Biomedical optics express,* vol. 10, no. 6, pp. 3061-3069, 2019.

[44]   C. Liu, Y. Liang, and L. Wang, "Single-shot photoacoustic microscopy of hemoglobin concentration, oxygen saturation, and blood flow in sub-microseconds," *Photoacoustics,* vol. 17, pp. 100156, Mar, 2020.

[45]   B. Ning, M. J. Kennedy, A. J. Dixon, N. Sun, R. Cao, B. T. Soetikno, R. Chen, Q. Zhou, K. K. Shung, and J. A. Hossack, "Simultaneous photoacoustic microscopy of microvascular anatomy, oxygen saturation, and blood flow," *Optics letters,* vol. 40, no. 6, pp. 910-913, 2015.

[46]   J. Yao, K. I. Maslov, Y. Zhang, Y. Xia, and L. V. Wang, "Label-free oxygen-metabolic photoacoustic microscopy in vivo," *Journal of biomedical optics,* vol. 16, no. 7, pp. 076003, 2011.

[47]   J. Yao, L. Wang, J.-M. Yang, K. I. Maslov, T. T. Wong, L. Li, C.-H. Huang, J. Zou, and L. V. Wang, "High-speed label-free functional photoacoustic microscopy of mouse brain in action," *Nature methods,* vol. 12, no. 5, pp. 407-410, 2015.

[48]   D. Hanahan, and R. A. Weinberg, "Hallmarks of cancer: the next generation," *cell,* vol. 144, no. 5, pp. 646-674, 2011.

[49]   F. Cao, Z. Qiu, H. Li, and P. Lai, "Photoacoustic imaging in oxygen detection," *Applied Sciences,* vol. 7, no. 12, pp. 1262, 2017.

[50]   H. F. Zhang, K. Maslov, G. Stoica, and L. V. Wang, "Functional photoacoustic microscopy for high-resolution and noninvasive in vivo imaging," *Nature biotechnology,* vol. 24, no. 7, pp. 848-851, 2006.

[51]   Y. Liang, L. Jin, B.-O. Guan, and L. Wang, "2 MHz multi-wavelength pulsed laser for functional photoacoustic microscopy," *Optics letters,* vol. 42, no. 7, pp. 1452-1455, 2017.

[52]   R. Cao, J. Li, B. Ning, N. Sun, T. Wang, Z. Zuo, and S. Hu, "Functional and oxygen-metabolic photoacoustic microscopy of the awake mouse brain," *Neuroimage,* vol. 150, pp. 77-87, 2017.

[53]   M. Moothanchery, R. Bi, J. Y. Kim, G. Balasundaram, C. Kim, and M. C. Olivo, "High-speed simultaneous multiscale photoacoustic microscopy," *Journal of biomedical optics,* vol. 24, no. 8, pp. 086001, 2019.

[54]   W. Song, Q. Xu, Y. Zhang, Y. Zhan, W. Zheng, and L. Song, "Fully integrated reflection-mode photoacoustic, two-photon and second harmonic generation microscopy in vivo," *Scientific reports,* vol. 6, no. 1, pp. 1-8, 2016.

[55]   H. Kang, S. W. Lee, S. M. Park, S. W. Cho, J. Y. Lee, C. S. Kim, and T. G. Lee, "Real-time functional optical-resolution photoacoustic microscopy using high-speed alternating illumination at 532 and 1064 nm," *Journal of biophotonics,* vol. 11, no. 3, pp. e201700210, 2018.

[56]   T. Wang, N. Sun, R. Cao, B. Ning, R. Chen, Q. Zhou, and S. Hu, "Multiparametric photoacoustic microscopy of the mouse brain with 300-kHz A-line rate," *Neurophotonics,* vol. 3, no. 4, pp. 045006, Oct, 2016.

[57]   J. J. Yao, and L. H. V. Wang, "Photoacoustic microscopy," *Laser & Photonics Reviews,* vol. 7, no. 5, pp. 758-778, Sep, 2013.

[58]   P. Beard, "Biomedical photoacoustic imaging," *Interface Focus,* vol. 1, no. 4, pp. 602-631, Aug 6, 2011.

[59]   H. F. Zhang, K. Maslov, G. Stoica, and L. H. V. Wang, "Functional photoacoustic microscopy for high-resolution and noninvasive in vivo imaging," *Nature Biotechnology,* vol. 24, no. 7, pp. 848-851, Jul, 2006.

[60]   F. Cao, Z. H. Qiu, H. H. Li, and P. X. Lai, "Photoacoustic Imaging in Oxygen Detection," *Applied Sciences-Basel,* vol. 7, no. 12, Dec, 2017.

[61]   Y. Z. Liang, L. Jin, B. O. Guan, and L. D. Wang, "2 MHz multi-wavelength pulsed laser for functional photoacoustic microscopy," *Optics Letters,* vol. 42, no. 7, pp. 1452-1455, Apr 1, 2017.

[62]   W. Shi, P. Hajireza, P. Shao, A. Forbrich, and R. J. Zemp, "In vivo near-realtime volumetric optical-resolution photoacoustic microscopy using a high-repetition-rate nanosecond fiber-laser," *Optics Express,* vol. 19, no. 18, pp. 17143-17150, Aug 29, 2011.

[63] Y. Yamaoka, Y. Harada, M. Sakakura, T. Minamikawa, S. Nishino, S. Maehara, S. Hamano, H. Tanaka, and T. Takamatsu, "Photoacoustic microscopy using ultrashort pulses with two different pulse durations," *Optics Express,* vol. 22, no. 14, pp. 17063-17072, Jul 14, 2014.

[64] B. Ning, M. J. Kennedy, A. J. Dixon, N. D. Sun, R. Cao, B. T. Soetikno, R. M. Chen, Q. F. Zhou, K. K. Shung, J. A. Hossack, and S. Hu, "Simultaneous photoacoustic microscopy of microvascular anatomy, oxygen saturation, and blood flow," *Optics Letters,* vol. 40, no. 6, pp. 910-913, Mar 15, 2015.

[65] Y. Wang, S. Hu, K. Maslov, Y. Zhang, Y. N. Xia, and L. V. Wang, "In vivo integrated photoacoustic and confocal microscopy of hemoglobin oxygen saturation and oxygen partial pressure," *Optics Letters,* vol. 36, no. 7, pp. 1029-1031, Apr 1, 2011.

[66] S. Hu, K. Maslov, P. Yan, J. M. Lee, and L. V. Wang, "Dichroism Optical-resolution Photoacoustic Microscopy," *Photons Plus Ultrasound: Imaging and Sensing 2012,* vol. 8223, 2012.

[67] P. Hajireza, A. Forbrich, and R. Zemp, "In-Vivo functional optical-resolution photoacoustic microscopy with stimulated Raman scattering fiber-laser source," *Biomed Opt Express,* vol. 5, no. 2, pp. 539-46, Feb 1, 2014.

[68] D. Koeplinger, M. Y. Liu, and T. Buma, "Photoacoustic microscopy with a pulsed multi-color source based on stimulated Raman scattering," *2011 Ieee International Ultrasonics Symposium (Ius)*, pp. 296-299, 2011.

[69] R. H. Stolen, J. P. Gordon, W. J. Tomlinson, and H. A. Haus, "Raman Response Function of Silica-Core Fibers," *Journal of the Optical Society of America B-Optical Physics,* vol. 6, no. 6, pp. 1159-1166, Jun, 1989.

[70] J. F. Andersen, J. Busck, and H. Heiselberg, "Pulsed Raman fiber laser and multispectral imaging in three dimensions," *Applied Optics,* vol. 45, no. 24, pp. 6198-6204, Aug 20, 2006.

[71] P. X. Lai, L. D. Wang, J. W. Tay, and L. H. V. Wang, "Photoacoustically guided wavefront shaping for enhanced optical focusing in scattering media," *Nature Photonics,* vol. 9, no. 2, pp. 126-132, Feb, 2015.

[72] H. F. Zhang, K. Maslov, M. Sivaramakrishnan, G. Stoica, and L. H. V. Wang, "Imaging of hemoglobin oxygen saturation variations in single vessels in vivo using photoacoustic microscopy," *Applied Physics Letters,* vol. 90, no. 5, Jan 29, 2007.

[73] B. Norden, M. Kubista, and T. Kurucsev, "Linear Dichroism Spectroscopy of Nucleic-Acids," *Quarterly Reviews of Biophysics,* vol. 25, no. 1, pp. 51-170, Feb, 1992.

[74] B. M. Bulheller, A. Rodger, and J. D. Hirst, "Circular and linear dichroism of proteins," *Physical Chemistry Chemical Physics,* vol. 9, no. 17, pp. 2020-2035, 2007.

[75] J. S. Qiao, X. H. Kong, Z. X. Hu, F. Yang, and W. Ji, "High-mobility transport anisotropy and linear dichroism in few-layer black phosphorus," *Nature Communications,* vol. 5, Jul, 2014.

[76] B. Norden, "Applications of Linear Dichroism Spectroscopy," *Applied Spectroscopy Reviews,* vol. 14, no. 2, pp. 157-248, 1978.

[77] K. Razmkhah, N. P. Chmel, M. I. Gibson, and A. Rodger, "Oxidized polyethylene films for orienting polar molecules for linear dichroism spectroscopy," *Analyst,* vol. 139, no. 6, pp. 1372-1382, 2014.

[78] G. Z. Zhang, J. Li, P. Cui, T. Wang, J. Jiang, and O. V. Prezhdo, "Two-Dimensional Linear Dichroism Spectroscopy for Identifying Protein Orientation and Secondary Structure Composition," *Journal of Physical Chemistry Letters,* vol. 8, no. 5, pp. 1031-1037, Mar 2, 2017.

[79] Z. J. Chen, S. H. Yang, and D. Xing, "Optically integrated trimodality imaging system: combined all-optical photoacoustic microscopy, optical coherence tomography, and fluorescence imaging," *Optics Letters,* vol. 41, no. 7, pp. 1636-1639, Apr 1, 2016.

[80] C. Liu, J. Liao, L. Chen, J. Chen, R. Ding, X. Gong, C. Cui, Z. Pang, W. Zheng, and L. Song, "The integrated high-resolution reflection-mode photoacoustic and fluorescence confocal microscopy," *Photoacoustics,* vol. 14, pp. 12-18, Jun, 2019.

[81] M. Seeger, A. Karlas, D. Soliman, J. Pelisek, and V. Ntziachristos, "Multimodal optoacoustic and multiphoton microscopy of human carotid atheroma," *Photoacoustics,* vol. 4, no. 3, pp. 102-111, Sep, 2016.

[82] J. Xia, J. J. Yao, and L. V. Wang, "Photoacoustic Tomography: Principles and Advances," *Progress in Electromagnetics Research-Pier,* vol. 147, pp. 1-22, 2014.

[83] Y. J. Liu, H. H. Liu, H. X. Yan, Y. C. Liu, J. S. Zhang, W. J. Shan, P. X. Lai, H. H. Li, L. Ren, Z. J. Li, and L. M. Nie, "Aggregation-Induced Absorption Enhancement for Deep Near-Infrared II Photoacoustic Imaging of Brain Gliomas In Vivo," *Advanced Science,* vol. 6, no. 8, Apr 17, 2019.

[84] X. Huang, W. Shang, H. Deng, Y. Zhou, F. Cao, C. Fang, P. Lai, and J. Tian, "Clothing spiny nanoprobes against the mononuclear phagocyte system clearance in vivo: Photoacoustic diagnosis and photothermal treatment of early stage liver cancer with erythrocyte membrane-camouflaged gold nanostars," *Applied Materials Today*, 2019.

[85] Y. Qu, L. Li, Y. C. Shen, X. M. Wei, T. T. W. Wong, P. Hu, J. J. Yao, K. Maslov, and L. H. V. Wang, "Dichroism-sensitive photoacoustic computed tomography," *Optica,* vol. 5, no. 4, pp. 495-501, Apr 20, 2018.

[86] Z. H. Zhang, Y. J. Sh, L. Z. Xiang, and D. Xing, "Polarized photoacoustic microscopy for vectorial-absorption-based anisotropy detection," *Optics Letters,* vol. 43, no. 21, pp. 5267-5270, Nov 1, 2018.

[87]   L. D. Wang, K. Maslov, J. J. Yao, B. Rao, and L. H. V. Wang, "Fast voice-coil scanning optical-resolution photoacoustic microscopy," *Optics Letters,* vol. 36, no. 2, pp. 139-141, Jan 15, 2011.

[88]   L. D. Wang, C. Zhang, and L. H. V. Wang, "Grueneisen Relaxation Photoacoustic Microscopy," *Physical Review Letters,* vol. 113, no. 17, Oct 20, 2014.

[89]   L. D. Wang, K. Maslov, and L. H. V. Wang, "Single-cell label-free photoacoustic flowoxigraphy in vivo," *Proceedings of the National Academy of Sciences of the United States of America,* vol. 110, no. 15, pp. 5759-5764, Apr 9, 2013.

[90]   J. I. Kim, M. S. Lee, D. H. Lee, K. Boddy, and E. Ernst, "Cupping for Treating Pain: A Systematic Review," *Evidence-Based Complementary and Alternative Medicine*, pp. 1-7, 2011.

[91]   H. J. Cao, M. Han, X. Li, S. J. Dong, Y. M. Shang, Q. A. Wang, S. Xu, and J. P. Liu, "Clinical research evidence of cupping therapy in China: a systematic literature review," *Bmc Complementary and Alternative Medicine,* vol. 10, Nov 16, 2010.

[92]   P. Mehta, and V. Dhapte, "Cupping therapy: A prudent remedy for a plethora of medical ailments," *J Tradit Complement Med,* vol. 5, no. 3, pp. 127-34, Jul, 2015.

[93]   N. A. Qureshi, G. I. Ali, T. S. Abushanab, A. T. El-Olemy, M. S. Alqaed, I. S. El-Subai, and A. M. N. Al-Bedah, "History of cupping (Hijama): a narrative review of literature," *Journal of Integrative Medicine-Jim,* vol. 15, no. 3, pp. 172-181, May, 2017.

[94]   H. J. Cao, C. J. Zhu, and J. P. Liu, "Wet Cupping Therapy for Treatment of Herpes Zoster: A Systematic Review of Randomized Controlled Trials," *Alternative Therapies in Health and Medicine,* vol. 16, no. 6, pp. 48-54, Nov-Dec, 2010.

[95]   H. J. Cao, J. P. Liu, and G. T. Lewith, "Traditional Chinese Medicine for Treatment of Fibromyalgia: A Systematic Review of Randomized Controlled Trials," *Journal of Alternative and Complementary Medicine,* vol. 16, no. 4, pp. 397-409, Apr, 2010.

[96]   H. J. Cao, H. Hu, B. Colagiuri, and J. P. Liu, "Medicinal Cupping Therapy in 30 Patients with Fibromyalgia: A Case Series Observation," *Forschende Komplementarmedizin,* vol. 18, no. 3, pp. 122-126, 2011.

[97]   C. J. Hogeboom, K. J. Sherman, and D. C. Cherkin, "Variation in diagnosis and treatment of chronic low back pain by traditional Chinese medicine acupuncturists," *Complementary Therapies in Medicine,* vol. 9, no. 3, pp. 154-166, Sep, 2001.

[98]   J. Koo, and S. Arain, "Traditional Chinese medicine for the treatment of dermatologic disorders," *Archives of Dermatology,* vol. 134, no. 11, pp. 1388-1393, Nov, 1998.

[99]   J. Koo, and S. Arain, "Traditional Chinese medicine in dermatology," *Clinics in Dermatology,* vol. 17, no. 1, pp. 21-27, Jan-Feb, 1999.

[100]   R. Lauche, H. Cramer, C. Hohmann, K. E. Choi, T. Rampp, F. J. Saha, F. Musial, J. Langhorst, and G. Dobos, "The Effect of Traditional Cupping on Pain and Mechanical Thresholds in Patients with Chronic Nonspecific Neck Pain: A Randomised Controlled Pilot Study," *Evidence-Based Complementary and Alternative Medicine*, 2012.

[101]   A. Michalsen, S. Bock, R. Ludtke, T. Rampp, M. Baecker, J. Bachmann, J. Langhorst, F. Musial, and G. J. Dobos, "Effects of Traditional Cupping Therapy in Patients With Carpal Tunnel Syndrome: A Randomized Controlled Trial," *Journal of Pain,* vol. 10, no. 6, pp. 601-608, Jun, 2009.

[102]   K. J. Sherman, D. C. Cherkin, and C. J. Hogeboom, "The diagnosis and treatment of patients with chronic low-back pain by Traditional Chinese Medical acupuncturists," *Journal of Alternative and Complementary Medicine,* vol. 7, no. 6, pp. 641-650, Dec, 2001.

[103]   J. Wang, and X. J. Xiong, "Evidence-Based Chinese Medicine for Hypertension," *Evidence-Based Complementary and Alternative Medicine*, 2013.

[104]   Y. Wang, X. M. Lin, and G. Q. Zheng, "Traditional Chinese Medicine for Parkinson's Disease in China and Beyond," *Journal of Alternative and Complementary Medicine,* vol. 17, no. 5, pp. 385-388, May, 2011.

[105]   T. Li, Y. X. Li, Y. Lin, and K. Li, "Significant and sustaining elevation of blood oxygen induced by Chinese cupping therapy as assessed by near-infrared spectroscopy," *Biomedical Optics Express,* vol. 8, no. 1, pp. 223-229, Jan 1, 2017.

[106]   C. Y. Gao, M. Wang, L. He, Y. N. He, and T. Li, "Alternations of hemodynamic parameters during Chinese cupping therapy assessed by an embedded near-infrared spectroscopy monitor," *Biomedical Optics Express,* vol. 10, no. 1, pp. 196-203, Jan 1, 2019.

[107]   S. Kim, E. Kim, G. Jung, S. Lee, and J. G. Kim, "The hemodynamic changes during cupping therapy monitored by using an optical sensor embedded cup," *Journal of Biophotonics,* vol. 12, no. 5, May, 2019.

[108]   L. V. Wang, "Multiscale photoacoustic microscopy and computed tomography," *Nature Photonics,* vol. 3, no. 9, pp. 503-509, Sep, 2009.

[109]   P. Lai, L. Wang, J. W. Tay, and L. V. Wang, "Photoacoustically guided wavefront shaping for enhanced optical focusing in scattering media," *Nat Photonics,* vol. 9, no. 2, pp. 126-132, Feb, 2015.

[110]   P. K. Upputuri, and M. Pramanik, "Recent advances toward preclinical and clinical translation of photoacoustic tomography: a review," *Journal of Biomedical Optics,* vol. 22, no. 4, Apr, 2017.

[111]   H. Li, F. Cao, Y. zhou, Z. yu, and P. Lai, "Interferometry-free noncontact photoacoustic detection method based on speckle correlation change," *Optics Letters,* vol. 44, no. 22, 2019.

[112] L. de la Cruz-May, J. A. Alvarez-Chavez, E. B. Mejia, A. Flores-Gil, F. Mendez-Martinez, and S. Wabnitz, "Raman threshold for nth-order cascade Raman amplification," *Optical Fiber Technology,* vol. 17, no. 3, pp. 214-217, May, 2011.

[113] N. Bosschaart, G. J. Edelman, M. C. G. Aalders, T. G. van Leeuwen, and D. J. Faber, "A literature review and novel theoretical approach on the optical properties of whole blood," *Lasers in Medical Science,* vol. 29, no. 2, pp. 453-479, Mar, 2014.

[114] R. Rosencranz, and S. A. Bogen, "Clinical laboratory measurement of serum, plasma, and blood viscosity," *Am J Clin Pathol,* vol. 125 Suppl, pp. S78-86, Jun, 2006.

[115] B. Jakoby, M. Scherer, M. Buskies, and H. Eisenschmid, "An automotive engine oil viscosity sensor," *Ieee Sensors Journal,* vol. 3, no. 5, pp. 562-568, Oct, 2003.

[116] G. D. O. Lowe, M. M. Drummond, A. R. Lorimer, I. Hutton, C. D. Forbes, C. R. M. Prentice, and J. C. Barbenel, "Relation between Extent of Coronary-Artery Disease and Blood-Viscosity," *British Medical Journal,* vol. 280, no. 6215, pp. 673-674, 1980.

[117] G. D. O. Lowe, F. G. R. Fowkes, J. Dawes, P. T. Donnan, S. E. Lennie, and E. Housley, "Blood-Viscosity, Fibrinogen, and Activation of Coagulation and Leukocytes in Peripheral Arterial-Disease and the Normal Population in the Edinburgh Artery Study," *Circulation,* vol. 87, no. 6, pp. 1915-1920, Jun, 1993.

[118] S. Shin, and D. Y. Keum, "Measurement of blood viscosity using mass-detecting sensor," *Biosensors & Bioelectronics,* vol. 17, no. 5, pp. 383-388, May, 2002.

[119] Y. J. Kang, J. Ryu, and S. J. Lee, "Label-free viscosity measurement of complex fluids using reversal flow switching manipulation in a microfluidic channel," *Biomicrofluidics,* vol. 7, no. 4, Jul, 2013.

[120] H. Kim, Y. I. Cho, D. H. Lee, C. M. Park, H. W. Moon, M. Hur, J. Q. Kim, and Y. M. Yun, "Analytical performance evaluation of the scanning capillary tube viscometer for measurement of whole blood viscosity," *Clinical Biochemistry,* vol. 46, no. 1-2, pp. 139-142, Jan, 2013.

[121] W. J. Lan, S. W. Li, J. H. Xu, and G. S. Luo, "Rapid measurement of fluid viscosity using co-flowing in a co-axial microfluidic device," *Microfluidics and Nanofluidics,* vol. 8, no. 5, pp. 687-693, May, 2010.

[122] S. Kim, K. C. Kim, and E. Yeom, "Microfluidic method for measuring viscosity using images from smartphone," *Optics and Lasers in Engineering,* vol. 104, pp. 237-243, May, 2018.

[123] Y. J. Kang, S. Y. Yoon, K. H. Lee, and S. Yang, "A Highly Accurate and Consistent Microfluidic Viscometer for Continuous Blood Viscosity Measurement," *Artificial Organs,* vol. 34, no. 11, pp. 944-949, Nov, 2010.

[124] L. Liu, D. Hu, and R. H. W. Lam, "Microfluidic Viscometer Using a Suspending Micromembrane for Measurement of Biosamples," *Micromachines (Basel),* vol. 11, no. 10, Oct 14, 2020.

[125] Y. Zhou, J. Chen, C. Liu, C. Liu, P. Lai, and L. Wang, "Single-shot linear dichroism optical-resolution photoacoustic microscopy," *Photoacoustics,* vol. 16, pp. 100148, Dec, 2019.

[126] X. Huang, W. Shang, H. Deng, Y. Zhou, F. Cao, C. Fang, P. Lai, and J. Tian, "Clothing spiny nanoprobes against the mononuclear phagocyte system clearance in vivo: Photoacoustic diagnosis and photothermal treatment of early stage liver cancer with erythrocyte membrane-camouflaged gold nanostars," *Applied Materials Today,* vol. 18, pp. 100484, 2020/03/01/, 2020.

[127] H. Li, F. Cao, and P. Lai, "Interferometry-free noncontact photoacoustic detection method based on speckle correlation change," *Optics letters,* vol. 44, no. 22, pp. 5481-5484, 2019.

[128] Z. Yu, H. Li, and P. Lai, "Wavefront shaping and its application to enhance photoacoustic imaging," *Applied Sciences,* vol. 7, no. 12, pp. 1320, 2017.

[129] Y. Wang, Y. Zhan, M. Tiao, and J. Xia, "Review of methods to improve the performance of linear array-based photoacoustic tomography," *Journal of Innovative Optical Health Sciences,* vol. 13, no. 02, 2019.

[130] J. Zhao, Q. Zhao, R. Lin, and J. Meng, "A microvascular image analysis method for optical-resolution photoacoustic microscopy," *Journal of Innovative Optical Health Sciences,* vol. 13, no. 04, pp. 2050019, 2020.

[131] C. G. Lou, and D. Xing, "Photoacoustic measurement of liquid viscosity," *Applied Physics Letters,* vol. 96, no. 21, May 24, 2010.

[132] Y. Zhao, S. Z. Yang, Y. T. Wang, Z. Yuan, J. L. Qu, and L. W. Liu, "In vivo blood viscosity characterization based on frequency-resolved photoacoustic measurement," *Applied Physics Letters,* vol. 113, no. 14, Oct 1, 2018.

[133] Y. Zhou, S. Liang, M. Li, C. Liu, P. Lai, and L. Wang, "Optical-resolution photoacoustic microscopy with ultrafast dual-wavelength excitation," *J Biophotonics,* vol. 13, no. 6, pp. e201960229, Jun, 2020.

[134] J. Pfitzner, "Poiseuille and his law," vol. 31, no. 2, pp. 273–275, 1976.

[135] W. H. L. V Wang, "Biomedical Optics: Principles and Imaging," *Biomedical Optics*, N. J. W.-I. x. Hoboken, 362, ed., pp. 283-321, 2007.

[136] L. D. Wang, J. J. Yao, K. I. Maslov, W. X. Xing, and L. H. V. Wang, "Ultrasound-heated photoacoustic flowmetry," *Journal of Biomedical Optics,* vol. 18, no. 11, Nov, 2013.

[137] A. Sheinfeld, and A. Eyal, "Photoacoustic thermal diffusion flowmetry," *Biomedical Optics Express,* vol. 3, no. 4, pp. 800-813, Apr 1, 2012.

[138] W. Liu, B. X. Lan, L. Hu, R. M. Chen, Q. F. Zhou, and J. J. Yao, "Photoacoustic thermal flowmetry with a single light source," *Journal of Biomedical Optics,* vol. 22, no. 9, Sep, 2017.

[139] Z. P. Yu, H. H. Li, and P. X. Lai, "Wavefront Shaping and Its Application to Enhance Photoacoustic Imaging," *Applied Sciences-Basel,* vol. 7, no. 12, Dec, 2017.

[140] Y. Zhou, J. J. Yao, and L. H. V. Wang, "Optical clearing-aided photoacoustic microscopy with enhanced resolution and imaging depth," *Optics Letters,* vol. 38, no. 14, pp. 2592-2595, Jul 15, 2013.

[141] Z. Bozóki, A. Pogány, and G. Szabó, "Photoacoustic instruments for practical applications: present, potentials, and future challenges," *Applied Spectroscopy Reviews,* vol. 46, no. 1, pp. 1-37, 2011.

[142] Q. Fu, R. Zhu, J. Song, H. Yang, and X. Chen, "Photoacoustic imaging: contrast agents and their biomedical applications," *Advanced Materials,* vol. 31, no. 6, pp. 1805875, 2019.

[143] J. L. Su, B. Wang, K. E. Wilson, C. L. Bayer, Y.-S. Chen, S. Kim, K. A. Homan, and S. Y. Emelianov, "Advances in clinical and biomedical applications of photoacoustic imaging," *Expert opinion on medical diagnostics,* vol. 4, no. 6, pp. 497-510, 2010.

[144] Y. Zhu, G. Xu, J. Yuan, J. Jo, G. Gandikota, H. Demirci, T. Agano, N. Sato, Y. Shigeta, and X. Wang, "Light emitting diodes based photoacoustic imaging and potential clinical applications," *Scientific reports,* vol. 8, no. 1, pp. 1-12, 2018.

[145] S. Jeon, J. Kim, D. Lee, J. W. Baik, and C. Kim, "Review on practical photoacoustic microscopy," *Photoacoustics,* vol. 15, pp. 100141, 2019.

[146] W. Liu, and J. Yao, "Photoacoustic microscopy: principles and biomedical applications," *Biomedical engineering letters,* vol. 8, no. 2, pp. 203-213, 2018.

[147] J. Yao, and L. V. Wang, "Photoacoustic microscopy," *Laser & photonics reviews,* vol. 7, no. 5, pp. 758-778, 2013.

[148] M. Moothanchery, and M. Pramanik, "Performance characterization of a switchable acoustic resolution and optical resolution photoacoustic microscopy system," *Sensors,* vol. 17, no. 2, pp. 357, 2017.

[149] M. Moothanchery, A. Sharma, and M. Pramanik, "Switchable Acoustic and Optical Resolution Photoacoustic Microscopy for in vivo small-animal blood vasculature imaging," *Journal of visualized experiments: JoVE*, no. 124, 2017.

[150] L. V. Wang, and J. Yao, "A practical guide to photoacoustic tomography in the life sciences," *Nature methods,* vol. 13, no. 8, pp. 627, 2016.

[151] C. Dong, C. C. Loy, K. He, and X. Tang, "Image super-resolution using deep convolutional networks," *IEEE transactions on pattern analysis and machine intelligence,* vol. 38, no. 2, pp. 295-307, 2015.

[152]   C. Ledig, L. Theis, F. Huszár, J. Caballero, A. Cunningham, A. Acosta, A. Aitken, A. Tejani, J. Totz, and Z. Wang, "Photo-realistic single image super-resolution using a generative adversarial network." pp. 4681-4690.

[153]   X. Wang, K. Yu, S. Wu, J. Gu, Y. Liu, C. Dong, Y. Qiao, and C. Change Loy, "Esrgan: Enhanced super-resolution generative adversarial networks." pp. 0-0.

[154]   Y. Rivenson, Z. Göröcs, H. Günaydin, Y. Zhang, H. Wang, and A. Ozcan, "Deep learning microscopy," *Optica,* vol. 4, no. 11, pp. 1437-1443, 2017.

[155]   H. Wang, Y. Rivenson, Y. Jin, Z. Wei, R. Gao, H. Günaydın, L. A. Bentolila, C. Kural, and A. Ozcan, "Deep learning enables cross-modality super-resolution in fluorescence microscopy," *Nature methods,* vol. 16, no. 1, pp. 103-110, 2019.

[156]   T. J. Allen, O. Ogunlade, E. Zhang, and P. C. Beard, "Large area laser scanning optical resolution photoacoustic microscopy using a fibre optic sensor," *Biomedical Optics Express,* vol. 9, no. 2, pp. 650-660, Feb 1, 2018.

[157]   I. J. Goodfellow, J. Pouget-Abadie, M. Mirza, B. Xu, D. Warde-Farley, S. Ozair, A. Courville, and Y. Bengio, "Generative adversarial networks," *arXiv preprint arXiv:1406.2661*, 2014.

[158]   M. Mirza, and S. Osindero, "Conditional generative adversarial nets," *arXiv preprint arXiv:1411.1784*, 2014.

[159]   T. S. Ralston, D. L. Marks, F. Kamalabadi, and S. A. Boppart, "Deconvolution methods for mitigation of transverse blurring in optical coherence tomography," *Ieee Transactions on Image Processing,* vol. 14, no. 9, pp. 1254-1264, Sep, 2005.

[160]   R. C. Lee, H. Kang, C. L. Darling, and D. Fried, "Automated assessment of the remineralization of artificial enamel lesions with polarization-sensitive optical coherence tomography," *Biomedical optics express,* vol. 5, no. 9, pp. 2950-2962, 2014.

[161]   C. F. Gainer, U. Utzinger, and M. Romanowski, "Scanning two-photon microscopy with upconverting lanthanide nanoparticles via Richardson-Lucy deconvolution," *Journal of Biomedical Optics,* vol. 17, no. 7, Jul, 2012.

[162]   H. Zhang, and X. Lv, "Modified robust anisotropic diffusion denoising technique with regularized Richardson-Lucy deconvolution for two-photon microscopic images," *Optical Engineering,* vol. 47, no. 4, pp. 047004, 2008.

[163]   M. Laasmaa, M. Vendelin, and P. Peterson, "Application of regularized Richardson-Lucy algorithm for deconvolution of confocal microscopy images," *J Microsc,* vol. 243, no. 2, pp. 124-40, Aug, 2011.

[164] J. H. Chen, R. Q. Lin, H. N. Wang, J. Meng, H. R. Zheng, and L. Song, "Blind-deconvolution optical-resolution photoacoustic microscopy in vivo," *Optics Express,* vol. 21, no. 6, pp. 7316-7327, Mar 25, 2013.

[165] T. Jetzfellner, and V. Ntziachristos, "Performance of Blind Deconvolution in Optoacoustic Tomography," *Journal of Innovative Optical Health Sciences,* vol. 4, no. 4, pp. 385-393, Oct, 2011.

[166] Y. Wang, D. Xing, Y. G. Zeng, and Q. Chen, "Photoacoustic imaging with deconvolution algorithm," *Physics in Medicine and Biology,* vol. 49, no. 14, pp. 3117-3124, Jul 21, 2004.

[167] C. Zhang, C. H. Li, and L. H. V. Wang, "Fast and Robust Deconvolution-Based Image Reconstruction for Photoacoustic Tomography in Circular Geometry: Experimental Validation," *Ieee Photonics Journal,* vol. 2, no. 1, pp. 57-66, Feb, 2010.

[168] L. Lin, P. F. Zhang, S. Xu, J. H. Shi, L. Li, J. J. Yao, L. D. Wang, J. Zou, and L. H. V. Wang, "Handheld optical-resolution photoacoustic microscopy," *Journal of Biomedical Optics,* vol. 22, no. 4, Apr, 2017.

[169] H. Wang, X. Q. Yang, Y. Y. Liu, B. W. Jiang, and Q. M. Luo, "Reflection-mode optical-resolution photoacoustic microscopy based on a reflective objective," *Optics Express,* vol. 21, no. 20, pp. 24210-24218, Oct 7, 2013.

[170] J. B. Chen, Y. C. Zhang, X. Z. Li, J. Y. Zhu, D. F. Li, S. L. Li, C. S. Lee, and L. D. Wang, "Confocal visible/NIR photoacoustic microscopy of tumors with structural, functional, and nanoprobe contrasts," *Photonics Research,* vol. 8, no. 12, pp. 1875-1880, Dec 1, 2020.

[171] Y. Yuan, S. H. Yang, and D. Xing, "Optical-resolution photoacoustic microscopy based on two-dimensional scanning galvanometer," *Applied Physics Letters,* vol. 100, no. 2, Jan 9, 2012.

[172] J. Yao, C.-H. Huang, K. I. Maslov, L. Wang, L. Gao, J. Zou, and L. V. Wang, "Water-Immersible MEMS Scanning Mirror Enhanced Optical-Resolution Photoacoustic Microscopy," *OSA Technical Digest.* p. BSu3A.54.

[173] B. Lan, W. Liu, and J. Yao, "High-speed Wide-field Photoacoustic Microscopy," *OSA Technical Digest.* p. JTu3A.68.

[174] J. H. Park, Z. P. Yu, K. Lee, P. X. Lai, and Y. Park, "Perspective: Wavefront shaping techniques for controlling multiple light scattering in biological tissues: Toward in vivo applications," *Apl Photonics,* vol. 3, no. 10, Oct, 2018.